UNIVERSIDAD Ð LA LAGUNA
Departamento de Astrofísica

Morphology and metallicities of OTELO galaxies.

Jakub Nadolny

Memoria presentada para optar al grado de
Doctor en Ciencias Físicas.

Directores:
Dr. Jordi Cepa
Dr. Ángel Bongiovanni
Dr. Miguel Cerviño

INSTITUTO Ð ASTROFISICA Ð CANARIAS
Enero de 2021

Examination date: 2021
Thesis supervisors: Dr. Jordi Cepa, Dr. Ángel Bongiovanni, and Dr. Miguel Cerviño

Some of the material included in this document has been already published in *Astronomy & Astrophysics*.

Dla rodziców.

Resumen

En esta tesis exploramos el cartografiado OTELO (OSIRIS Tunable Filter Emission Line Object). Gracias al uso de los filtros sintonizables de instrumento OSIRIS de Gran Telescopio Canarias, OTELO recupera objetos con líneas de emisión hasta flujos muy débiles. El método de tomografía permite construir espectros de baja resolución ($R \sim 700$) para todos los objetos detectados. El flujo de linea límite estimado es de $4.6 \times 10^{-19}\,\mathrm{erg\,s^{-1}\,cm^{-2}}$, haciendo del cartografiado OTELO el más profundo en flujo de línea disponible hasta la fecha.

En particular, en este trabajo presentamos un catalogo morfológico de los objetos de OTELO detectados en las imágenes de alta resolución del instrumento ACS del *Hubble Space Telescope*. Para ello, hemos usado un mt́odo paramétrico que ajusta un modelo 2D informado por el perfil de Sérsic, incluido en la versión multi-onda de la aplicación `GALFIT`. Este programa ajusta instantáneamente el perfil seleccionado a los objetos seleccionados en las bandas fotométricas disponibles mediante el uso de funciones polinomiales de Chebyshev. Comparando con la versión estándar de `GALFIT`, mostramos que los resultados de la versión multi-onda del mismo programa proporciona resultados más robustos, en particular en el regimen de baja señal a ruido. Addicionalmente, los resultados de la inspeción visual de los objetos seleccionados (hasta magnitud $I = 24.5$) son consistentes con los parámetros estimados mediante `GALFIT`. Usando los mismos parámetros probamos varios métodos de segregación de galaxias tempranas y tardías; también investigamos la relación entre la masa estelar y el tamaño para ambos tipos de objetos. Además de lo anterior, confirmamos la evolución de la mediana de la masa estelar hasta $z = 2$.

Usando el catálogo morfológico descrito, seleccionamos una muestra de las galaxias tempranas en emisión (ET-ELG). La naturaleza y el origen de las líneas de emisión en estos objetos están siendo investigadas aún. Usando una muestra de 14 objetos de ET-ELG a un dezplazamiento al rojo , comparamos la densidad de estos objetos con una muestra local análoga extraída del cartografiado SDSS. Encontramos que OTELO detecta una densidad considerablemente

mayor de ET-ELG que en la muestra a bajo desplazamiento al rojo del SDSS. Estos resultados se mantienen, aún teniendo en cuenta la varianza cósmica – la fuente de incertidumbre más importante para un cartografiado con una cobertura angular discreta ($\sim$56 arcmin^2) como OTELO.

Por último, investigamos la relación entre la masa estelar y la metalicidad de una muestra de objetos con emisión en Hα a $z \sim 0.4$. En particular, y aprovechando la capacidad de OTELO de detectar objetos con flujo límite muy bajo, estudiamos una muestra de emisores de línea con muy baja masa ($\sim 10^7\, M_\odot$). La gran mayoría de estos objetos están clasificados morfológicamente como galaxias de disco, con un índice de Sérsic bajo, lo esperado para las galaxias con formación estelar activa. No hemos encontrado evidencia alguna de evolución de la relación masa-metalicidad desde $z = 0.4$.

Abstract

In this thesis we explore the OTELO (OSIRIS Tunable Filter Emission Line Object) survey. OTELO is a very deep, pencil beam survey for the search of emission line sources by means of the tunable filters of the OSIRIS instrument, installed at the Gran Telescopio Canarias. A tomography scan method results in 2D, low-resolution pseudo-spectra for all the sources in the observed field. The reached line flux of 4.6×10^{-19} erg s^{-1} cm^{-2} makes it the deepest survey in terms of the line flux.

In particular, we present the morphological catalogue of the OTELO sources detected in high-resolution images from the ACS instrument of the *Hubble Space Telescope*. We have employed a parametric method to fit 2D model composed of single-Sérsic profile using a multi-wavelength version of `GALFIT` software. This software fits simultaneously selected model to all given images using Chebyshev polynomial functions. We show that this multi-wavelength method provides better results in the low signal-to-noise, recovering a substantial fraction of sources in this regime, as compared to a standard version of the same software. We also provide a preliminary visual morphology of the selected sample (up to magnitude I=24.5 mag). The results of this analysis are consistent with the obtained from the parametric method. We have tested various methods for separation of early-type galaxies from late-type galaxies, as well as the mass-size relation. We also found a median stellar mass evolution up to $z = 2$ finding good agreement with previous works.

From the morphological catalogue we selected a population of early-type emission line galaxies (ET-ELG). Even if under investigation for many decades, there is lack of the clear consensus on the nature and origin of the emission lines found in the ET-ELG. We study a sample of 14 such objects at intermediate redshift. Due to the limited spectral information available, we compared the number densities of our sample with a carefully selected sample of local counterparts from SDSS. We found that OTELO detects a considerably higher ET-ELG density than it would be expected from the local SDSS sample. This

result holds even considering a cosmic variance – the most important source of uncertainties for a pencil beam survey ($\sim$56 arcmin^2) as OTELO.

Finally, we studied a stellar-mass–metallicity relation (MZR) of selected Hα emission line sources at $z \sim 0.4$. Particularly, and taking advantage of the depth reached by the OTELO survey, we focus on the very low-mass end of this relation, with the low-mass limit ($\sim 10^7\, M_\odot$). Most of the galaxies in the Hα sample are morphologically classified as disk-like sources with low Sérsic index, as expected for the star-forming galaxies. We have found no evidence for the evolution of the MZR since $z = 0.4$.

Agradecimientos

Laura. Gracias por todo. Gracias por tu paciencia, compasion, amor, apoyo. Gracias por tus consejos, gracias por escucharme. El doctorado de astrofísica fue una excusa para quedarme por aquí y poder emepzar una escuela de la vida contigo. Mar gracias por tus abrazos, tu sonrisa, y las ganas de aprender que tienes! Manuel, aunque todavía estás en la barrigita, te quiero mucho y ya tengo ganas de verte!

En segundo lugar quiero agradecer a Jordi, el director de la tesis. Gracias por guiarme a lo largo de este tiempo con tus comentarios, dejandome espacio para aprender de las pruebas y ensayos, pero siempre vigilando para cumplir los objetivos. Ángel, Miguel gracias por co-dirigirme en este trabajo. Ángel, gracias por tu tiempo, por las infinitas coversaciones (muchas veces en las horas nocturas, cuando el IAC estaba ya vacio) y todo el apoyo. Las charlas sobre masa madre, himalaismo, fotografia, y muchos más temas han sido estimulantes. Gracias por el apoyo en los momentos de "baja temporada". Miguel, gracias por estar siempre listo para ayudar. Por tu franqueza, la actitud positiva, y la rapidez de actuar. Quiero agradecer también a Maritza por acogernos en Copenhague. Fue un tiempo estimulante, y con resultados importantes para esta tesis.

Quiero agradecer también a todos los *Otelianos et al.*, ya que todos tienen una parte, mas o menos grande, en este trabajo. Las reuniones semanales fueron muy estimulantes. Pero no quiero agradecerles solo el lado cientifico, pero también el ambiente de amistad y apoyo de todos ustedes. Gracias por los "viernes a medio día", y todas las salidas nocturnas a buscar algún que otro Bacalao.

Rodzice! Dziękuję za wasze wsparcie, na odległość, ale jednak wielkie wsparcie! Dziękuję wam za wiarę we mnie. Dziękuję za wasze kochające serca! Ewa, Lusia. Dzięki za to, że jesteście zawsze gotowe na wysłuchanie problemów i za wasze wsparcie w trudnych momentach. Dzięki za wasz bliskość nawet na

odległość. Filip, bracie. Dzięki za inspirację do robienia trudnych rzeczy, które na początku mogą wydawać się niewykonalne.

Astroteam: Camilo y Salvo! Gracias chcios por estos años. Salvo gracias por acompañarme desde primer día en la Universidad, literalmente. Camilo, gracias por todos los entrenamientos y tu positividad! Tener amigos así es una ganancia sin comparación.

Finally, I want to give thanks to my personal saviour Jesus Christ, the cause of everything.

∼K.

Acknowledgments

This work was supported by the project Evolution of Galaxies, of reference AYA2014-58861-C3-1-P and AYA2017-88007-C3-1-P, within the "Programa estatal de fomento de la investigación científica y técnica de excelencia del Plan Estatal de Investigación Científica y Técnica y de Innovación (2013-2016)" of the "Agencia Estatal de Investigación del Ministerio de Ciencia, Innovación y Universidades", and co-financed by the FEDER "Fondo Europeo de Desarrollo Regional". Based on observations made with the Gran Telescopio Canarias (GTC), installed in the Spanish Observatorio del Roque de los Muchachos of the Instituto de Astrofísica de Canarias, on the island of La Palma. This work made use of the IAC Supercomputing facility HTCondor (`http://research.cs.wisc.edu/htcondor/`). This work made use of the Wright (2006) cosmological calculator. Based on observations obtained with MegaPrime/MegaCam, a joint project of CFHT and CEA/IRFU, at the Canada-France-Hawaii Telescope (CFHT) which is operated by the National Research Council (NRC) of Canada, the Institut National des Science de l'Univers of the Centre National de la Recherche Scientifique (CNRS) of France, and the University of Hawaii. This work is based in part on data products produced at Terapix available at the Canadian Astronomy Data Centre as part of the Canada-France-Hawaii Telescope Legacy Survey, a collaborative project of NRC and CNRS. This research uses data from the VIMOS VLT Deep Survey, obtained from the VVDS database operated by Cesam, Laboratoire d'Astrophysique de Marseille, France. IRAF is distributed by the National Optical Astronomy Observatories, which is operated by the Association of Universities for Research in Astronomy, Inc. (AURA) under cooperative agreement with the National Science Foundation (Tody 1993).

Contents

List of Figures

List of Tables

1

Introduction

1.1 Extragalactic surveys

Sky surveys play a fundamental role in the study of the phenomena found in the near and far Universe. Generally speaking, sky surveys collect a number of parameters of different types of objects. Historically, these collections of data can be traced back to the time when the eye and a piece of paper were the detector and a hard-disk. As a first systematic sky survey of extended sources one can consider the work of Charles Messier in the middle of 18^{th} century, containing a total of about one hundred entries. Messier's work was followed by that of Herschel (1864) and his family in the late 19^{th} century. Herschel's catalogue with several thousands objects was a precursor of the still-used New General Catalogue (NGC) compiled by Dreyer (1888). The size of the catalogues increased with time, mostly because of advances in the available technology.

The invention of the photographic plate was a first milestone in the endeavor to survey the sky at the end of 19^{th} century. Photographic plates helped to cover larger sky areas thus increasing the number of catalogued sources. For example, a collection of more than 220 000 stars was catalogued in the *Henry Draper Catalogue*, compiled by Edward C. Pickering, Annie J. Cannon, and collaborators in the 20s of the last century. Photographic plates were also the tool for one of the most important works (in my opinion) in astronomy of all time. This was the basis of the work developed by Hubble (1926), where observations of $\sim$400 extra-galactic nebulæ were systematically carried out at the Mount Wilson Observatory. Careful examination of the photographic plates resulted in the still widely used galaxy classification scheme, the so-called Hubble's tun-

ing fork, along with the first insights on the expansion of the Universe. The *Harvard Plate Collection* from Harvard College Observatory, with more than 500 000 images taken between 1882 and 1992 is another good example of a survey based on photographic plates. Currently further efforts are being made to scan a majority of these photographic glass negatives by the *Digital Access to a Sky Century at Harvard* (DASCH) project[1] to produce enhanced photometric catalogues.

A *Palomar Observatory Sky Survey I* (POSS-I) was also based on photographic plates. It was conducted in the 50s using a wide-field Schmidt telescope at Mount Palomar. A total of 936 plates covering two thirds of the sky visible from this site were observed. POSS-II followed four decades later. A visual inspection of these plates led to several catalogues of sources with different properties. For example the *Morphological Catalog of Galaxies* with about 30 000 galaxies (Vorontsov-Velyaminov & Krasnogorskaya 1974); the *Uppsala General Catalogue* with more than 10 000 galaxies with apparent diameter > 1 arcmin (Nilson 1973); and the catalogue with about 3 000 rich galaxy clusters compiled by Abell (1958), to name only a few.

In parallel, during the mid-20 century, observations of the sky in different spectral regimes emerged. These span from γ-ray and X-ray, through infrared (IR), to radio frequencies. In particular, as early as the beginning of the 30s, radio astronomy, with pioneering work by Karl Jansky and Grote Reber, resulted in the discovery of the radio emission from the Milky Way. Soon after, the development of radio interferometry led to the first catalogues with discrete radio sources. Emblematic examples are the Third Cambridge (3C) and the Fourth Cambridge (4C) catalogues. Thanks to these catalogues the first quasi-stellar object (QSO; 3C 273) was discovered. Furthermore, the Space Race during the Cold War opened possibilities to observe the Universe in the UV spectral range ($\lambda < 320$ Å) not available from ground-based facilities. Since the early 60s space telescopes are orbiting the Earth providing excellent data in high-energy spectral regime in particular, otherwise blocked by the Earth's atmosphere.

Another milestone was invention of the charge-coupled device (CCD). Even if first CCD's were manufactured in the late 60's, only few decades ago the sensitivity and resolution made them a real "game-changer" in the astronomical observations. This development coincided with the increase in computational power which is essential to process all the data gathered. A great example of the all-sky *optical* survey is the Sloan Digital Sky Survey (SDSS, York et al. 2000). With its 16$^{\text{th}}$ data release (DR16, Ahumada et al. 2020), and after about 20 years of operation, it contains data for several million unique objects, including

[1] `https://platestacks.cfa.harvard.edu/dasch-project`

spectroscopic data for more than two million sources. The statistical power of SDSS led to the discovery of many new phenomena, types of sources, or relations between the parameters of statistically significant populations of sources. While SDSS is the optical survey, *The Two Micron All Sky Survey* (2MASS, Skrutskie et al. 2006) was designed to survey the near-infrared (NIR) sky. A catalogue with almost two million extended NIR sources, covering virtually the entire night sky, is now available. The synergy of surveys at different spectral ranges provides a multi-wavelength view on the multiple types of sources with a variety of different phenomena.

The above brief introduction shows that there are multiple types of surveys. The all-sky surveys cover large areas of the sky in a particular spectral range (like SDSS or 2MASS). There are also surveys which are focused on observing a limited patch of the sky in order to detect fainter sources. A good example is *Hubble Ultra Deep Field* (Beckwith et al. 2006) exposing a field of 11 arcmin^2 for about a million seconds, reaching a limiting magnitude of 29 (AB). On the other hand, we can supplement photometric data from spectroscopic surveys. In these surveys, pre-selection of the targets is a common practice since the spectroscopic observations are time-consuming. An close example of these could be Lockman-SpReSO survey (González-Otero et al. 2020), which aims to observe the optical counterparts of selected far-IR (FIR) galaxies. There are also spectroscopic surveys with virtually no target pre-selection biases, apart from the magnitude cut, in order to reach a desirable signal-to-noise (S/N) ratio. This methodology was applied in the VIMOS VLT deep survey (VVDS, Le Fèvre et al. 2005) or in the SDSS spectroscopic sample.

A natural consequence of all the data gathered in this great variety of surveys is a creation of catalogues where a range of particular parameters are recompiled, for example, photometric data, emission line fluxes, redshifts, or morphological parameters. A good example of such a catalogue is the *Galaxy Zoo* project (Lintott et al. 2008), where an enormous effort has been made to provide visual morphological classification for a large collection of galaxies observed in the framework of SDSS. This particular project involved a general public in the classification process. More than 4×10^7 classifications has been made by about 10^5 participants. This kind of projects have its own advantages and disadvantages, but the scope of this thesis is beyond to provide a discussion on this type of projects.

Yet another type of surveys is devoted to the search for emission line systems (ELS). These objects are particularly important, not only for this thesis. Emission-line analysis opens the door to the intimacy of the observed source, through which we can significantly study their physical conditions (see next Section). These surveys can use different observing strategies to detect such

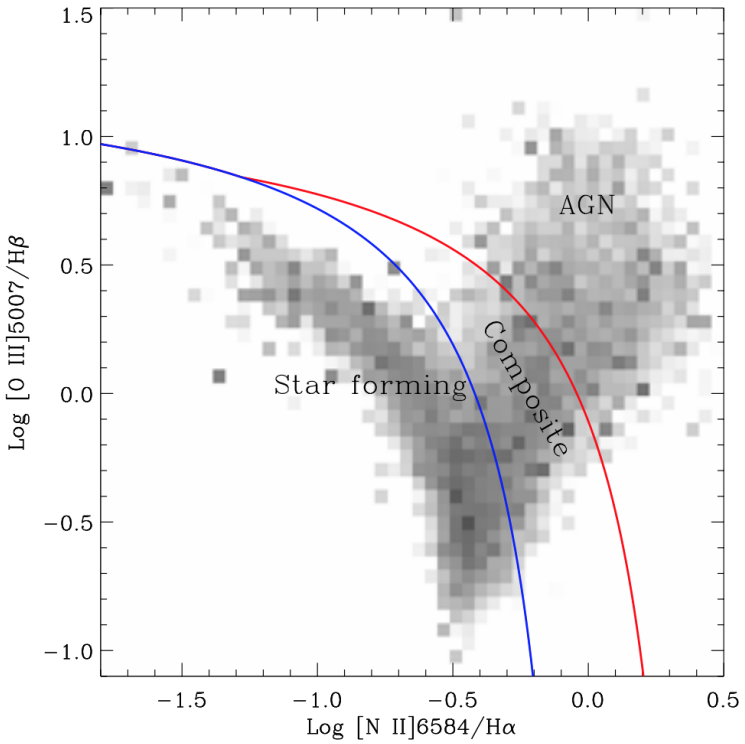

Figure 1.1. BPT diagnostic diagram. Figure taken from Brinchmann et al. (2004) with $\sim$ 150 000 SDSS galaxies.

emission lines from the sources. Examples of these are the blind slit-less spectroscopic or narrow-band surveys, to name just a couple. More details on this type of surveys are given in Section 1.3.

1.2 Emission line Universe

Emission lines are of great importance for study of the Universe because of their ubiquitous presence in almost all observed sources including the Sun, other Galactic stars, planetary nebulæ, star-forming galaxies (SFG), AGN/QSO, and even the Earth's atmosphere. Furthermore, emission lines are detected along the whole spectrum from X-ray to radio domain. Detailed analysis of emission lines provide an efficient way to study chemical abundances, the star-formation rate (SFR) and its history (SFH), kinematics, and other physical conditions of emitting source, as well as to determine its redshift z.

Selected ratios of emission lines are used as a diagnostic methods to distin-

guish between various types of host galaxies. One of the most commonly used diagnostic diagram is a BPT diagram (Baldwin et al. 1981), named after proponents of the method. In the BPT diagram one can segregate the SFG, composite and narrow-line AGN hosts. In Figure 1.1 we show an example from Brinchmann et al. (2004), where a total of about 150 000 galaxies from SDSS is included. This is a textbook example of the statistical power of large galaxy surveys and the emission line analysis. In this particular diagram, authors have used the line ratio of [O III]5007/Hβ vs. [N II]6584/Hα. Veilleux & Osterbrock (1987) further proposed two different ratios of [S II]6725/Hα and [O II]6300/Hα, to be used with [O III]5007/Hβ. As noted by Stasińska et al. (2006), the [N II]6584/Hα ratio (so-called N2 index) can be used alone as a proxy for the SFG and AGN separation. Since [O III]5007 and Hβ lines are not used in this method, it can be applied to larger samples.

Emission lines can also be used to estimate relative chemical content, also called metallicity of the object. As proposed by Alloin et al. (1979), semi-empirical relations between the emission-line intensities are adequate to estimate the metallicities of SFG's. For instance, the [N II]6584/Hα ratio (N2 index), or $\log\{([\text{O III}]5007/\text{H}\beta)/([\text{N II}]6584/\text{H}\alpha)\}$ (O3N2 index) can be also used as a metallicity estimation as showed by Pettini & Pagel (2004). With its own limitations, these however are widely used because of the relatively easy detection of the emission lines employed.

Furthermore, several emission lines can be used to estimate the SFR. While the line luminosity provides insights about recent star-formation episodes, the equivalent width can be used to estimate the ratio of the present to past SFR. To this purpose one can use Hα or Lyα emission, both pursue directly the UV emission of young OB starts (although an AGN can also contribute to these lines). Another SFR tracers are [O II]λ3727 or [O III]λ5007, however with more complex dependency on the interstellar medium (ISM), dust extinction, and metallicity. In the case of the latter emission line, it have to be used with caution, because of its further non negligible dependence on the mass of the ionizing star cluster (Villaverde et al. 2010). NIR emission lines, like hydrogen Paschen α, can also be used to estimate SFR, however, due to the current instrumentation it can be observed only in the low-redshift regime. In the near future the *James Webb Space Telescope* will cover this spectral range enabling the use of these lines for galaxies observed when the Universe was younger. Despite the X-ray, and radio emission lines were also used to trace the SFR, we will not discuss these methods here. For more details on this issues see Cepa (2008) and reference therein.

1.3 Searching for the emission lines

Because of the wealth of information hidden behind the emission lines, there are dedicated surveys to search for the ELS. Four main types can be highlighted: slitless spectroscopy, mid-band imaging using colour excess, mid/narrow-band slicing, Fabry-Pérot interferometers, and its particular type, the tunable filter (TF) imaging.

First type of surveys are the blind, slitless spectroscopic surveys. Good examples of these are UCM (Gallego et al. 1993), KISS (Wegner et al. 2003), CUYS (Bongiovanni et al. 2005), or PEARS (Straughn et al. 2009). These surbeys, however, have limited capacity in crowded fields where spectra of individual galaxies overlap. The multi-object spectroscopy (MOS) approach, or the use of integral-field units (IFU) can help to overcome the issue of crowded fields, but with the expense of the completeness of target selection (e.g., SDSS; GAMA Driver et al. 2011; DEEP2 Newman et al. 2013).

Another type of surveys dedicated to ELS search are the medium- and narrow-band surveys. Among these we can also point to fundamental differences in the design of the particular surveys. On one hand, we have surveys which uses several medium-bands (width of about hundred of Å), allocated in different, non-overlapping spectral windows. These surveys additionally uses broad-bands images as well. The presence of emission line is detected by the colour excess in colour diagrams built by using using the wide- and narrow-band photometry. These surveys however, are limited in spectral resolution and can provide very little information about emission line. The advantage is that these surveys cover relatively large areas of the sky. Examples of these are SDF (Kashikawa et al. 2004), SDXS (Ouchi et al. 2010), or HSC-SSP (Hayashi et al. 2018). On the other hand, we have surveys which make use of sequence of medium-band filters with overlapping spectral frequencies. The number of filters and their widths define the spectral resolution and the redshift range of detected emission lines. ALHAMBRA (Moles et al. 2008), SHARDS (Pérez-González et al. 2013) or J-PAS (Benítez et al. 2014) are representative examples of this type of surveys.

The last type of surveys focused on the ELS makes use of the tunable filters (TF). The narrow spectral range of each filter tuning (a few tens of Å), combined with a sequence of spectral (or tomography) scans, allows to obtain low-resolution spectra for the search of emission lines with EW limits lower than the obtained from classic narrow-band surveys. In order to complete such survey it is necessary to observe the same area of the sky multiple times. Hence, most of the surveys designed in this way are limited in the covered area. However, an additional advantage is the reached depth in the limiting emission line flux en-

abling detection of very faint (or low-mass) sources, including sources with not detected continuum. The TTF (Jones & Bland-Hawthorn 2001), CADIS (Hippelein et al. 2003), and OTELO (Bongiovanni et al. 2019) are good examples of such surveys.

1.4 The OTELO survey

The OTELO (OSIRIS Tunable Filter Emission Line Object) survey is a very deep, blind spectroscopic survey. It is based on the red tunable filter (RTF) images obtained through the OSIRIS (Cepa et al. 2003) instrument at Gran Telescopio Canarias (GTC). A total of 108 dark hours (PI: Jordi Cepa) were devoted to obtain 36 RTF tomography scans of the selected Extended Groth Strip region, covering $\sim$ 56 sq-arcmin. The RTF spectral energy distribution (SED) allowed to build intermediate resolution ($\sim$ 700) pseudo-spectra (PS; more details are given in Sec. 2.1.2). The limiting line flux of 4.6×10^{-19}erg s^{-1}cm^{-2} and an equivalent width of $EW \approx 6$ Å (Bongiovanni et al. 2020) makes OTELO the deepest survey to date in terms of the emission line flux. Because the selected spectral window of the RTF scans between 9070 Å and 9280 Å, OTELO survey probes different cosmic volumes depending on the emission line detected in the PS. The co-addition of reduced and aligned RTF scans provide a detection image OTELO$_{deep}$ from which a total of 11 273 raw detections were extracted (see Bongiovanni et al. 2019)

The OTELO survey enables the study of variety of astrophysical objects and its properties up to redshift $z \sim 6.55$. Among the principal scientific goals of the OTELO survey we can (i) study AGN/QSO populations and star-forming galaxies (SFG), (ii) determining star-formation rate (SFR) of the low-mass end of SFG at different redshifts, and (iii) sampling of the faint-end of the luminosity function (in Hα, [O III], or other detected emission line). Some of these were already explored (Ramón-Pérez et al. 2019; Ramón-Pérez et al. 2018; Bongiovanni et al. 2020; Nadolny et al. 2020; de Diego et al. 2020, Hα luminosity function; Hα AGN population; study of the [O III] ELS; Hα SFG; morphology classification with machine learning techniques, respectively) or are in preparation (study of compact galaxies; Hβ, [O II] ELS including luminosity functions; redshift estimation with machine learning).

In summary, OTELO survey is designed to explore the emission line Universe using PS, which enable the detection of ELS down to the low-mass regime ($\log M_*/M_\odot > 6$).

For more details on the OTELO's data-products see Chapter 2.

1.5 Aims of this thesis

Various aspects of the OTELO survey are explored in this work. In the following lines I give a brief insights about the aims of this thesis.

The main goal of this thesis is to provide a morphological catalogue with basic parameters derived from the high-resolution *HST*-ACS images available in the OTELO field. Using estimated parameters, we study the stellar-mass–size relation (MSR) of galaxies up to $z = 2$, and down to stellar-masses of $\log M_*/M_\odot \sim 8$, which is $\sim$1 dex. lower than the lower mass limit established in previous studies at the same redshift range (van der Wel et al. 2014; Mowla et al. 2019). In particular, we present insights on the median size evolution r_e–z for LT and ET galaxies at a fixed stellar-mass found in the OTELO field. This study is based on the accepted article Nadolny et al. (2021, A&A accepted). Since galaxy morphology is related to other galaxy properties, this information is crucial for this thesis, as well as for the exploitation of the OTELO survey scientific goals. Among these we can highlight the following: a census of ET galaxies with emission lines, a comprehensive study of the properties of compact galaxies, a comparison of extragalactic sources with and without detection of emission lines. Furthermore, the morphological catalogue presented here was already successfully used in published work (de Diego et al. 2020) on the machine learning techniques to separate ET from LT galaxies.

The second aim of this thesis is the study of count numbers of a population of early-type emission line galaxies (ET-ELG) at several cosmic volumes. Their morphological parameters are obtained from the morphological catalogue and template fitting of SEDs, while their emission is revealed in the OTELO's RTF pseudo-spectra. We compare our results with carefully selected local ET-ELG counterparts from SDSS.

The last part of this work is devoted to the Hα ELS. These objects are found in the first cosmic volume explored by the OTELO survey. In particular, we focus on the stellar-mass–metallicity relation (MZR) of the low-mass end of the SFG. Using OTELO's pseudo-spectra, fluxes of the [N II] and Hα emission lines are used to select SFG and to derive metallicities. These results has been presented in Nadolny et al. (2020).

The thesis is organized as follows. In Chapter 2 we describe the OTELO data-products, with details on the survey's observational design. In the same Chapter, we define complementary data used (i.e., broad-band images used to derive morphology, or other catalogues used to compare our findings). Chapter 3 outlines the methods used along the thesis, explaining software and setup parameters, as well as the method to obtain stellar-masses or emission line parameters. In Chapters 4 we study the morphology classification including

MSR and evolution of median size relation for ET and LT galaxies up to $z = 2$; in Chapter 5 we study the number density of ET-ELG galaxies; in Chapter 6 we present results on the mass-metallicity relation of the Hα sample, respectively. Finally, in Chapter 7 we present the conclusions of this thesis.

2

Data

In this Chapter we describe the data used along this thesis. Firstly, we provide a brief introduction to tunable filters and a particular case of the OTELO tunable filter observations, following with the OTELO catalogue assembly. Even though in this thesis we use already constructed OTELO catalogue, some technical background is essential for better understanding of the OTELO data products. We further describe the data from external surveys which were used to provide morphological classification, and to build samples with which we could compare our results.

2.1 OTELO catalogue

The OTELO survey takes advantage of the red tunable filter (RTF) of the OSIRIS instrument installed at GTC. A brief description of the basic concepts of tunable filters, the OTELO's observation strategy, and data-products (including pseudo-spectra, OTELO_{deep} and multi-wavelength catalogue) is given in what follows.

2.1.1 Tunable filter

The origin of tunable filter (TF) goes back to the end of 19^{th} century when Alfred Pérot and Charles Fabry have came up with a novel method of the use of interferometry (Pérot & Fabry 1899; Fabry & Pérot 1901). These so called Fabry-Pérot interferometers (FP) were used since then to study many

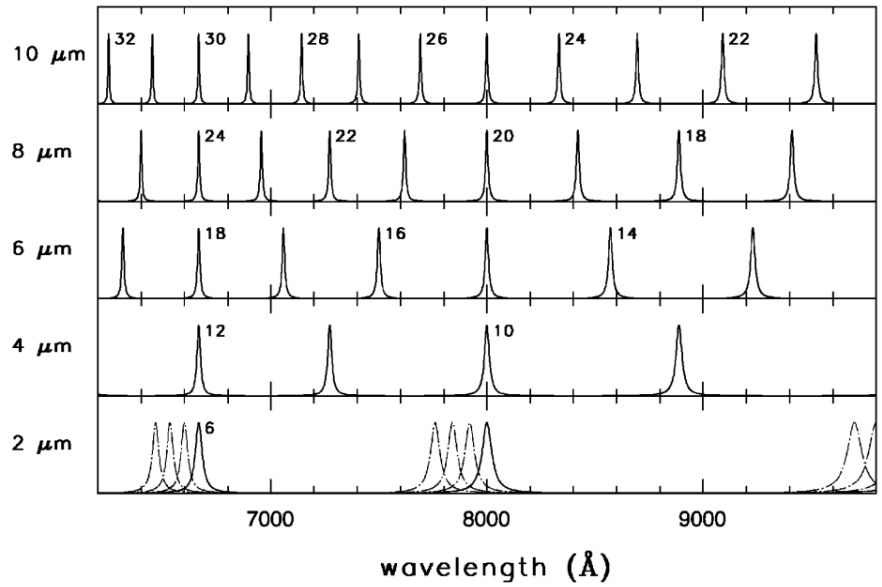

Figure 2.1. Transmission profile of TF as a function of wavelength for a given spacing (2, 4, 6, 8 and 10 μm) between parallel plates. Dot-dashed lines in the bottom panel represents the change of the spacing between plates for 1.98, 1.96 and 1.94 μm. Figure taken from Jones et al. (2001).

phenomena found in astrophysical objects via emission lines properties.

The FP interferometer is based on two parallel, highly reflective plates. These plates, or coatings, are separated by a small distance. Light entering the interferometer experience multiple reflections between the coatings resulting in destructive and constructive interferences. If both plates have a reflection coefficient R, then a transmission function is defined as

$$\frac{I_{transmitted}}{I_{incident}} = \left(\frac{T}{1-R}\right)^2 \left[1 + \frac{4R}{(1-R)^2}\sin^2\left(\frac{2\pi\mu d\cos\theta}{\lambda}\right)\right]^{-1}, \qquad (2.1)$$

where T is the transmission coefficient of each plate, R is the reflection coefficient, d is the plate separation, μ is the refractive index of the medium in the cavity (usually air, $\mu = 1$), and θ is the angle of incident light.

The transmission spectrum shows a series of the peaks of large transmission at specific orders of interference m given by

$$m\lambda = 2\mu d\cos\theta. \qquad (2.2)$$

The spacing of the parallel plates defines the resolution of the observed spectra (i.e., the larger the spacing, the higher resolution) and the resonance

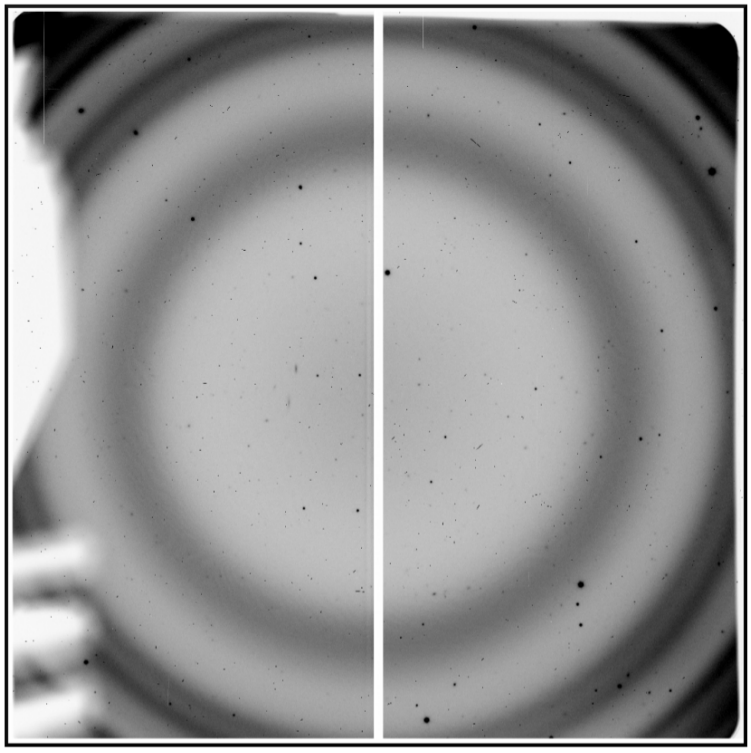

Figure 2.2. OTELO's raw red tunable image (inverted colours). The wavelength dependence of the distance from the optical center can be appreciated from the imprint of airglow emission.

wavelength. Furthermore, the angle of incidence of the entering light affects the position of the interference peaks. In Figure 2.1 we show the transmission spectrum of TF as a function of wavelength and for different spacing values (Figure form Jones et al. 2001).

The TF is a particular type of FP with much smaller gap between the parallel plates what makes it a low-resolution FP interferometer. The transmission (Airy) profile can be approximately expressed as a function of the central wavelength of the given peak, and the full width at half maximum (FWHM) of the profile. Thus, the TF enable consecutive narrow-band imaging at selected wavelength and bandwidth, which can be translated to the so-called tomography scans. In order to avoid unwanted input of different interference peaks (or orders of interference m) into scientific image, it is obligatory to use a order-sorter (OS) filter. The OS filter allows to select a single peak within a free spectral range previously defined.

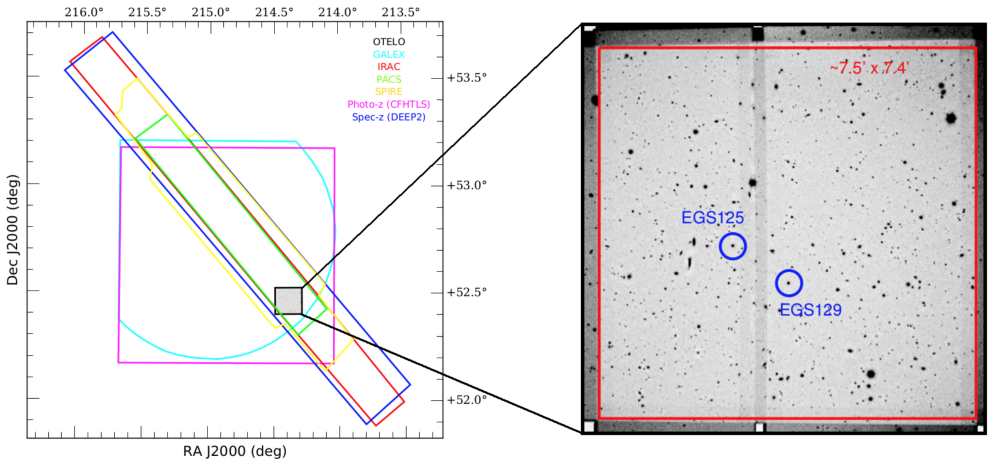

Figure 2.3. Spatial distribution of the multi-wavelength data used in the OTELO catalogue (*left panel*). On the *right panel* the OTELO's field is expanded. Red polygon represents the OTELO survey area, while blue circles indicates position of two flux calibration stars. Figure taken from Bongiovanni et al. (2019).

Characteristics of the OSIRIS's tunable filters

The OSIRIS (Optical System for Imaging and low Resolution Integrated Spectroscopy) instrument installed at GTC can be used in image and spectroscopy (long-slit or multi-object) modes. For imaging mode, apart form the standard, broad-band filters, OSIRIS is equipped with two different tunable filters. One operates in the blue spectral range (between 4500 and 6170 Å), while the second one in the red part of the electromagnetic spectrum (between 6510 and 9345 Å). Three piezoelectric devices control with a high precision the spacing and parallelism of the two plates that constitute the TFs. Thus, the synergy of the big collecting area of the GTC (with a primary mirror of 10.4 m in diameter), the relatively big field-of-view (FoV) of OSIRIS ($\sim$7.8 $\times$ 7.8 arcmin square), and the availability of the TFs makes it a unique tool for search of the faint emission line galaxies.

Various characteristics of the TF images from OSIRIS are described shortly in what follows. Resulting effective wavelength of the image depend on the TF setup (central wavelength and FWHM of the filter) as well as on the angle of incidence of the light. Thus, for different angles of incidence we obtain slightly different observed wavelength. For a tuned wavelength, the central part of the field is nearly monochromatic (Jacquinot spot). Rigorously, the effective observed wavelength changes from longer to shorter with the distance from the optical center. The resulting image contains monochromatic rings as can be

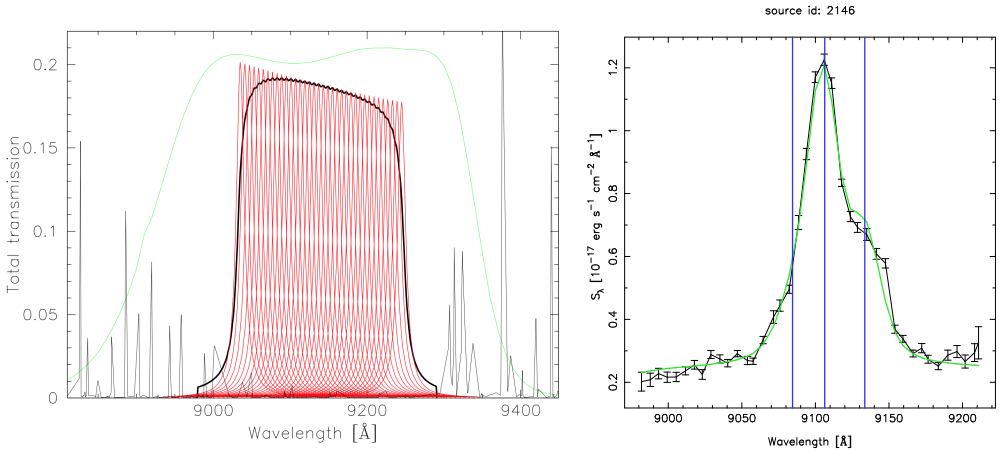

Figure 2.4. *Left panel:* Transmission of the 36 RTF used in the OTELO survey (red), together with resulting OTELO-custom filter (thick line in black). The order-sorter filter is showed as thin line in green. Black thin lines shows the sky emission lines. Figure taken Bongiovanni et al. (2019). *Right panel:* an example of PS of the Hα + [N II] emitter `id:2146` at $z\sim0.4$. Vertical blue lines represent the centers of the emission lines obtained after the inverse deconvolution of the PS, and the green curve shows the best convolved model. Figure taken from Nadolny et al. (2020).

appreciated in Figure 2.2. In the case of the RTF of OSIRIS, the observed empirical dependency of wavelength on the distance from the optical center is given by (González et al. 2014)

$$\lambda = \lambda_0 - 5.04r^2 + a_3(\lambda)r^3, \tag{2.3}$$

where λ_0 is the tuned central wavelength [Å], r is the distance from the optical center in arcminute, while a_3 is a third-order term defined as

$$a_3(\lambda) = 6.0396 - 1.5698 \times 10^{-3}\lambda + 1.0024 \times 10^{-7}\lambda^2. \tag{2.4}$$

This dependence is then used in the flux calibration process.

Another characteristic of the TF images are the spurious objects (or ghosts). These appear as a consequence of multiple internal reflections of the light from bright objects. One family of ghosts are the diametrical ones. Since position of these type of ghosts is always symmetrical to the bright source that causes it, dithering pattern of consecutive images help to detect and remove these ghosts after combining individual frames.

2.1.2 OTELO's TF observations

A selected region of Extended Groth Strip was targeted (see Figure 2.3) with the TF mode of the OSIRIS instrument, in particular the RTF. The selected

spectral range, between 9070 Å and 9280 Å, was observed using the tomography scan technique. This spectral window was carefully selected in order to avoid the Meinel bands of the night emission features (see left panel Figure 2.4). The RTF width of 12 Å with 6 Å scan step between consecutive slices were selected in order to be able to separate [N II]λ6583 (hereafter [N II]) contribution from Hα emission lines (Lara-López et al. 2010b). For each central wavelength setup of RTF, six images were taken with a cross-shape dithering and an exposure time of 1100 seconds each. A total of 216 individual science images were observed. After reduction and alignment of the individual images for each RTF setup (i.e. images with the same central wavelength) a total of 36 tomography slices were obtained. The co-addition of the RTF slices provided a deep detection image OTELO$_{deep}$ from which a total of 11 273 raw detections were extracted providing the OTELO source catalogue (for details see Bongiovanni et al. 2019). For each detected source the aperture photometry on the flux calibrated tomography slices were used to construct intermediate-resolution ($\sim$ 700) pseudo-spectra (PS). We refer to these as PS because each flux point is affected by the Airy transmission profile peculiar to the the Fabry-Pérot interferometers. An example of the PS is shown on the right panel of Figure 2.4.

Since the TF images posses a certain characteristics (as described in Section 2.1.1) the reduction process has its own specificity. We refer to Bongiovanni et al. (2019) for details on the reduction, alignment, flux calibration and the OTELO$_{deep}$ image construction.

2.1.3 OTELO's multi-wavelength catalogue

The wealth of the data in EGS enables to create a uniform multi-wavelength data base. The OTELO source catalogue, with OTELO$_{deep}$ photometry was used as a base for this multi-wavelength catalogue. Employing this catalogue it was possible to estimate the photometric redshift and the stellar mass of selected sources, among other parameters.

The All-wavelength Extended Groth Strip International Survey (AEGIS, Davis et al. 2007) compiles as much information as available for the EGS field. These panchromatic data set spans from X-ray to radio spectral range. The OTELO survey makes an intensive use of the AEGIS data-base to build the multi-wavelength catalogue. Figure 2.3 shows the available multi-wavelength data in EGS.

OTELO core catalogue

The process of the multi-wavelength catalogue assembly was done in two steps. The first step was to construct a "core" catalogue which includes optical to NIR data. The core catalogue was made up with the OTELO$_{deep}$, Canada-France-Hawaii Telescope Legacy Survey (CFHTLS, T0007 release) in *u', g', r', i', z'* bands, *HST*-ACS in F606W and F814W, and WIRcam Deep Survey (WIRDS, T0002 release) in J, H, Ks photometric data. The images from these surveys, scientific and weight maps, were re-processed (i.e., flux-conserving pixel resampling to the OTELO spatial resolution, astrometrically calibrated to CFHTLS i'-band image, and trimmed to the OTELO's FoV) in order to provide consistent photometry in all given filters. After extensive simulations explained in Bongiovanni et al. (2019), a `DETMODEL` photometry from `SExtractor` software (Bertin & Arnouts 1996) was employed.

Auxiliary data

The second step consisted in an educated cross-matching of the core catalogue with publicly available auxiliary data, in order to expand the spectral coverage of the OTELO multi-wavelength catalogue, as well as to add existing redshift information.

Photometric auxiliary catalogues

A total of five auxiliary photometric catalogues were cross-matched. These cover the spectral range from X-rays, through UV, and mid-IR, to far-IR.

In the X-rays catalogues from Pović et al. (2009) and Laird et al. (2009) were used, both based on the data from Chandra Data Archive[1]. After cross-match of both databases, a total of 42 common sources were found in the OTELO field. For these sources we prioritize the tabulated information from Pović et al. (2009). Additionally to the 42 common sources, further 32 sources found in Pović et al. (2009), and 8 found in Laird et al. (2009) were complemented with X-ray data. Thus a total of 82 OTELO sources have X-ray detection.

In the UV spectral range, the data from Galaxy Evolution Explorer telescope (GALEX, Martin et al. 2005) were used. The retrieved bands cover near-UV and far-UV. From a total of 5185 in the OTELO field a match was found for 4223 sources.

In the case of mid and far-IR spectral range *Spitzer* and *Herschel* data were

[1] `https://cxc.cfa.harvard.edu/cda/`

used. A total of 2128 sources were matched from Barro et al. (2011) with *Spitzer*-IRAC in 3.6, 4.5, 5.8 and 8 μm filters. Further data for 503 sources selected with 24 μm *Spitzer*-MIPS emission, observed with *Herschel*-PACS in 100, and 160 μm described by Lutz et al. (2011) were added. Finally, far-IR data for a total of 749 sources from Roseboom et al. (2010) observed in 250, 300, and 500 μm with *Herschel*-SPIRE were also included.

Redshift auxiliary catalogues

Since the emission line identification of the OTELO emitters is mainly based on photometric or ancillary spectroscopic (when available) redshifts, this is an essential piece of information. Thus, two available redshift catalogues were also matched and included in the final OTELO multi-wavelength catalogue.

The CFHTLS T0004 Deep3 photo-z catalogue (Coupon et al. 2009) contains data for more than 500 000 sources in the total area of 0.83 degree square. Limiting this catalogue to the OTELO's FoV, a total of 7725 sources were found. From these, 4860 were matched to the OTELO core catalogue.

The second redshift catalogue was the DEEP2 Galaxy Redshift Survey (Newman et al. 2013). Spectroscopic information for more than 50 000 sources preselected using broad-band CFHT images are included in DEEP2. From these, there are 517 sources which falls within the OTELO field, while a total of 461 sources were matched.

2.1.4 Photometric redshifts from OTELO data

The OTELO multi-wavelength photometric catalogue described above was used to estimate photometric redshift $z_{\rm phot}$. Reliable $z_{\rm phot}$ is especially important for the sources with detected emission line in their PS, which often is the only spectral information available. To obtain $z_{\rm phot}$ we used `LePhare` code (Arnouts et al. 1999; Ilbert et al. 2006). This code performs χ^2 fitting of a set of given templates to input SED. In this process we adopted the Calzetti et al. (2000) extinction law ($E(B-V)$ in the range of 0 and 1.1), setting the redshift range between 0.04 and 10.

Three different template libraries were employed to derive the OTELO's $z_{\rm phot}$. The first one, with galaxy templates contains four standard Hubble types E/S0, Sbc, Scd, and Irr from Coleman et al. (1980) and six starburst templates from Kinney et al. (1996) with a broad span of UV-slope (β). These are shown in Figure 2.5. The second library consist of AGN/QSO templates from SWIRE[2]

[2] *Spitzer* Wide-area InfraRed Extragalactic survey.

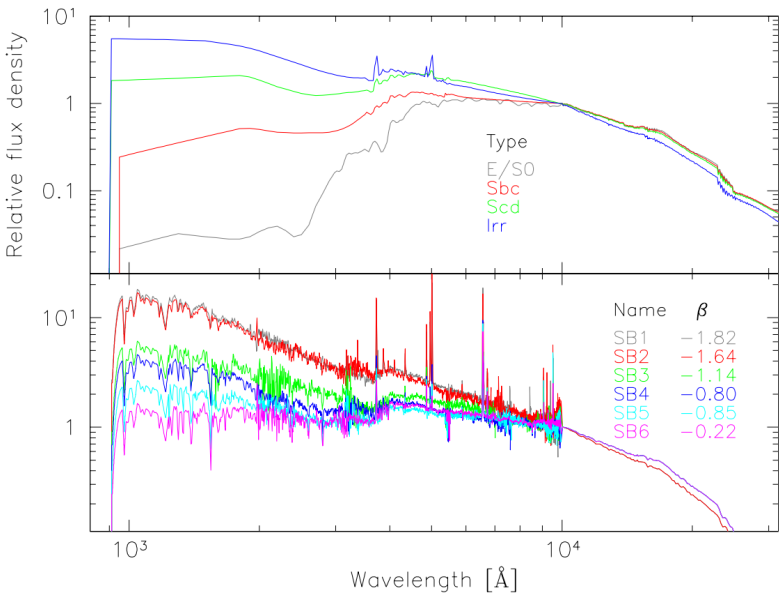

Figure 2.5. Templates of the galaxy library used in this work. *Top panel:* templates of standard Hubble type galaxies E/S0, Sbc, Scd, and Irr from Coleman et al. (1980) *Bottom panel:* six SFGs templates from Kinney et al. (1996) with a different of UV-slope (β). Figure taken from Bongiovanni et al. (2019).

library with two Seyfert, three type-1 and two type-2 QSOs and three composite (starburst+QSO) templates created by Polletta et al. (2007). Finally, the third library consist of the 131 star templates from Pickles (1998), four white dwarfs from Bohlin et al. (1995), and with further 26 brown dwarfs from the SpeX Prism library[3]. Altogether, the star templates covers a wide range of spectral types as well as the luminosity classes.

The `LePhare` code was executed two times for each library. The first one includes broad-band photometry described in previous Sections (from NUV GALEX data, to 500μm from SPIRE). In the second run the OTELO$_{deep}$ photometry was added.

For the purpose of this work we make a use of the $z_{\rm phot}$ solution for the galaxy library only. The final best solution was obtained by the analysis of the best χ^2 obtained together with the estimated redshift error, $\sigma_{\rm Zphot}$, defined as

$$\sigma_{\rm Zphot} = |\texttt{Z\_BEST\_LOW\_deepX} - \texttt{Z\_BEST\_HIGH\_deepX}|, \qquad (2.5)$$

where `Z_BEST_LOW_deepX` and `Z_BEST_HIGH_deepX` (as labeled in the OTELO catalogue) are the 1σ deviations of the estimated redshift for the given object,

[3] `http://pono.ucsd.edu/~adam/browndwarfs/spexprism/`

while `X` stands for `Y` or `N`, including or excluding the OTELO$_{deep}$ photometry in the SED fitting, respectively. We select $z_{\rm phot}$ with lower $\sigma_{\rm Zphot}$, with the additional requirement that

$$\sigma_{\rm Zphot} < 0.2 \times (1 + \texttt{Z\_BEST\_deepX}), \tag{2.6}$$

where `Z_BEST_deepX` is the photometric redshift. We refer to these selected $z_{\rm phot}$ solution as $z_{\rm best}$, and to their associated templates as SED$_{\rm best}$. We further use these templates to provide an ET/LT classification. We consider ET sources with SED$_{\rm best}$ of E/S0, while we label as LT galaxies with remaining SED$_{\rm best}$ templates from galaxy library. This classification is used in order to check the information derived from the parametric method described in next Chapter.

2.1.5 Summary

In summary, a total of 11 273 raw sources (i.e. including possible spurious detections) were extracted from the OTELO$_{deep}$ image. For each of the detected source a pseudo-spectrum, or PS, is constructed from the tomography scans of RTF images. The PS reaches limiting line flux of 4.6×10^{-19} erg s^{-1} cm^{-2} (Bongiovanni et al. 2020), what makes OTELO the deepest survey to date, in terms of the emission line flux. The OTELO$_{deep}$ photometry was complemented with spatially resampled archival data, and PSF-matched to the OTELO's resolution photometry available in EGS. Together these data allowed to build the OTELO multi-wavelength photometric catalogue with *X*-ray to far infra-red (FIR) wavelength coverage. Furthermore, photometric and spectroscopic redshift information was included in the final OTELO catalogue. All data described above are recompiled in our graphic user interface (GUI) available at the project website[4] and are publicly available.

In this work, we refer to the data from the OTELO multi-wavelength catalogue as the low-resolution (or low-res) ensemble in order to distinguish it from the high-resolution *HST*-ACS data used to provide the morphological catalogue. This is particularly important in Section 4.2.

2.2 Complementary data

Complementary data described in this Section were used to derive morphological parameters, and to build samples of selected sources for comparison purposes.

[4] `http://research.iac.es/proyecto/otelo`

2.2.1 *HST*-ACS images

The high-resolution images from *HST*-ACS in F606W and F814W (hereafter V- and I-bands, respectively) are used in this thesis. A total of 11 (overlapping with the OTELO survey field) *HST*-ACS tiles were retrieved from AEGIS data base in its native pixel scale of 0.03 ″/px and average resolution of $\sim 0\farcs15$. These high-resolution data were acquired in HST Cycle 13 GO program 10134 (PI: M. Davis). In short, *HST*-ACS images were already processed with standard ACS pipeline (including bias subtraction, gain and flat-field correction) and a Python-based multi-drizzle package (Koekemoer et al. 2003) was applied to combine all exposures in a simgle mosaic (including registration, median image creation, identification of cosmic rays and its removal). For the purpose of this thesis we provide our own astrometric correction of all the *HST* tiles used, as described in the next section. These were further used to construct the high-resolution mosaic image.

Astrometric correction

The *HST*-ACS data are used to provide a morphological catalogue, complementary to the OTELO survey data-products. Thus, we had to align the *HST*-ACS images to the same reference catalogue as used in the OTELO survey, i.e., to the CFHTLS D3-25 i'-band source catalogue. This astrometric correction is necessary not only to provide homogeneous celestial coordinates of objects detected on OTELO$_{deep}$ image and its counterparts from high-resolution data, but also in our further analysis of morphological parameters. The initial astrometric offset between all of the 11 tiles used and CFHTLS catalogue were found to be different. This is showed in Figure 2.6, where we can see the astrometric shift of individual tiles. Thus we decided to provide a homogeneous astrometric correction for each tile separately to the CFHTLS D3-25 i'-band catalogue before proceeding to the mosaic assembly.

The selection of objects suitable for astrometry correction is important because of differences in the resolution between CFHTLS catalogue (resolution $\sim 0\farcs6$ with pixel scale of 0.186 ″/px) and *HST*-ACS data (with resolution of $\sim 0\farcs15$ and pixel scale of 0.03 ″/px). This selection was based on (i) CFHTLS i'-band magnitude (≤ 24.5), (ii) `SExtractor` parameters `CLASS_STAR` ≥ 0.9 (for both images: *HST* I-band and CFHTLS i'-band), and (iii) `FLAG` $= 0$ for only *HST*-ACS high-resolution data. Furthermore, from these we have selected visually a total of ~ 370 point-like, isolated source, quite uniformly distributed on the OTELO field (~ 33 objects per *HST* tile) as the final astrometric reference catalogue.

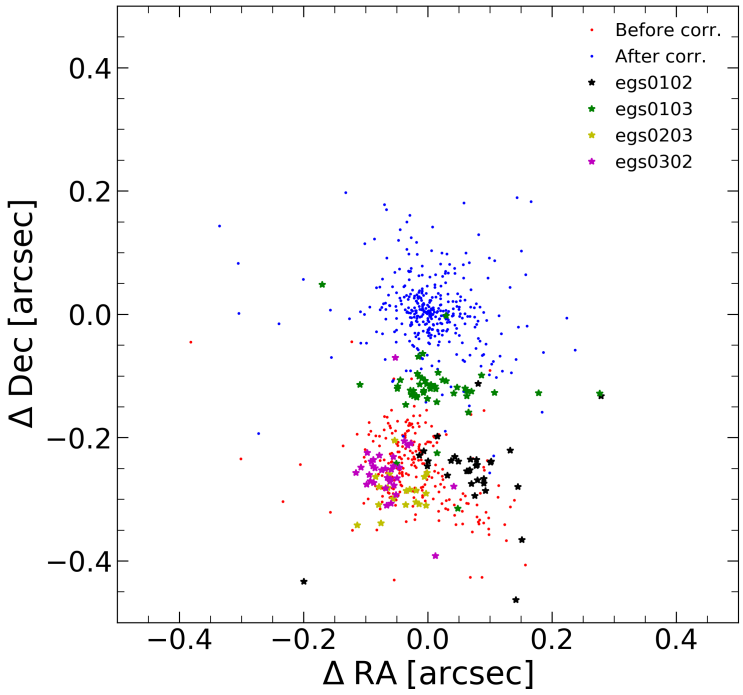

Figure 2.6. Difference in position of the selected point-like sources used in astrometric correction. Red and blue dots show position before and after correction. Coloured star-markers show the position of the selected point-like objects in the individual *HST* tiles. For clarity only four tiles are shown (star-shaped marks).

The astrometric reference catalogue was cross-matched with a detected source catalogue, which corresponds to each individual *HST* I-band tile, using `IRAF ccxymatch` task. The astrometric solution was obtained using `IRAF ccmap`, adopting a third-order polynomial geometry with standard `TNG` projection. The accuracy of our astrometric solution in standard coordinates ξ_I and η_I are: $0\farcs016$ and $0\farcs013$, respectively. This gave us an offset of $0\farcs021$ for the whole set of the *HST*-ACS I-band tiles – i.e. the sub-pixel accuracy in high-resolution *HST* data with respect to CFHTLS D3-25 i'-band catalogue. The registration process of *HST* V-band images was based on the already aligned I-band data. Internal (i.e. between *HST* V- and I-band images) astrometric offset is $0\farcs002$.

The final mosaic of scientific and weight (inverse variance) maps were obtained with `SWarp`[5] software (Bertin et al. 2002). These were trimmed to the field of OTELO$_{deep}$ image with additional $\sim 3''$ per side in order to provide morphological analysis of the objects which are near the borders of the effective

[5] `http://www.astromatic.net/software/swarp`

OTELO FoV.

2.2.2 ACS-GC catalogue

In order to compare our results of the morphological analysis we make a use of ACS-GC catalogue described in Griffith et al. (2012). The ACS-GC catalogue is a photometric and morphological catalogue of about 470 000 sources from AEGIS, COSMOS, GEMS, and GOODS surveys, i.e., compiling all the big surveys carried-out with *HST*-ACS. This catalogue is based on the same data as described in Section 2.2.1, i.e. high-resolution data from *HST*-ACS in the F606W and F814W bands (quite equivalent to the Johnson V and I bands, respectively). Because of the method used to provide morphological parameters in ACS-GC (i.e., with `GALFIT` software, in contrast to `GALFIT-M` used in our work; see Section 3.1.2) we can provide a quantitative comparison of the common sample found in both, OTELO and ACS-GC catalogues.

2.2.3 Sloan Digital Sky Survey

In this work we make an extensive use of the data products from SDSS (York et al. 2000) data release 8 (DR8), in order to prepare low-redshift comparison samples (as in the case of the data sets described in the following sections). In particular, we employed the data collected in the MPA-JHU[6] catalogues. From these catalogues, we retrieve emission line properties from Brinchmann et al. (2004), rest-frame fiber and Petrosian photometry from `photoPlate` table to compute aperture corrections, and finally, stellar masses were taken from Kauffmann et al. (2003b).

SDSS Morphological catalogue

In Chapter 5 we make a use of the morphological catalogue from Domínguez Sánchez et al. (2018) to select a sample of local ET-ELG. In their work, a total of 670 000 galaxies from SDSS were classified using deep learning technique into T-type and visual-like classification scheme. Using for a training set of visually classified galaxies from Nair & Abraham (2010) and from Galaxy Zoo 2 (Lintott et al. 2008; Willett et al. 2013), this catalogue provide reliable morphologies for a fairly complete sample (90% completeness of the parent sample, see Meert et al. 2014) up to $z \sim 0.1$.

[6] `https://www.sdss.org/dr12/spectro/galaxy_mpajhu/`

2.2.4 Galaxy and Mass Assembly survey

In Chapter 6 we additionally make a use of the Galaxy and Mass Assembly (GAMA, Driver et al. 2011) data-products. The GAMA survey is a spectroscopic survey of about 300 000 galaxies selected from SDSS covering ~ 286 deg^2. The data were acquired using the AAOmega fibre-fed spectrograph facility on the 3.9-m Anglo-Australian Telescope. The limiting flux of $r_{\rm petro}$ $\sim$19.5 mag is reached as stated in Driver et al. (2011).

2.2.5 VIMOS VLT Deep Survey

We also use VIMOS VLT Deep Survey (VVDS) and VVDS Ultra-Deep[7] data products (Le Fèvre et al. 2013). The VVDS sample selection is based on the i-band magnitude limit of 24.75 [AB]. Spectra for $\sim$35 000 sources are available up to redshift $z\sim$ 6.7. We use a selected sample of SFG to compare our finding on SFR and sSFR. The selection and further comparison with our work are presented in Chapter 6.

[7] `http://cesam.lam.fr/vvds/index.php`

3

Methods

In this Chapter we introduce methods and software employed in this thesis. Details on setup parameters are given, as well as examples of performance are showed.

3.1 GALAPAGOS-2

Along the thesis we have used GALAPAGOS-2 (Galaxy Analysis over Large Areas: Parameter Assessment by GALFITting Objects from SExtractor) to derive morphological parameters of the OTELO galaxies. This IDL-based[1] software was developed by the MegaMorph group[2] and is full described in Häussler et al. (2013). GALAPAGOS-2 is a new version of GALAPAGOS originally written by Barden et al. (2012). This software employs two well known applications: SExtractor (Bertin & Arnouts 1996), and GALFIT (Peng et al. 2002, 2010) to detect, and to fit a chosen parametric profile to each source, respectively.

In Section 3.1.1 and 3.1.2 brief description of SExtractor and GALFIT-M (a multi-wavelength version of GALFIT) are given. We chose this software due to its fully automatic operation: it extract sources through SExtractor, prepares initial GALFIT-M values and run it, reads-out the result for each source, and prepares a final catalogue. Furthermore, it handles the sky background estimation and the issue of neighbouring sources in an accurate and efficient way (Häussler et al. 2013). One of the most important characteristic is that GALFIT-M fits

[1] Interactive Data Language

[2] https://www.nottingham.ac.uk/astronomy/megamorph/

simultaneously the selected model to all given bands (and thus we refer to this version as multi-wavelength) using selected Chebyshev polynomial functions. The simultaneous performance increases stability of the fitting process, increasing the number of analysed sources, especially those with low S/N ratio (as will be showed in Section 4.2.3). `GALAPAGOS-2` has been successfully used in several low- and high-redshift studies of surveys (e.g., Barden et al. 2005; Krywult et al. 2017), on different environmental conditions (e.g., Kuchner et al. 2017). This is also true for its multi-wavelength version `GALFIT-M` (e.g. Vulcani et al. 2014; Vika et al. 2015).

3.1.1 `SExtractor`

The `SExtractor` application was developed by Bertin & Arnouts (1996), an it is designed to *"optimally detects, de-blends, measures and classifies sources from astronomical images"*, as stated in their work. Its robustness and speed made it a widely used software. Furthermore, easy implementations can be done to wrap it with virtually any programming language (Python, or IDL – as in the case of `GALAPAGOS-2`). `SExtractor` performance can be described in the following steps: *"estimation of sky background, thresholding, deblending, filtering of the detections, photometry, and star/galaxy separation"*.

In this work (as well as in the OTELO core catalogue assembly) a dual `SExtractor` mode was used. The dual mode is used to provide homogeneous aperture photometry measurements on several filters. In this mode, one photometric band is selected to be a detection band on which all decisions are made, in particular aperture for photometry. Afterwords, the same apertures are applied for remaining bands. In the case of the morphological analysis using the high-resolution *HST*-ACS images we selected the *I*-band (F814W) as the detection band. In this thesis we used `SExtractor` in version 2.19.5.

High-dynamical range mode of `SExtractor`

Following Rix et al. (2004), the so called high-dynamical range (HDR) mode was used in order to maximise the source detection, as implemented in `GALAPAGOS-2`. The HDR mode uses two separate `SExtractor` runs with different configurations. The first one (so-called hot run), is optimized to detect faint sources, while the second one (cold run) is optimized to detect bright sources. In Table 3.1 we show the values of relevant parameters associated to hot and cold run. Both, hot and cold runs, are executed in the dual mode described above. After the hot and cold runs, `GALAPAGOS-2` takes care of matching both (hot and cold) catalogues in such a way that hot detections inside of a defined ellipse of a cold

Table 3.1. Main configuration parameters used in SExtractor HDR run.

Parameter	hot	cold
DETECTED_MINAREA [px]	5	5
DETECT_THRESH [σ]	1.8	6.0
ANALYSIS_THRESH [σ]	1.6	6.55
FILTER_NAME	gauss$^{(a)}$	tophat$^{(b)}$
DEBLEND_NTHRESH [branch]	64	64
DEBLEND_MINCONT [fraction]	0.005	0.002
BACK_SIZE [px]	128	256
BACK_FILTERSIZE [px]	5	9
BACKPHOTO_TYPE	LOCAL	LOCAL
BACKPHOTO_THICK [px]	48	100

$^{(a)}$gauss_4.0_7x7; $^{(b)}$tophat_5.0_5x5

detection are not included. Examples of the cold and hot detection apertures are shown in Figure 3.1.

Since GALAPAGOS-2 keeps the SExtractor measurements only for the detection band, we have performed a separate run with exactly the same parameters in dual, HDR mode in order to obtain parameters for the V-band filter. Obtained parameters are used to provide $(V - I)$ colour, and the concentration index $c_{90/50}$ (i.e. the ratio of the radii containing 90% and 50% of the flux).

3.1.2 GALFIT-M

GALFIT originally developed by Peng et al. (2002) is a two-dimensional source fitting software. It is designed to provide accurate model of the light distribution of selected objects. The advantage of this software is that multiple components (or models) can be fitted simultaneously if necessary, e.g., to provide a bulge-disc decomposition, or to fit a neighbouring sources. Various models are available such as Nuker law, Sérsic profile, and Gaussian or Moffat functions. As in the case of SExtractor, this software is easy to include in a wrapping script such as GALAPAGOS.

In this work, we have used GALFIT-M – a new version of GALFIT, as implemented in GALAPAGOS-2 and developed by MegaMorph group. This new version fits simultaneously a selected model to the given sources in all the available bands by applying a linear Chebyshev polynomial. In our case the Sérsic (1968) profile was fitted to all the detected sources in the I-band and the second avail-

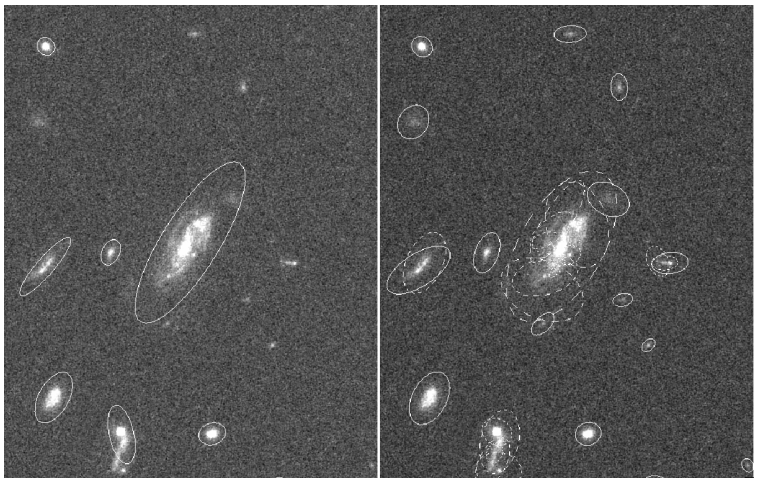

Figure 3.1. Example of detection apertures from `SExtractor` cold (left panel) and hot (right panel) run. Central sources correspond to the OTELO object `id:5298`.

able *HST*-ACS *V*-band. The Sérsic profile is defined as

$$I(r) = I_e \exp\{-b_n[(r/r_e)^{1/n} - 1]\}, \tag{3.1}$$

where r_e is the effective radius (i.e., radius containing 50% of the total flux), I_e is the intensity at r_e, n is the Sérsic index and b_n is a function of n as defined in Ciotti (1991).

3.1.3 `GALAPAGOS-2` performance

In this Section we briefly describe the way `GALAPAGOS-2` works, including important details for this thesis. For greater technicalities we refer to Häussler et al. (2013) and references therein.

`GALAPAGOS-2` is a single-setup script which run `SExtractor` to provide a guess values for `GALFIT-M`. Since `GALFIT-M` fit a single galaxy at once, a stamp or cutout for the galaxy in the question is prepared. The size of the stamp is defined in terms of semi-major axis a, Kron-radius $kron$, position angle ϕ, and ellipticity $ellip$ parameters from `SExtractor` (`A_IMAGE`, `KRON_RADIUS`, `THETA_IMAGE`, `ELLIPTICITY`, respectively). The size of the stamp is defined by the following equations:

$$x_{\text{size}} = 2.5 \times a \times kron[|sin(\phi)| + (1 - ellip) \times |cos(\phi)|] \tag{3.2}$$

$$y_{\text{size}} = 2.5 \times a \times kron[|cos(\phi)| + (1 - ellip) \times |sin(\phi)|]. \tag{3.3}$$

Such definition of the size should be adopted (Häussler et al. 2007) in order to keep the stamp small enough to make the fitting process reasonably fast, while providing enough background sky for robust sky level estimation.

After the stamp is created, the decisions on the secondary source fitting (neighbouring sources) are made on the basis of the SExtractor detection ellipses enlarged by a user-selected factor. All the sources with ellipses which overlaps with the primary source are fitted with a single-Sérsic model, while pixels of other sources (even if their central positions are not in the stamp) are masked.

In the next step the sky background is estimated from the SExtractor aperture map of the whole field, masking the contribution of the source in question, as well as the neighbouring objects. Sky values are measured in consecutive elliptical rings centered at the primary source with the user-defined width. Mean values of the six last rings are fitted with a linear function and the process stops if user-given slope of the fit is reached. The final sky value is estimated as the mean value of these six sky background values of the outer ellipses.

The initial guess values for GALFIT-M are automatically prepared for each source separately. These are based on the SExtractor source catalogue described above. The initial values are given in the following list:

1. Magnitude $mag_{\rm input}$ is given by MAG_BEST,
2. effective radius $r_{\rm e}$ is given by $0.162 \times$ FLUX_RADIUS$^{1.87}$,
3. ellipticity a/b is defined as $1 -$ ELLIPTICITY,
4. position angle ϕ is given by THETA_IMAGE, and
5. stamp center position (x, y) is estimated using the size of the stamp and position of given source in the whole image X_IMAGE and Y_IMAGE in pixels.

Apart for the initial guess values defined above, the constraint values are defined by the user. These constraints assure that during the fitting process the algorithm will explore only the physically meaningful parameter space, saving CPU time. In our work we followed the recommendations from Häussler et al. (2007, 2013), thus we set constraint values as follow (mostly default values):

1. position of the primary object has to lay inside of the image cutout (hard-coded into GALFIT-M),
2. Sérsic index: $0.2 < n < 8$,

3. effective radius: $0.3 < r_{\mathrm{e,GF}} < 400$ [px]; GF stands for the `GALFIT-M` output,
4. modeled magnitude: $mag_{\mathrm{input}} - 5 < mag_{\mathrm{GF}} < mag_{\mathrm{input}} + 5$, mag_{GF} is the output magnitude fitted with `GALFIT-M`. A further constraint of $0 < mag_{\mathrm{GF}} < 40$ is set to ensure rational values.
5. axis ratio: $0.0001 \leq Q \leq 1$, even if limits $0 \leq Q \leq 1$ are hard-coded in `GALFIT-M` (based on the recommendation given by Häussler et al. 2007),
6. position angle: $-180° < PA < 180°$ (hard-coded into `GALFIT-M`),
7. time limit of the fitting was set to not exceed 10 minutes.

During the `GALFIT-M` fitting we fixed the center position of source to the input values `X_IMAGE` and `Y_IMAGE` I-band position, while linear Chebyshev polynomial function was used to fit magnitudes, effective radius r_{e}, and Sérsic index n, all over both *HST*-ACS input bands.

The resulting catalogue contains multiple morphological parameters for all the sources. On the basis of the constraint values a sample with good results can be defined to provide robust analysis (see Section 4.2). In addition to the morphological catalogue, `GALAPAGOS-2` provides the 2D model and the residual image together with original stamp of the galaxy.

3.2 Visual classification

Complementary to the parametric morphology (via `GALAPAGOS-2`) we also provide a visual classification. Since a comprehensive visual classification of a large sample of galaxies is a time-consuming task, in this thesis we show preliminary results.

To provide the visual classification we made use of a Perl-based graphic user interface MorphGUI developed by Kocevski (2015). The MorphGUI was previously used in the CANDELS survey (Grogin et al. 2011) to classify ∼10 000 galaxies down to H-band magnitude 24.5 (Kartaltepe et al. 2015) by at least three independent individuals. MorphGUI display the galaxy stamp in all given filters together with segmentation map from `SExtractor` using DS9 (Joye & Mandel 2003). Multiple flags are then available to be checked in the interface in order to classify the source. Once the classification is done the answers are saved in the output catalogue.

For the purpose of this work I have modified the MorphGUI (with a permission of the authors). The fundamental change was for the so-called "main

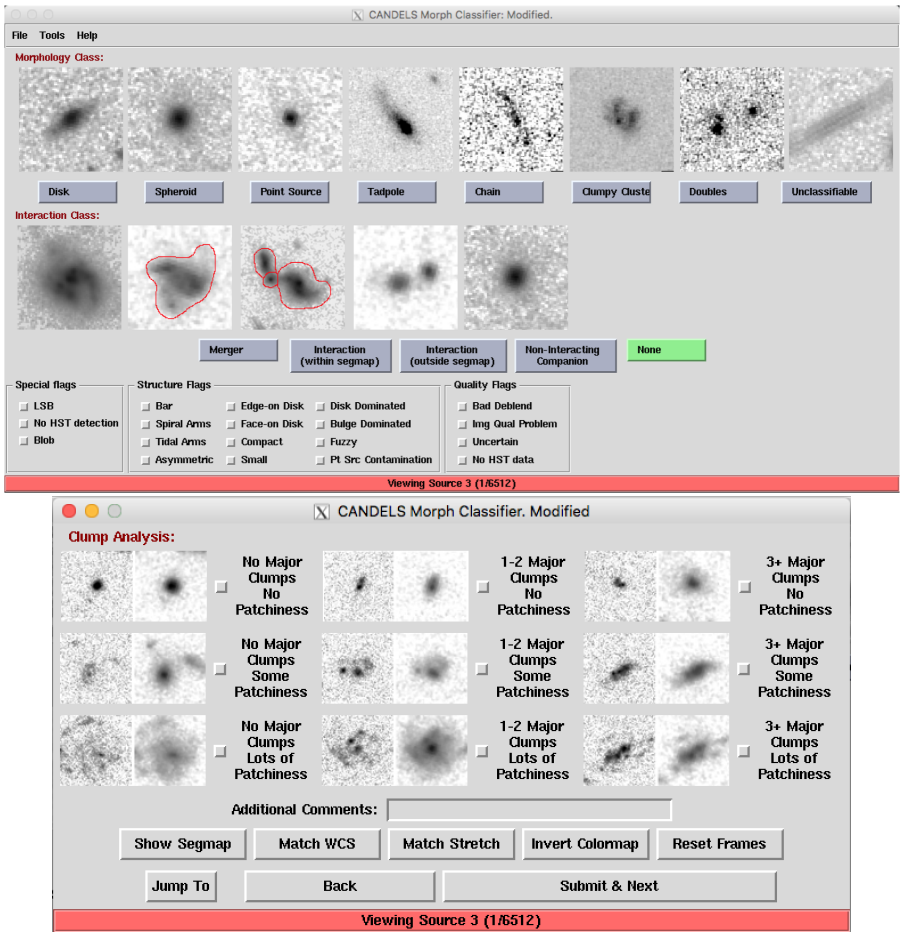

Figure 3.2. MorphGUI graphic user interface. *Top panel:* main morphology class, and interaction class are showed. Examples of each morphologies and interactions are displayed; specific flags showed in the lower part of this panel are available to be eventually selected. *Bottom panel:* Clump analysis. This window enable to select the clumpiness of the sources, as well as to navigate through the GUI (e.g., save the classification task, change to another object, etc.).

morphology class". In the original GUI the following classes were available: disk (D), spheroid (Sph), peculiar/irregular, point like/compact (PL), and unclassifiable (Unclass). In the modified version we have added several additional morphological classes, which were found to appear in the earlier epochs of the Universe, as showed in Elmegreen et al. (2007). These are: tadpole (T), chain (C), clumpy cluster (CC), and doubles (DD). Thus, in total there are eight morphology classes. Along the main morphology class, the interaction class, and clumpiness flags are also available. In a top panel of Figure 3.2 we show

the main morphology class window, together with interaction class, and several different type of possible flags (special, structural, and quality flags). Examples of the morphologies and interaction classes are showed for each type. The clump analysis window is showed on the bottom panel in the same figure, also including examples for each type.

Results of the visual classification of the OTELO selected sub-sample are described in Chapter 4, in particular in Section 4.4.

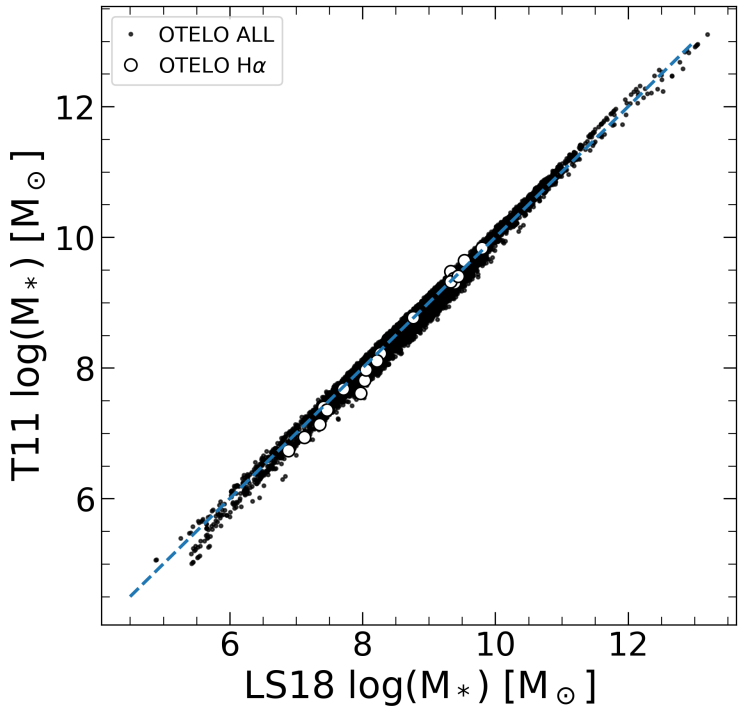

Figure 3.3. Estimated stellar masses for overall OTELO survey galaxies. A comparison between Taylor et al. (2011) and López-Sanjuan et al. (2018) methods is showed. Black dots show all the OTELO sources with estimated stellar mass. The blue dashed line represent 1:1 relation. Open empty circles shows the Hα sample studied in Chapter 6. Figure from Nadolny et al. (2020).

3.3 Stellar masses

Stellar masses M_* for the overall OTELO sample were computed using the López-Sanjuan et al. (2018) mass-to-light ratio for quiescent and SFGs defined by

$$\Upsilon_{\rm q} = 1.02 + 0.84(g - i) \tag{3.4}$$

$$\Upsilon_{\rm SFG} = 1.411 + 0.212(g-i) + 0.144(g-i)^2 \tag{3.5}$$

$$\log M_* = \Upsilon - 0.4 M_i, \tag{3.6}$$

employing rest-frame g- and i-band magnitudes, together with absolute i-band magnitude M_i. The rest-frame photometry was computed by shifting the $\rm SED_{best}$ (defined in Sec. 2.1.4) to $z = 0$, and calculating the flux below transmission curves for *g'*, *r'*, *i'*, *z'* (CFHTLS) and for the *HST*-ACS F606W and F814W filters. To estimate M_i we used $z_{\rm phot}$ associated with the used $\rm SED_{best}$. A second-order correction accounted for the Galactic dust extinction towards the EGS using the Galactic dust map from Schlafly & Finkbeiner (2011).

The associated stellar mass uncertainty was computed making use of the `propagate`[3] sub-routine, included in the R software which makes an estimate of the error by a first- and second-order propagation of any input recipe, as well as by Monte Carlo simulations. The uncertainty quoted corresponds to the variance obtained from 10 000 Monte Carlo simulations using that sub-routine.

As showed in Figure 3.3, the stellar masses for the OTELO survey galaxies falls between 10^6 and 10^{12} $M_\odot$. About 55% of the sources have masses $M_* < 10^9$ $M_\odot$. This fact indicates that OTELO is quite sensitive to the low-mass regime. In the same Figure we also compare results of stellar masses estimated using method described in Taylor et al. (2011). Both methods are consistent, and in what follows we adopt as valid the mass estimations obtained from equations 3.4, 3.5, and 3.6.

3.4 Inverse deconvolution

Throughout this thesis we made use of the inverse deconvolution as the numerical method addressed to obtain valuable information from OTELO's pseudo-spectra (PS). This software was originally written by Á. Bongiovanni and M. Cerviño. Furthermore, a substantial part of this Section was published in Nadolny et al. (2020). Here we describe how this deconvolution is performed.

For a given PS we obtain (a) the maximum value of the PS $f_{\rm PS}^{\rm max}$ and its observed error $\sigma_{\rm PS}^{\rm max}$; (b) an estimate of the continuum level defined as the median flux of the PS $f_{\rm c}$, and the deviation $\sigma_{\rm med,c}$ around this value (mean of the square root of the differences around $f_{\rm c}$). We also have a redshift guess

[3] `https://cran.r-project.org/web/packages/propagate/propagate.pdf`

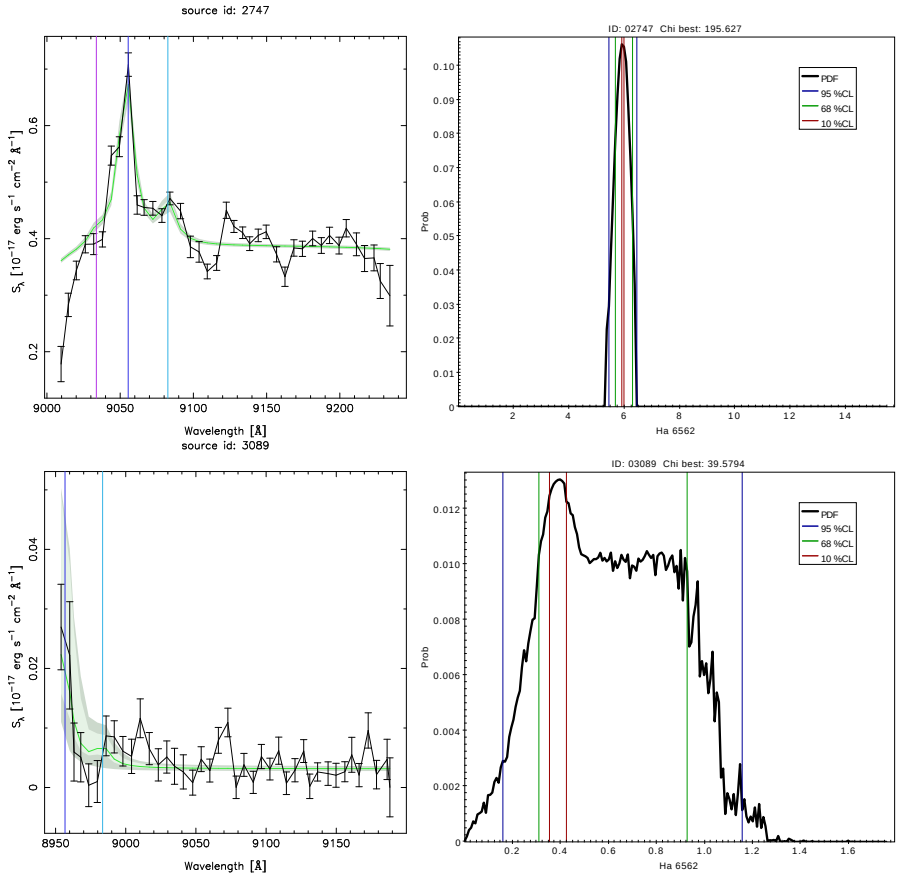

Figure 3.4. Inverse deconvolution of the Hα emission line source `id:2747` (top row) and `id:3089` (bottom row). *Left panel:* black thick line shows observed PS with error bars at each of the RTF tomography slices. Light green line represents best simulated pseudo-spectrum, while shaded light and dark green regions represent 25% and 68% confidence intervals. Figure from Nadolny et al. (2020). *Right panel:* Black line is the probability distribution function of the Hα line flux. Vertical lines shows 10%, 68% and 90% confidence intervals.

value $z_{\rm PS}$ that is obtained from visual inspection of the PS in our GUI web-based tool, and it is assumed to be accurate up to the third digit, that is, with an uncertainty $\Delta z = 0.001$. Finally, we define the wavelength region of the PS where the lines can be detected in such a way that it contains at least 2.5 RTF slices (15 Å being 6 Å the average width of the RFT) below and above the redshifted emission-line (EL). In the case of the emission line complexes (e.g., Hα + [N II]$\lambda\lambda$6548,6583, or [O III]$\lambda\lambda$4959,5007) the below and above wavelength limits are defined by the blues and the reddest rest-frame EL wavelength for a given complex. For example, in the case of Hα + [N II] complex these limits are

defined by

$$\begin{aligned} \lambda_{\rm min} &= 6548 \cdot (1 + z_{\rm PS} - \Delta z) - 15 \\ \lambda_{\rm max} &= 6583 \cdot (1 + z_{\rm PS} + \Delta z) + 15, \end{aligned} \tag{3.7}$$

where 6548 and 6583 are the rest-frame wavelengths of the blue and the red [N II] components in Å, respectively.

We assumed a model spectrum as a rest-frame spectrum defined by Gaussian profiles of the given emission lines (individual or multiple) defined by their amplitudes and a common line width for all lines, and a constant continuum level. The model to be compared with the observational data is therefore defined by following parameters for the case of Hα + [N II] complex: $f_{\rm mod}(z, f_c, \sigma_{\rm line}, f_{\rm H\alpha}, f_{\rm [N\ II]\lambda6583})$, taking into account possible constraints (e.g., the rest-frame $f_{\rm [N\ II]\lambda6548}$ was fixed to $1/3 \cdot\ f_{\rm [N\ II]\lambda6583}$). We note that there is an intrinsic assumption that this type of model is correct and that there is no additional component in the PS. In the case of other emission lines or other complexes of lines the fluxes ($f_{\rm [N\ II]\lambda6548}, f_{\rm H\alpha}$, and $f_{\rm [N\ II]\lambda6583}$) are correspondingly modified.

We performed 10^6 Monte Carlo simulations over the model parameter space using values of $z_{\rm PS}$, $f_{\rm c}$, $\sigma_{\rm med,c}$, $f_{\rm PS}^{\rm max}$, and $\sigma_{\rm PS}^{\rm max}$ to constrain the parameter space (see below) and provide the basis for the determination of the uncertainties. In each simulation the model was convolved with the RTF filter system used in the observations, and a synthetic PS $f_{{\rm PSmod},i}$ for each of the N slices of the PS was obtained. This synthetic PS was compared with the observed PS, and a likelihood distribution function is obtained.

First 30% of simulations (300 000) were made with following priors:

1. The redshift z follows a flat distribution in the range $z_{\rm PS} \pm 0.001$.
2. The dispersion of the line, $\sigma_{\rm line}$, varies following a flat distribution from 20 to 500 km/s. This value is used for all the modelled lines.
3. The continuum value follows a flat distribution in the interval [MAX(0, $f_{\rm c} - \sigma_{\rm med,c}$), $f_{\rm c} + \sigma_{\rm med,c}$].
4. The rest-frame emission line flux varies following a flat distribution in the interval $[f_{\rm c}, f_{\rm max}]$, where $f_{\rm max}$ is given by

$$\begin{aligned} f_{\rm max} =& (f_{\rm med,c} + f_{\rm PS}^{\rm max} + \quad 3\,\sigma(f_{\rm PS}^{\rm max})) \cdot \\ & \sigma_{\rm line\,max} \cdot (1 + z_{\rm max}) \cdot \sqrt{2\pi}. \end{aligned} \tag{3.8}$$

5. Further specific priors for particular emission lines were imposed, e.g.: the $f_{\mathrm{N\ II}\ \lambda 6548}$ line flux is fixed to $1/3 \cdot f_{\mathrm{N\ II}\ \lambda 6583}$.

When these 300 000 simulations were obtained, we computed a preliminary likelihood function. This likelihood was sampled in a regular interval with 200 bins over the range in which each parameter varied.

This likelihood function was marginalized for each parameter (i.e. we made a projection of the probability density function, PDF, on each particular parameter and the corresponding PDF was normalized). We obtained the marginalized likelihood using a regular interval of 200 bins over the range in which each parameter varied, and we obtained the range that contains 99% of the simulations around the value with the maximum likelihood. The next 20% (200 000) of the simulations were restricted to the parameters that sample this 99% confidence interval. This process was repeated five more times (using 10% (100 000) of the simulations at each step) with the limits obtained by the 85%, 75%, 68%, 40%, and 10% confidence intervals around the most probable value.

After this process we had a final PDF shape for each parameter, as well as all the required additional quantities such as the EWs, the emission line fluxes, etc. We note that the asymmetry of the PDF implies that the mean and the standard deviation (squared of the variance) are not informative to describe the distribution. For this reason we used the statistical mode of the resulting PDF as the reference value, and we obtained the region around the mode that included 10%, 25%, 50%, 68%, and 90% of the area. Along this thesis the error bars show the 25% and 68% confidence interval, which also gives an idea of the asymmetry of the associated distribution. Figure 3.4 shows examples of the deconvolved PS (in this case both sources are Hα emitters `id:2747, 3089`) as well as the PDF of the Hα line flux. As can be seen, in the case of `id:3089`, the PDF is not symmetric thus a simple median, or mean would not properly account for obtained asymmetric probability of a particular parameter's value.

4

Morphology classification

This Chapter presents the study of the OTELO survey galaxies in the context of their morphology. After a brief introduction we show the results of our parametric method applied to carefully selected sample. Furthermore, we also present the preliminary results of the visual classification of a magnitude limited sub-sample. In this Chapter we also compare our approach using multi-wavelength version of `GALFIT` with the method used to derive the ACS-GC catalogue with standard version of `GAFLIT`. This Chapter is based on the accepted article Nadolny et al. (2021, A&A accepted, DOI:10.1051/0004-6361/202037861).

4.1 Introduction

Galaxy morphology is related with other physical properties like star-formation, dynamical histories, stellar mass, colours, luminosities and different morphological parameters (Kauffmann et al. 2003b; Baldry et al. 2004; Salim et al. 2007; Pović et al. 2013; Schawinski et al. 2014; Mahoro et al. 2019). Since Hubble (1925) discovered the extragalactic nature of some "nebulae", the first step for tackling their systematic study was to establish a morphological classification. Hubble (1926, 1936) proposed the widely known *tuning-fork* classification scheme, further extended by de Vaucouleurs system (de Vaucouleurs 1959), who incorporated the numerical stages as well. A graphic representation of the *tuning-fork* is showed in Figure 4.1. Soon it was realized that ellipticals and spirals had different photometric and dynamical properties. Ellipticals were usu-

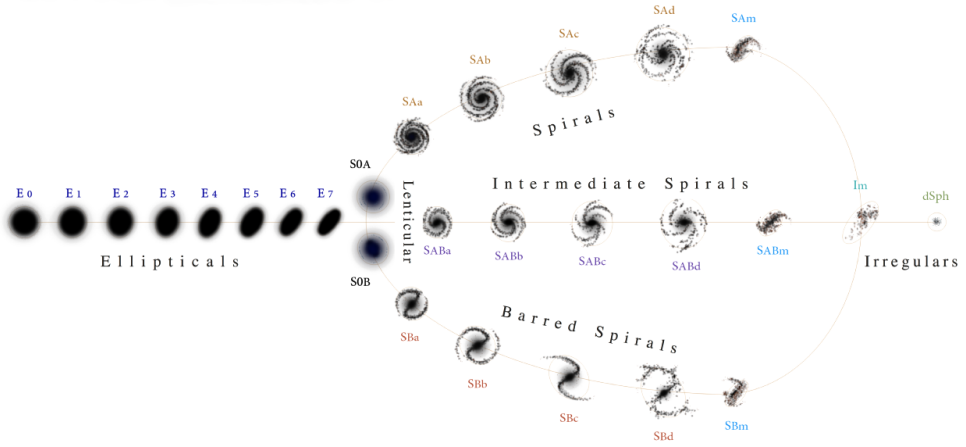

Figure 4.1. Hubble-de Vaucouleurs classification scheme. Figure by Antonio Ciccolella and M. De Leo.

ally defined by red colours, a de Vaucouleurs radial profile (Kormendy 1977), and mainly sustained by the velocity dispersion; while spirals were bluer, with a radial profile composed of a de Vaucouleurs plus an exponential disk (Freeman 1970), and dynamically sustained by rotation velocities. As a consequence, elliptical galaxies were compliant with a "fundamental plane" (Dressler et al. 1987) while spirals obey a Tully-Fisher relation (Tully & Fisher 1977). Then, morphology is directly linked to physical and chemical properties of galaxies, and ultimately to their evolution. In particular, the stellar-mass–size relation (MSR) has been studied for several decades, and it has been shown that the galaxy size not only can vary significantly with stellar-mass and morphology, but also evolves with redshift depending on these two parameters (e.g., Kormendy & Bender 1996; Shen et al. 2003; van der Wel et al. 2014; Lange et al. 2015; Roy et al. 2018; Mowla et al. 2019). For instance, early-type (ET) galaxies are typically more compact for the same mass, and more massive for the same size, than the late-type (LT) galaxies at a given redshift. These differences reflect different processes of the size growth in time (see Mowla et al. 2019, and references therein).

The way the classification has been done in times of Hubble changed mostly because of the amount of the available data. Large galaxy collections, at different redshifts provided by the rich surveys (e.g., SDSS, VVDS, COSMOS) have required the use of new methods involving less human interaction. Even if visual classification may results in more accurate description of the particular galaxy,

for tens of thousands of even millions of galaxies in modern sky surveys it is expensive in terms of the manpower. Furthermore, the final classification depends on the classifier experience. Two great examples of the visual classification are the work by Nair & Abraham (2010) and Kartaltepe et al. (2015). In the work by Nair & Abraham a total of 14 034 galaxies were visually classified. Their sample consist of almost all (to date of their work) SDSS spectroscopic targets ($g < 16$ mag) in the redshift range between 0.01 and 0.1. The classification scheme adopted in their work is fairly complex and complete where, apart of the standard Hubble types, the additional features as bars, rings, and lenses (among other) were also recorded. In the work by Kartaltepe et al. (2015) a total of 65 individuals classified more than 10 000 galaxies from CANDELS with redshift up to $z = 4$, with at least three, and up to five individual classification per galaxy. In this process they used the GUI detailed in Section 3.2.

In order to take advantage of the huge amount of data in today's surveys, different classification techniques were developed. For example, the statistical power of surveys have confirmed the colour bi-modality observed already in late 1930's (Humason 1936; Hubble 1936). Strateva et al. (2001) after analysing a sample of ∼150 000 galaxies from SDSS, have shown that using the $(u - r)$ colour it is possible to separate ET from LT galaxies (in a crude way). Later, more sophisticated methods were developed including automatic classification tools (e.g. Barden et al. 2012) and machine learning techniques (e.g., Huertas-Company et al. 2015; de Diego et al. 2020). Among these, two approaches stand out: non-parametric (Abraham et al. 1994, 2003; Conselice et al. 2000; Huertas-Company et al. 2008; Pović et al. 2013, 2015), and parametric based on galaxy physical (Peng et al. 2002, 2010; Simard et al. 2002, 2011; de Souza et al. 2004; Barden et al. 2012) or mathematical parameters (Kelly & McKay 2005; Ngan et al. 2009; Andrae et al. 2011a,b; Jiménez-Teja & Benítez 2012). Both methods depend greatly on the sensitivity of the data used (e.g. Häussler et al. 2007; Pović et al. 2015, and references therein).

The main advantage of the non-parametric methods is that they do not depend on any analytic form *a priori* and used information is obtained directly from the source images (i.e. concentration index, colour, asymmetry, Gini index, etc.). On the other hand, the main benefit of using a particular parametric function is that it can be extrapolated in the low S/N sources and can account for light at large radii (Häussler et al. 2007, 2013). Even being less flexible than non-parametric methods, and assuming that the chosen model correctly describes the light distribution, the parametric method is considered to be robust enough and feasible. In the particular case of the Sérsic profile, it has been used with success in previous studies (Simard 1998; Graham et al. 2005; Häussler et al. 2007, 2013).

It is important to note, that machine learning techniques (parametric or not) imply the necessity of a training set. The training set is a sample of previously classified objects used in order to train (or teach) the convolutional neural network or support vector machine. The training set has to be large and complete enough to reach desired accuracy. The visual classification is often used to provide such training set. For example, Huertas-Company et al. (2019) have used selected sample from the Nair & Abraham (2010) catalogue as the training set.

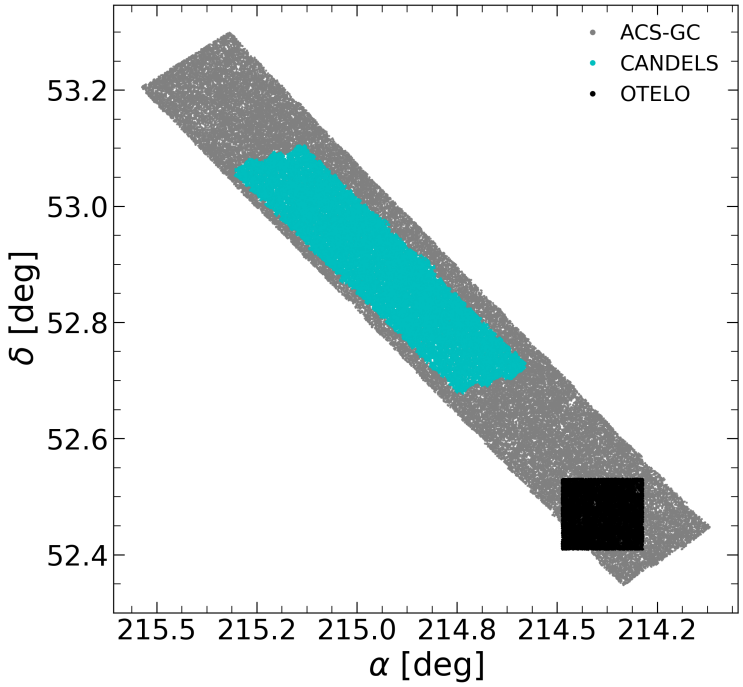

Figure 4.2. Spatial distribution of the morphological data available in EGS field. Data from ACS-GC (Griffith et al. 2012), CANDELS (Brammer et al. 2012), and the OTELO survey (Bongiovanni et al. 2019), are shown in gray, cyan, and black, respectively.

In this thesis we decided to use the parametric method implemented in `GALAPAGOS-2`, as described in Section 3.1, performing a single-Sérsic fit to detected galaxies in *HST*-ACS *I*-band images. While there are few morphological studies in the EGS field (Griffith et al. 2012; Brammer et al. 2012), the only overlapping with the OTELO survey field can be found in the work of Griffith et al. (2012, the ACS-GC catalogue, see Figure 4.2). The depth of the OTELO survey (27.8 AB on the OTELO$_{deep}$ image, see Bongiovanni et al. 2019) and the stellar-mass range (down to $\log M_*/M_\odot \sim$ 6, see Sec. 3.3 and Nadolny

et al. 2020) of the observed galaxies are the principal motivations to re-process the archival *HST*-ACS data, rather than employing morphological information from already published ACS-GC catalogue. Furthermore, as compared with ACS-GC catalogue, we analyze the *HST*-ACS data using newer version of the `GALFIT` software, namely its multi-wavelength version, the `GALFIT-M` (described in Sec. 3.1.2), where two *HST*-ACS bands are analysed simultaneously. This multi-wavelength version has been shown to produce more accurate, complete and meaningful results, especially in the low S/N regime (Häussler et al. 2013; see also Sec. 4.2.3).

4.2 Sample selection

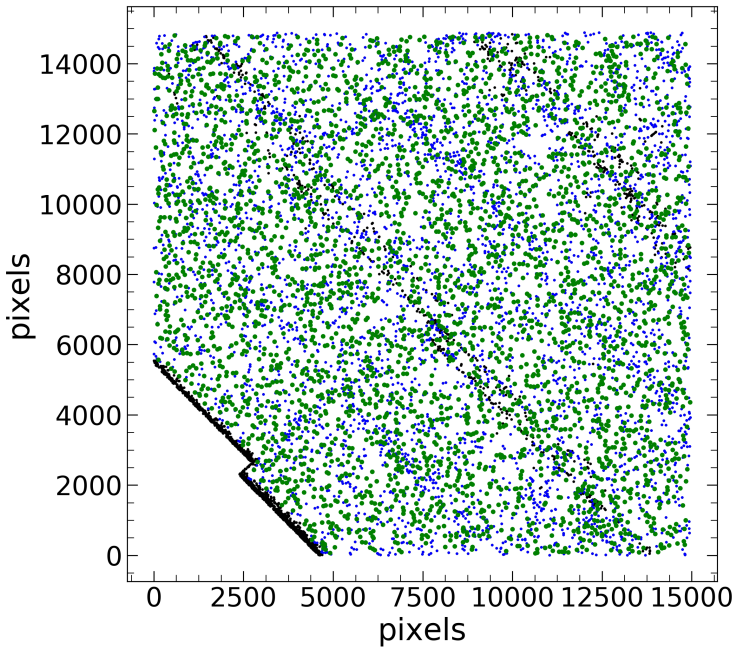

Figure 4.3. All detection from `SExtractor` dual HDR mode. Black dots represent non-real sources, or artifacts. Blue and green dots show sources with successful fit and with meaningful results, respectively. For details see Section 4.2.1.

The goal of this work is to assign a morphological classification to the largest possible number of the OTELO survey sources detected in the OTELO$_{deep}$ with counterparts in the *HST*-ACS images. Since the OTELO$_{deep}$ has lower spatial resolution than *HST*-ACS data used to provide the morphological catalogue, a careful match between both is essential. In the first part of this section we describe the "cleaning" process of the morphological `GALAPAGOS-2` catalogue

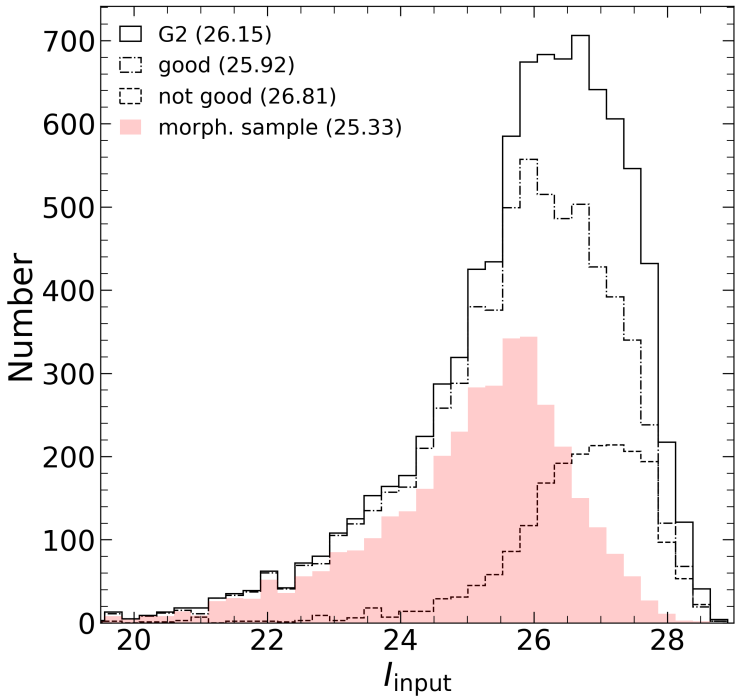

Figure 4.4. Magnitude completeness. Continuous and dot-dash histograms in black represent the G2 and the "good" samples, respectively. Dashed histogram in black shows the distribution of the sources removed from the G2 sample after the cleaning-out process (see Sec. 4.2.1). Red histogram show the distribution of the *morphological sample* (see Sec. 4.2.2). Magnitudes indicated in legend correspond to 50% completeness for each sample.

obtained from analysis of the *HST*-ACS data, while in the second part we explain the match and further selection of the galaxies, which are analysed in subsequent sections.

4.2.1 `GALAPAGOS-2` catalogue

Using `SExtractor` dual HDR mode (Sec. 3.1.1) we obtained 10 591 raw detections from *HST-I* band. A total of 1778 (17%) raw detections were visually selected as clearly not real objects. Such high percentage of non-real sources is because of: (i) the final mosaic of *HST*-ACS images (Sec. 2.2.1) still shows imperfections and artifacts, especially on the borders of individual images, as can be appreciated in Figure 4.3; (ii) the `SExtractor` parameters, listed in Table 3.1, were adjusted (via trial and error) to extract the maximum number of real sources, what on the other hand increase detection of spurious sources. If our

visual inspection omitted some of these bad detections, these were removed in the catalogue cleaning process described in what follows. The list of coordinates of these artifacts was passed to `GALAPAGOS-2` in order to omit them in the fitting process.

A total of 8812 (out of 8813) sources were successfully fitted by `GALAPAGOS-2` i.e., that `GALFIT-M` has not crush, or has not exceed the time-limit for the fitting process. We refer to this successfully fitted sources as G2 sample. The high rate of the successful fits is due to the visual inspection of the raw detections. The G2 sample, however, still contains sources for which one or more of the fitted parameters reached the constraint value (listed in Sec. 3.1.3) in one or both *HST*-ACS filters. Thus, these results are not necessarily meaningful. Using the criteria from Häussler et al. (2013, their Sec. 4.2) we identify sources with these not necessarily meaningful results and we do not include them in the further analysis. Here we list all the used criteria applied to both bands:

1. $mag_{\rm input} - 5 < mag_{\rm GF} < mag_{\rm input} + 5$, and $0 < mag_{\rm GF} < 40$,
2. $0.205 < n < 7.95$,
3. $0.301 < r_{\rm e} < 399$,
4. $0.001 < Q \leq 1$,
5. `FLAG_GALFIT`$= 2$.

We omitted the criterion (vi) from Häussler et al. (2013) due to our own star selection described in Bongiovanni et al. (2019). Applying those criteria we obtained a sample of 6780 sources with meaningful, or "good" results (i.e., 77% of G2 sample, similarly as reported in Häussler et al. 2013). The cleaning process of the morphological catalogue from not meaningful results guarantees quality results in the following analysis. As showed in Figure 4.4, this process removes the faint end of the G2 sample. The 50% completeness magnitude drops from $\sim$ 26.2 to $\sim$ 25.9 [AB] for the "good" sample. From now on we use the G2 "good" sample in the subsequent sample selection.

4.2.2 Match of `GALAPAGOS-2` and OTELO catalogues

We want to stress the importance of a reliable match between the results of the analysis of high-resolution *HST*-ACS images using `GALAPAGOS-2` and data from the OTELO catalogue, which are based on the low-resolution ground-based observations (photometry, photometric redshift, SED templates, ET/LT classification, and stellar masses, to name the relevant parameters used in this work; see Sec. 2.1 for details on the OTELO data-products).

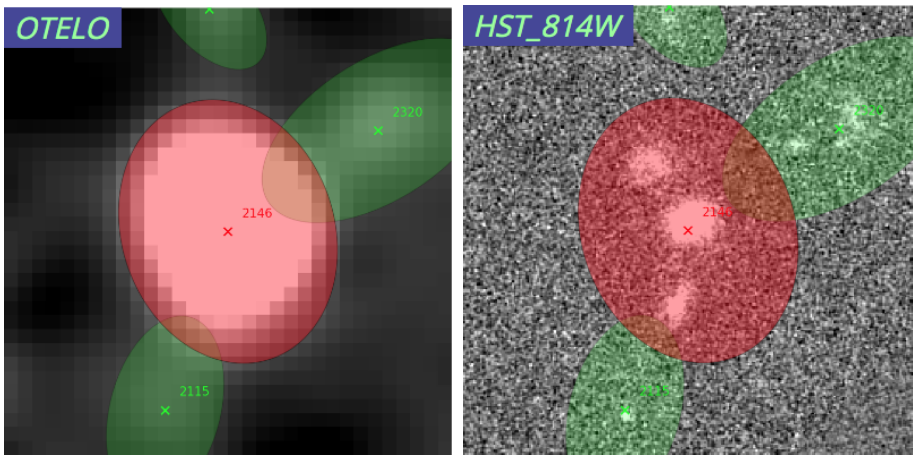

Figure 4.5. Example of a *multiple* source with central *multiple main* objects (these images are available in our web-based graphic user interface). *Left*: low-resolution OTELO$_{deep}$ image. *Right*: *HST* *I*-band high-resolution image. Ellipses in red (object in question) and green (neighbouring sources) show Kron ellipses from OTELO$_{deep}$ image for individual OTELO sources. The red ellipse shows the Kron ellipse corresponding to the source `id:2146`, inside which two additional sources (or well defined parts of a single galaxy) are visible. This particular source has three matched sources from *HST* image.

If we want to use any information derived from low-resolution data, we need to assure exact correspondence of the sources from high-resolution data. Due to the difference in spatial resolution, each source of the OTELO catalogue would admit one or multiple matches to the G2 sample. Hence, we checked the occurrence of one or more sources from G2 "good" sample inside of the OTELO$_{deep}$ detection ellipse (see example of multiple match in Figure 4.5; ellipses were calculated using `SExtractor` parameters: `A_IMAGE` $\times$ `KRON_RADIUS` in arcsec). In this match we got 5338 out of 6780 sources from the G2 "good" sample. At this point, we removed the objects which were preliminary classified as star candidates in the OTELO field (see Sect. 6.1 in Bongiovanni et al. 2019), what gives the total number of 5263 sources. Among these, there are 2780 *individual* or one-to-one matches (i.e., there is one source from G2 sample inside OTELO ellipse) between the G2 sample and the OTELO catalogue, while remaining 2483 sources are matched to 1295 OTELO sources, corresponding to the case where there are more than one source inside OTELO ellipse (e.g. Fig 4.5), and we refer to these as *multiple* matches. For each *multiple* match we selected one source which is the closest to the OTELO catalogued position and usually the brightest counterpart, and we refer to these as *multiple main*. A total of 1108 *multiple main* sources were selected. A good example of *multiple main* is the central source showed on the right panel of Fig. 4.5. This is a orthodox way

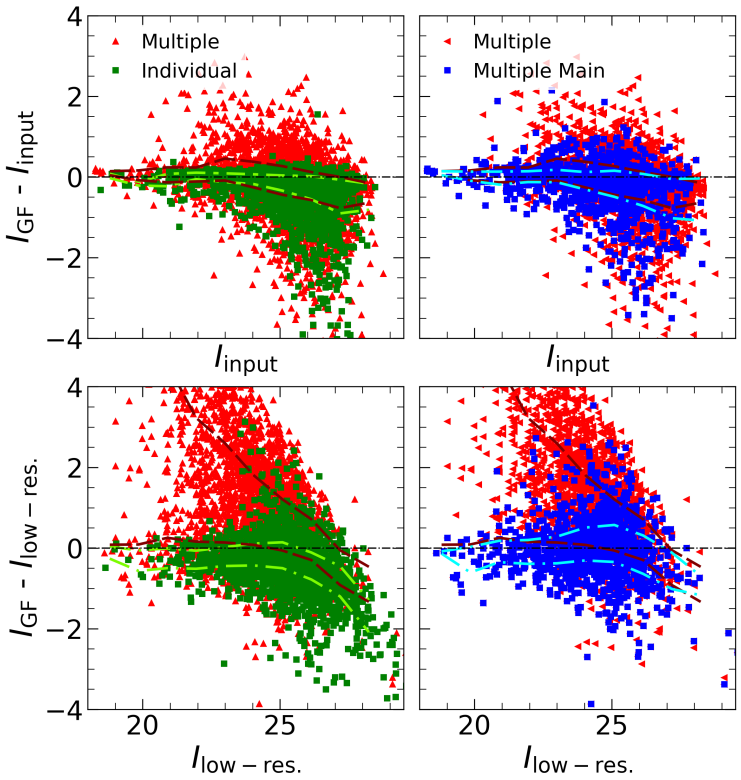

Figure 4.6. Magnitude comparison between low- and high-resolution data. Red up- and left-triangles show *multiple* sources, green squares show *individual* sources, while blue squares shows *multiple main* sources. Top row: comparison of *HST*-ACS input and `GALFIT-M` output I-band magnitudes. Bottom row: the same comparison as in top row, but instead of input high-resolution photometry we plot low-resolution *HST*-ACS-F814W photometry from OTELO catalogue. Lines represent the 25th and 75th percentile of the colour distribution per magnitude bin: light green dot-dashed - *individual*; dark red dashed - *multiples*; light blue dot-dashed - *multiple main*. See text for details on the samples selection (Section 4.2).

to select a fairly clean sample in order to use data obtained from low-resolution OTELO data-products such as $z_{\rm phot}$, ET/LT classification or stellar masses.

The visual inspection of the removed sources during the matching and cleaning out process reveals that these are in many cases point-like or very compact sources (possibly QSO), followed by those cases where interaction or merging sources are visible. There are also instances of sources which were excessively deblended by `SExtractor` (i.e. well resolved galaxies with more than one visible part). While many of these objects are interesting, the study of these require an individual attention, what is not the scope of this work.

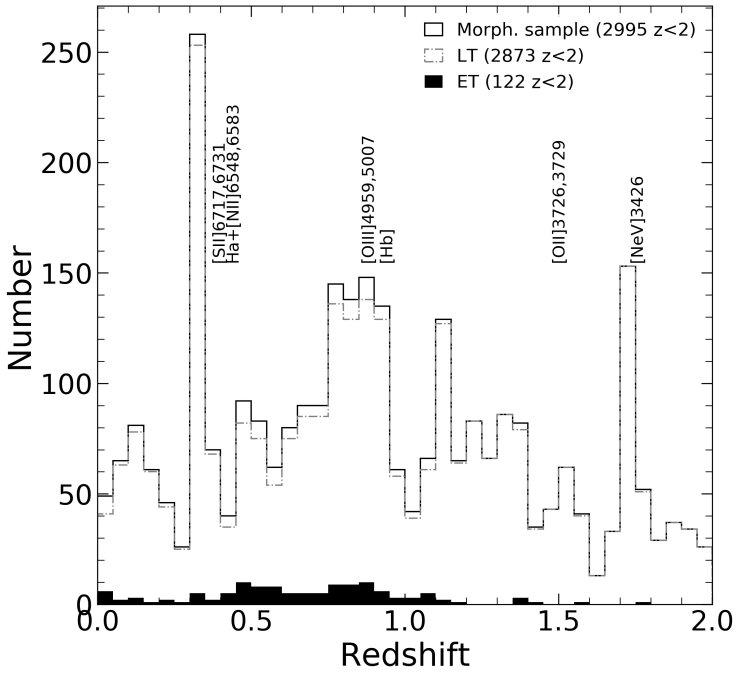

Figure 4.7. Redshift distribution of selected *morphological sample* (see text for details). Peaks in the distribution corresponds to specific emission lines, as seen in OTELO spectra range up to z=2. Solid black line shows all sources in *morphological sample*, gray dot-dashed line shows LT galaxies, while black filled histogram shows ET galaxies.

In Figure 4.6 we show the difference of the output `GALFIT-M` model magnitude ($I_{\rm GF}$) and the input high-resolution I-band *HST* photometry ($I_{\rm GF}-I_{\rm input}$), as well as the low-resolution photometric data of the PSF-matched *HST*-ACS I-band from OTELO catalogue ($I_{\rm GF}-I_{\rm low-res.}$). This figure illustrates the importance of the match and selection process described above. This figure shows *individual* (green squares) together with *multiple* matches (red up-triangles) on the left column, while *multiple* (red left-triangles) and selected *multiple main* (blue squares) sources on the right side. Considering upper-left panel, we can clearly see that for *individual* sources `GALFIT-M` returns the expected values. The dispersion (upper-left panel, green squares) of the magnitudes towards the brighter output `GALFIT-M` magnitudes is expected due to integration of the single-Sérsic model to the infinity (e.g., Häussler et al. 2007, 2013). While *multiple main* set (upper-right panel, blue squares) behaves in a similar way, their matched group members show larger dispersion. This is even more evident in the case of the low-resolution photometry (bottom row). Thus, even if on one hand we introduce bias in our sample selection, on the other hand we guaran-

tee the correspondence of the parameters from low-resolution data-base to the counterparts in high-resolution data.

On the basis of the source matching scheme described above, we focus on the meaningful results of the sources labeled as *individual* (2780) and *multiple main* sources (1108). This gives 3888 sources from which 3658 have $z_{\rm phot}$ solution from the OTELO catalogue, and 2995 have $z_{\rm phot}$ solution in the range $0 \leq z_{\rm phot} \leq 2$ (hereafter *morphological sample*). Figure 4.7 shows the redshift distribution of the *morphological sample*, with LT (2873) and ET (122) sources up to $z_{\rm phot} = 2$. The peaks of distribution correspond to redshifts at which the OTELO survey sees specific emission lines e.g., $z_{\rm phot} \sim 0.35$, 0.8, and 1.75 for Hα, [O III] and [Ne VI], respectively. As described in Section 2.1.4 we use $\rm SED_{best}$ template to provide ET and LT classification in order to compare it with derived parameters. We are aware of the possible misclassification of LT and ET using SED templates. However, de Diego et al. (2020) showed that less than 2% are misclassified using dense neural networks for the subset of the data used in this work (see their Sect. III.1.4). Thus, for the aims of this work, we consider the OTELO's classification as correct.

This restrictive selection process reduces dramatically the size of the final *morphological sample* (see Figure 4.4). However, in order to use parameters derived in previous works (PSF photometry, $z_{\rm phot}$, templates classifications associated to $z_{\rm phot}$, stellar masses and other OTELO-data products) this selection process is the most reasonable and responsible way to minimize possible biases due to the differences in the data used in the parameters estimation.

In order to provide visual classification we select sources from *morphological sample* with additional cut in $\rm OTELO_{\mathit{deep}}$ magnitude of 24.5 (following Kartaltepe et al. 2015). A total of 1467 sources were selected in this way. In Section 4.4 we present preliminary results.

4.2.3 Comparison with the ACS-GC catalogue

In this work we used the same data as previously analysed by Griffith et al. (2012, ACS-GC catalogue). We want to provide a quantitative comparison of the number of successfully analyzed sources. The ACS-GC catalogue is based on the standard `GALFIT` version, which treats all bands separately. On the other hand, the multi-wavelength version `GALFIT-M` implemented in `GALAPAGOS-2` and used in this work, allows to fit simultaneously data in all given bands using linear Chebyshev polynomial. This multi-wavelength version of `GALFIT` has been shown to be more robust for the low-S/N bands (Häussler et al. 2013). For the purpose of this comparison, we used a common sample composed of the matched sources from ACS-GC and our G2 sample (with 8812 objects, see Sect.

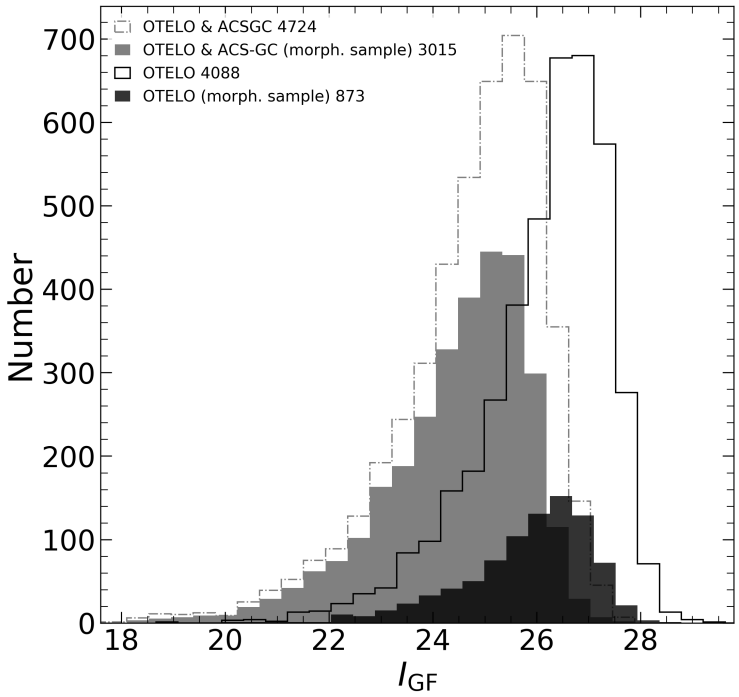

Figure 4.8. Magnitude comparison with Griffith et al. (2012). Step histogram in gray (dot-dashed line) shows the common sample distribution, while step histogram (continuous line) shows the distribution of remaining OTELO sources with no matched counterpart from ACS-GC (i.e., only found in OTELO). Filled gray and black histograms correspond to *morphological sample* (see Sect. 4.2.2) from common sample and without counterpart from ACS-GC (i.e., only found in OTELO), respectively. Numbers in the legend indicate the number of sources in the particular sub-sample.

4.2.1 for G2 sample definition). A total of 4724 sources were matched, and these constitute the common sample. Remaining 4088 sources from our G2 sample have no counterpart in ACS-GC (OTELO-only sample). The model-based I-band magnitude for both, the common sample and OTELO-only sample are showed in Figure 4.8.

Because the OTELO-only sample may still contain not meaningful results, we additionally show the magnitude distribution for each sub-sample which correspond to *morphological sample* defined in Section 4.2.2. From these sub-samples, a total of 3015 sources were found in common (with a median I-band magnitude $=$ 24.4), while remaining 873 were detected only in the OTELO catalogue (median I-band magnitude $=$ 26). We recovered a significant number of robust sources not presented in previous works, which fall into the faint-end of the magnitude distribution ($\sim$ 1.5 magnitude fainter).

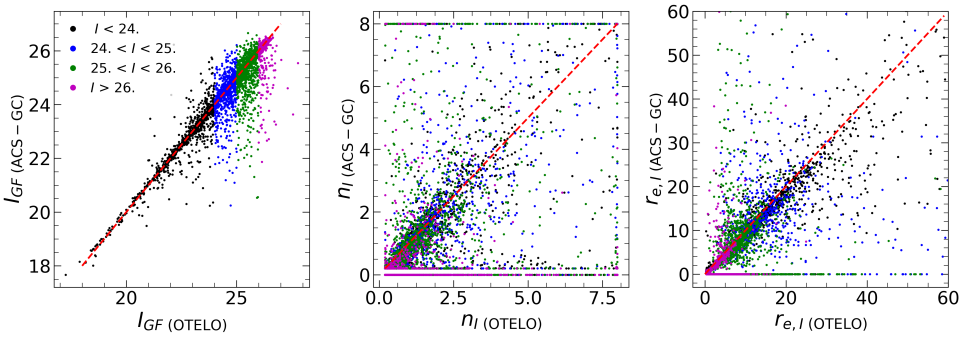

Figure 4.9. Comparison of the results from this work with those obtained by Griffith et al. (2012) for the common sample. From left to right: model-based I-band magnitude $I_{\rm GF}$, Sérsic index n_I, and effective radius $r_{{\rm e},I}$. Sources corresponding to each magnitude bin are colour-coded, as showed in the legend on the left panel. Red dashed lines represent 1:1 relation.

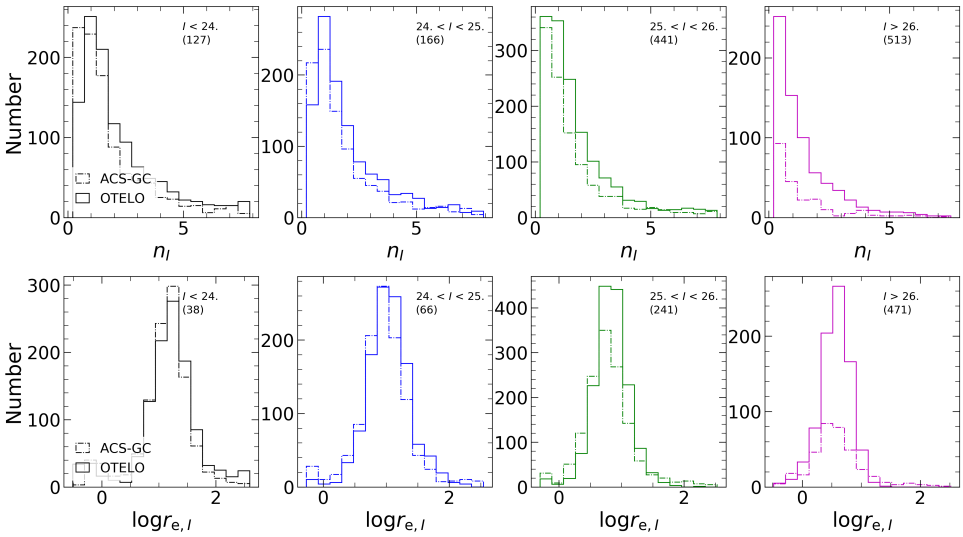

Figure 4.10. Comparison of the results from this work with those obtained by Griffith et al. (2012). Top row contains a comparison of the Sérsic index n_I distributions, while bottom row represents the logarithm of effective radius $r_{{\rm e},I}$. Each panel show a comparison for each magnitude bin indicated in the top-right corner. Numbers between brackets show the number of sources recovered in this work.

Regarding the common sample (4724 sources), in Figure 4.9 we show a comparison of model-based I-band results for magnitudes $I_{\rm GF}$, Sérsic index n_I, and effective radius $r_{{\rm e},I}$. In order to make our comparison sensitive to S/N, we divided the common sample into four magnitude bins ($I_{\rm GF} \leq 24$, $24 < I_{\rm GF} \leq 25$, $25 < I_{\rm GF} \leq 26$, and $I_{\rm GF} > 26$; colour-coded in all panels). Left panel shows the

magnitude comparison, and it is clearly visible that both catalogues are in good agreement. Middle, and right panel represents Sérsic index n_I, and effective radius $r_{e,I}$ for a direct comparison of both catalogues, ACS-GC and OTELO. In the middle panel, where n_I is represented, we can notice that a part of ACS-GC results is accumulated in three discrete values, i.e., at $n_I = 0$, around 0.2, and 8. These are the results for which `GALFIT` run into constraint values, and should not be considered as valid. While this is clearly visible for ACS-GC, much less sources are found at these constraint values among the OTELO results. The same is true for the effective radius r_e showed on the right panel, although less pronounced, as compared to the Sérsic index.

In Figure 4.10 we show histograms for n_I and $r_{e,I}$ per magnitude bins. In these histograms we include sources from the common sample after applying the criteria 2 and 3 listed in Section 4.2.1 (i.e., $0.205 < n_I < 7.95$, and $0.301 < r_{e,I} < 399$, removing in this way those sources with results that hit constraint values) for both catalogues. We indicate the difference of the sources in OTELO and ACS-GC for each parameter and bin (numbers between brackets) after applying mentioned criteria. As can be seen, for both parameters and all magnitude bins, OTELO has substantially more sources with meaningful results. The greatest difference is observed in the faintest bin, thus confirming that the multi-wavelength version of `GALFIT` used in this work is more robust, especially in the low S/N regime. Similar results are obtained for the remaining parameters, as well as for the V-band.

4.3 Morphology analysis

In this section we analyse the results of the parametric fitting method for *morphological sample* defined above. In this analysis we also include the Hα emission line sources studied in Chapter 6 in the context of the mass-metallicity relation. We represent the Hα sample as blue markers (circles or open circles) in the relevant figures.

Among the data returned by `GALAPAGOS-2`, there are model-based parameters like magnitudes (V_{GF}, I_{GF}), Sérsic indices (n), and effective radii (r_e, containing 50% of the model flux) for each input filter, i.e. *HST*-ACS I- and V-band. In the analysis are included also the parameters obtained from the separate `SExtractor` run, as described in Section 3.1.1 (e.g., those used to derive the concentration index), as well as stellar masses M_* described in Section 3.3 and in Nadolny et al. (2020).

Figure 4.11 shows the results of a linear discriminant analysis of model-based ($V_{GF} - I_{GF}$), and observed ($u - r$) colours performed to find the most

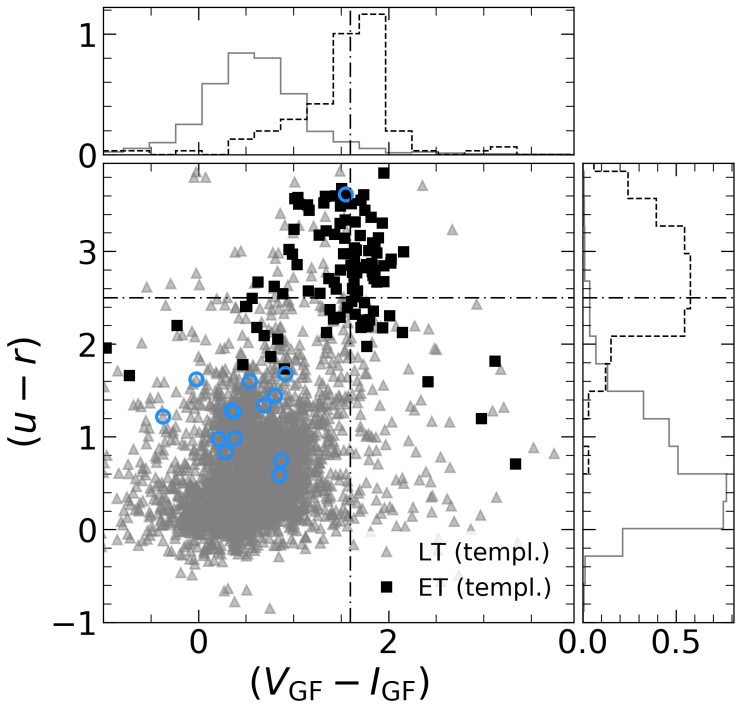

Figure 4.11. Comparison between $(V_{\rm GF} - I_{\rm GF})$ and $(u - r)$ colours. Triangles and solid lines in gray represent LT, squares and dashed lines in black correspond to ET galaxies. Top and right-hand density histograms correspond to $(V_{\rm GF} - I_{\rm GF})$ and $(u - r)$, respectively. Dot-dashed lines show the results of linear discriminant analysis of both colours with $(V_{\rm GF} - I_{\rm GF})$= 1.7 and $(u - r)$= 2.5. Blue circles represent the Hα sample studied in Chapter 6.

accurate ET/LT separation. We found cuts of 1.7 and 2.5 as the most accurate for $(V_{\rm GF} - I_{\rm GF})$ and $(u - r)$, respectively. Using these limits, we found an ET completeness and contamination of 39% and 63% for $(V_{\rm GF} - I_{\rm GF})$, and 62% and 35% for $(u - r)$, respectively. The small spectral separation of the filters used to calculate the $(V_{\rm GF} - I_{\rm GF})$ colour translates into the relatively poor separation of ET from LT galaxies, with a higher contamination of LT in the expected region for ET. The $(u - r)$ colour with larger wavelength separation, gives better results in terms of completeness and contamination. This figure shows that the $(u - r)$ is more adequate for ET/LT separation. The $(u - r)$ colour cut found in this work is higher than that reported by Strateva et al. (2001). and we attribute this difference to the redshift range of our sample. The high completeness ($> 97\%$) of LT in blue cloud is likely due to the selection process, where we cleared out the *morphological sample* from possible QSO/AGN and mergers/interacting galaxies, as described in Section 4.2.1. This is also visible

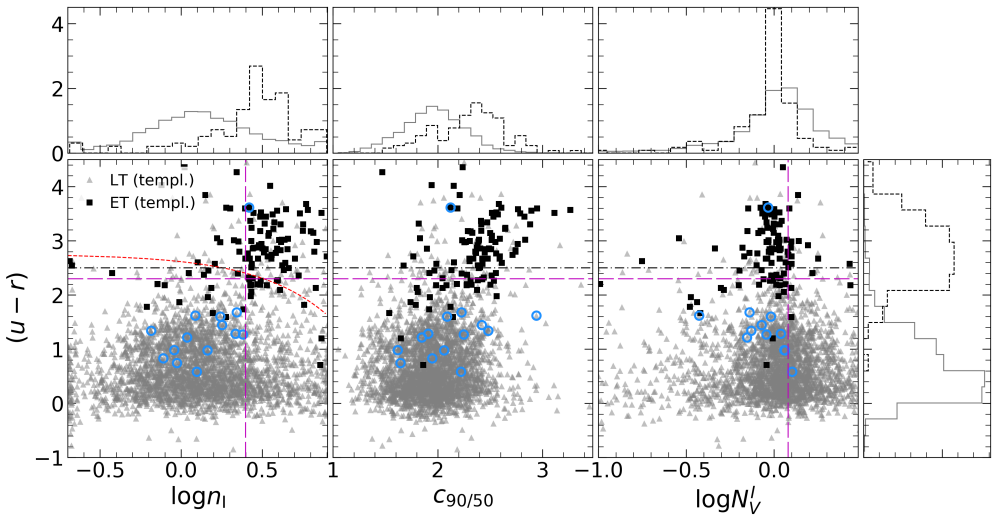

Figure 4.12. Observed $(u-r)$ colour as a function of morphological parameters. From left to right: Sérsic index n_I, concentration index $c_{90/50}$ and wavelength-dependent ratio of Sérsic indices N_V^I. Triangles and solid lines in gray (histograms) show LT, squares and dashed lines in black (histograms) show ET galaxies. Top histograms correspond to the respective value, as indicated in x-axis label, while right-hand histogram show the $(u-r)$ colour distribution. All histograms represent density distributions. Horizontal dot-dashed line in black shows $(u-r) = 2.5$. Red dashed line show linear discriminant analysis result from de Diego et al. (2020). Dashed lines in magenta represent the limits from Vika et al. (2015): vertical cut in $(u-r) = 2.3$, while on the left and right panels horizontal dashed-lines in magenta represent $\log(n_I) = 0.4$ and $\log(N_V^I) = 0.08$, respectively. Blue circles represent the Hα sample studied in Chapter 6.

for the case of the Hα sample – all but one are found in the blue cloud.

In order to make a second check, we used the criteria from Schawinski et al. (2014, their equation 1 and 2), to separate blue cloud, green valley and red sequence galaxies on the $(u-r)$ vs. stellar-mass plane. We found that $\sim$ 8% of our LT galaxies are in their red sequence, (as compared with 7% in their work, see their Table 1).

Left bottom panel of Figure 4.12 shows the Sérsic index distribution as a function of observed $(u-r)$ colour. The overall Sérsic indices fall in the expected ranges of values for ET and LT galaxies (top left histogram). The median values of n_I index are 1.3 ± 0.6 and 3.0 ± 0.9 for LT and ET, respectively. Uncertainties cited in this section are median absolute deviations. The increase of n from LT to ET is expected, since LT are disc-dominated (described with lower Sérsic index of $n \sim 1$) and ET are bulge-dominated (i.e. $n \gtrsim 4$) galaxies. A very similar

trend is observed for n_V (measured on V-band) with median values of 1.1 ± 0.6 and 3.0 ± 1.2 for LT and ET, respectively. V-band results are not shown for the sake of clarity. As can be seen in the same panel of Figure 4.12, there are two well defined regions occupied by red & high-n ET galaxies [$(u - r) > 2.3$ & $\log n > 0.4$] and blue & low-n LT galaxies [$(u - r) < 2.3$ & $\log n < 0.4$]. We found a ET completeness in the red & high-n zone of 59%, with a contamination of 30%. The completeness (and contamination) provided by this method according to Vika et al. (2015) is of 63% (53%) for their artificially redshifted sample (see their Table 1). In the same panel of Figure 4.12 we show the results of the linear discriminant analysis from de Diego et al. (2020). Using this discriminant for the *morphological sample* we found 98% and 66% of completeness for LT and ET, respectively.

The concentration index $c_{90/50}$, defined as ratio of `SExtractor` I-band flux radius containing 90% and 50% of the flux, is showed in the middle panel of Figure 4.12. The median values of I-band $c_{90/50}$ are 1.9 ± 0.2 and 2.4 ± 0.2 for LT and ET, respectively. Again, very similar median values are observed for V-band $c_{90/50}$ with 1.9 ± 0.2 and 2.3 ± 0.2 for LT and ET. As shown in previous works (e.g., Strateva et al. 2001), this parameter does not provide a good separation of ET/LT and it can only yields a crude classification.

The last parameter in Figure 4.12 (third panel) shows the the ratio of Sérsic indices in both *HST* bands $N_V^I = n_I/n_V$, as defined by Vika et al. (2015). This parameter, together with a colour term, is shown to be sensitive to the internal structure. Median values of N_V^I for LT and ET are 1.1 ± 0.4 and 1.0 ± 0.2, respectively. This indicates that the ET sub-sample is well defined around $N_V^I = 1$. This is an expected result because of the very nature of red ET galaxies which show less variation of the Sérsic profile with wavelength (e.g., Vulcani et al. 2014). Using cuts of $N_V^I < 1.2$ and $(u - r) > 2.3$, Vika et al. (2015) found 70% of completeness and 50% of contamination for ET galaxies. Here we report 60% of ET completeness with 42% of LT contamination using the same cuts in N_V^I and $(u - r)$.

4.3.1 Testing the mass-size relation

Using stellar masses M_* and physical sizes estimated using model-based flux radius r_e we can study the mass-size relation (MSR). In order to probe if there are any signs of evolution in MSR since $z = 2$, we divided our sample into three redshift bins or volumes (vol1: $z < 0.5$, vol2: $0.5 \leq z < 1$, and vol3: $1 \leq z < 2$). For each bin and for each morphological type we fit a single power–law of the form

$$r_e = a\,(M_*/M_\odot)^b. \tag{4.1}$$

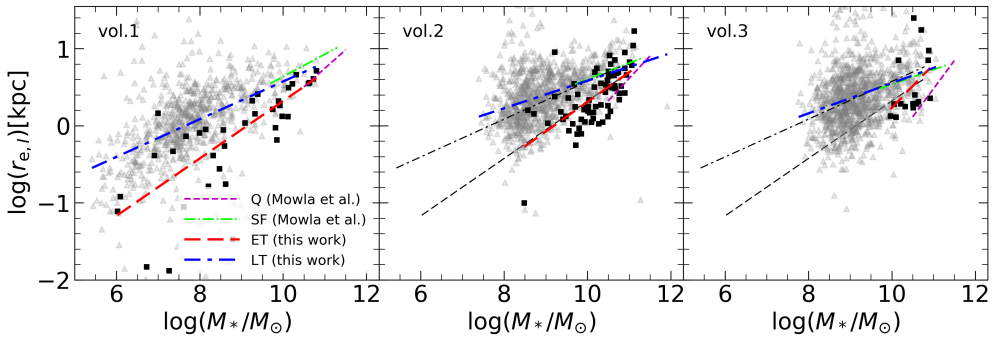

Figure 4.13. Effective radius as a function of stellar mass – the mass-size relation. Each panel correspond to selected cosmic volumes: $z < 0.5$, vol2: $0.5 \leq z < 1$, and vol3: $1 \leq z < 2$. Gray triangles and black squares show LT and ET galaxies, respectively. Dot-dashed blue and dashed red lines show power–law fits for LT and ET data, respectively, according to Eq. 4.1. The best-fit parameters are given in Table 4.1. Gray dot-dashed, and dashed lines in the middle and right panels show the fits for LT and ET obtained for the first cosmic volume (vol1). Dot-dashed green and dashed magenta lines represent the LT (SF) and the ET (Q) MSR, respectively, as reported by Mowla et al. (2019).

The parameters of the best-fitted functions for each cosmic volume, as well as median redshifts, are given in Table 4.1. These functions are represented in Figure 4.13. As can be seen, the slope of the relation fitted in this process do not vary significantly between different redshift bins for a given morphological type (the black lines in the middle and right panel in Fig. 4.13 show the fits from the first redshift bin). It is noticeable that, on one hand OTELO miss the high-mass end ($> 10^{11}\,M_\odot$) of the LT and ET galaxies, while on the other hand, there is also low statistics of the ET galaxies in the highest redshift bin (resulting in large errors in the best-fitted power–law, see Tab. 4.1).

As mentioned above, the OTELO survey was designed to recover the low-mass end of the field galaxy population. Indeed, in our MSR we can see that it extends toward lower stellar-masses if compared with previous works. In all panels of Fig. 4.13 we additionally represent the fits from Mowla et al. (2019) for star-forming (LT) and quiescent (ET) for the same redshift bins. Their separation onto star-forming and quiescent galaxies is based on U, V, and J rest-frame bands. For the purpose of the comparison, presented in what follows, this selection is compatible with our ET/LT separation (van der Wel et al. 2014). Our MSR for LT galaxies is consistent with those given by Mowla et al. (2019), even taking into account the differences in the mass range studied in both works. However, the slope obtained by these authors in the case of ET galaxies is stepper than the fitted in this work for all redshift bins, with

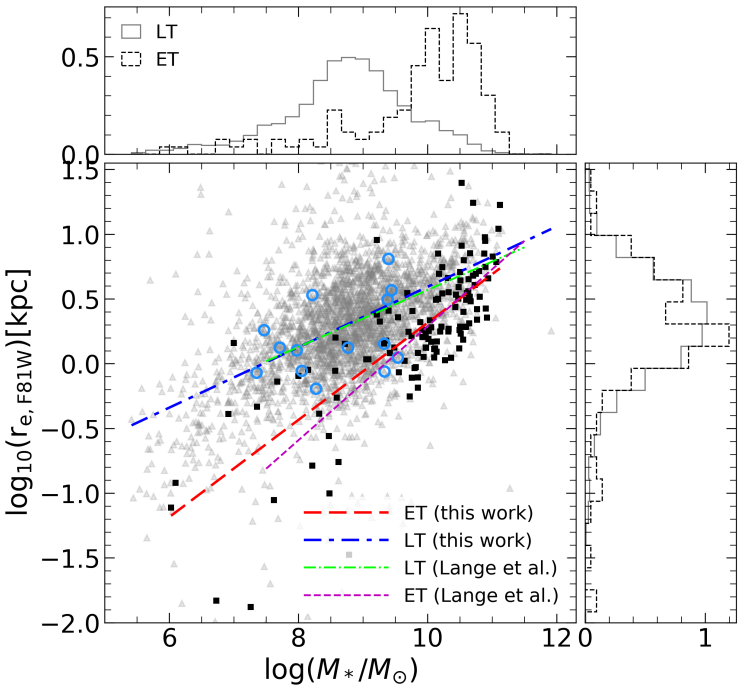

Figure 4.14. Effective radius as a function of stellar mass – the mass-size relation. Gray triangles and black squares show LT and ET galaxies, respectively. Dot-dashed blue and dashed red lines show the power–law fits for LT and ET data, respectively, according to Eq. 4.1. Thin dot-dashed green and dashed magenta lines represent the LT and ET MSR from Lange et al. (2015). Top and right panels show density histograms of stellar mass and size, respectively. Parameters of fitted power–law are given in the bottom of Table 4.1. Circles in blue shows the Hα sample studied in Chapter 6.

the largest difference in the cosmic volume at higher redshifts, $1 \leq z < 2$ (0.73 and 0.56, in Mowla et al. and in this work, respectively). This difference mainly obeys to the fact that the galaxies studied in Mowla et al. (2019) are more massive $\log M_*/M_\odot > 11.3$, complemented with galaxies from van der Wel et al. (2014, 3D-HST+CANDELS). Precisely, this addendum contains a great part of the ET galaxies of the resulting sample in the last redshift bin studied in their work. Since both works, van der Wel et al. (2014), and Mowla et al. (2019) are consistent, we decided to keep only the fits from the latter one.

It is worthy of note that due to the limited OTELO's field of view ($\sim$56 arcmin^2), the comoving volume surveyed is relatively small if compared with broadly known extragalactic surveys (e.g. SDSS, COSMOS, CANDELS). This fact may introduce a bias toward detection of sources with lower masses losing the high-mass end. For instance, if the results of the zCOSMOS survey are

Table 4.1. Results of the power–law fitting of MSR.

samples	$< z >$	log a	b	n	log $M_*/M_\odot$ range
ET vol1	0.33	-3.41 ± 0.63	0.37 ± 0.07	37	6.03 – 10.80
ET vol2	0.77	-3.53 ± 0.56	0.38 ± 0.06	68	8.48 – 11.12
ET vol3	1.11	-5.42 ± 3.31	0.56 ± 0.32	17	9.97 – 10.92
LT vol1	0.34	-1.87 ± 0.13	0.24 ± 0.02	749	5.42 – 10.78
LT vol2	0.79	-1.21 ± 0.13	0.18 ± 0.01	964	7.40 – 11.91
LT vol3	1.39	-1.41 ± 0.18	0.20 ± 0.02	1160	7.77 – 11.06
ET all	0.66	-3.44 ± 0.32	0.38 ± 0.03	122	6.03 – 11.12
LT all	0.88	-1.74 ± 0.06	0.23 ± 0.01	2873	5.42 – 11.91

Redshift bins are defined as follows: vol1: $z < 0.5$, vol2: $0.5 \leq z < 1$, and vol3: $1 \leq z < 2$. Median redshift for each volume and type is given in column 2. For each bin we fit a single power–law according to Eq. 4.1, with the number of galaxies and stellar-mass range indicated in the last two columns. These are showed in Figure 4.13. The last two rows give the results of fit using all the sources in ET and LT samples – both are shown in Figure 4.14.

scaled to the sky area explored by OTELO, and using the same selection criteria given by López-Sanjuan et al. (2012, i.e. $0.1 < z < 1.1$, log $M_*/M_\odot > 11$, and OTELO$_{deep}$< 24), we should find about 11 sources in the census of the OTELO survey. However, after the selection process described in Sect. 4.2, we are left with only 4 sources. Hence, it is necessary to stress that we loose $\sim 60\,\%$ of the high-mass end by effect of the limited sky covering of our survey.

In Figure 4.14 we show ET and LT galaxies analysed in this work without separation onto redshift bins. In this Figure we show the power–law fits to the whole ET and LT samples (tabulated in the bottom part of Table 4.1), as well as results from Lange et al. (2015, their Table 2 and 3, i-band fits), where local galaxy sample was studied ($0.01 < z < 0.1$, log $M_*/M_\odot \sim 7.5 - 11$). The MSR for ET and LT populations of OTELO are consistent with the low-redshift relation.

In order to test the effects of the selected stellar-mass range when compare our results with previous studies, we limited our sample to the lower limits given in Shen et al. (2003). These limits in log $M_*/M_\odot$ are 10.1 and 8.8 for ET and LT galaxies, respectively. Both limits correspond to median mass values of ET and LT samples studied in this work (i.e., removing a considerable part of our sample). Even so, using these mass-limited samples we found good agreement between our fit, and the results from Shen et al. (2003). For the sake of clarity,

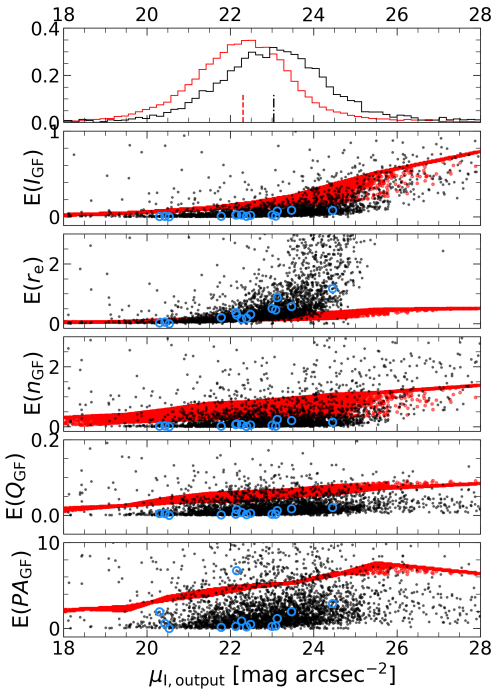

Figure 4.15. Errors of given parameter as a function of surface brightness μ_{output}. Black dots show the outcome from this work, and the red dots show data for selected (f1=1) galaxies from Häussler et al. (2007). Top panels show density distribution of μ_{output}. The median values are marked with a red dashed-line (22.3) and a black dot-dashed line (23.04). Circles in blue show the Hα sample studied in Chapter 6.

we do not include these results in Figure 4.14. On the top panel of the same Figure we show distribution of stellar-masses for ET and LT galaxies. It is noticeable that both populations dominate in different mass regimes with median values of $\log M_*/M_\odot \sim$ 8.8 and 10.12 for LT and ET galaxies, respectively. On the other hand, as can be seen on the right panel of Figure 4.14, both galaxy populations occupy the similar range of physical sizes. In Section 4.5 we will present more detailed discussion on possible median size evolution in the r_e–z space.

4.3.2 Error estimations

As described in Peng et al. (2010) the formal uncertainties derived in `GALFIT-M` are only the lower estimates. After extensive simulations and tests of this software, Häussler et al. (2007) provides estimates of uncertainties based on the comparison of input and output values. In Figure 4.15 we show the errors from

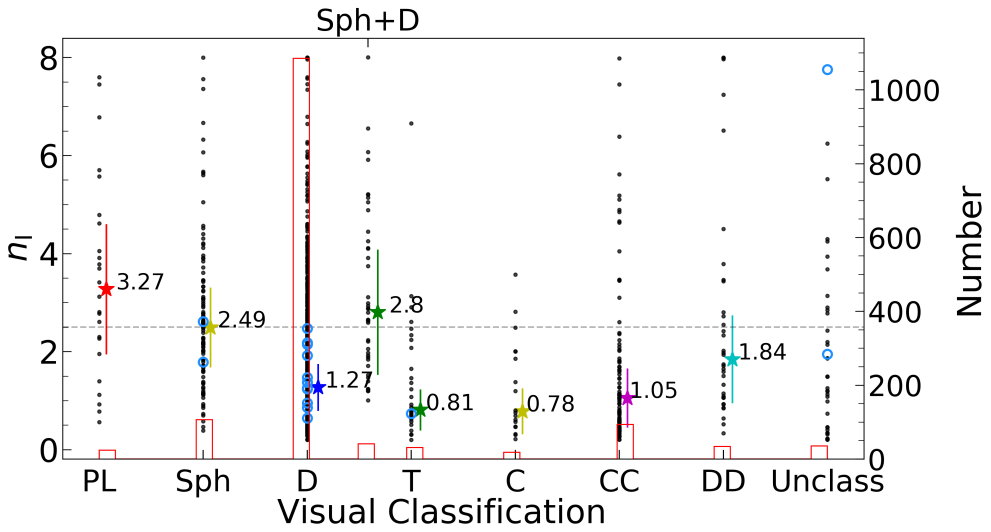

Figure 4.16. Comparison of visual classification and Sérsic index. Black dots show objects with both, visual classification and parametric parameters. The horizontal axis represents visual types, while the vertical axis shows their Sérsic index in *HST* I-band n_I. Blue histogram shows the number of sources of a particular type (right-hand *y-axis*). Star-shape marks show median values of Sérsic index for each visual classification, and error bars represent median absolute deviations. Blue circles represent the Hα sample studied in Chapter 6.

Häussler et al. (2007) and the nominal errors from `GALFIT-M` from this study, as a function of the surface brightness defined as (Häussler et al. 2007)

$$\mu_{\rm output} = mag + 2.5 \cdot \log[2(b/a)\pi r_{\rm e}^2], \tag{4.2}$$

where mag is the I-band magnitude, b/a the axis ratio, and $r_{\rm e}$ the half-light radius in arcseconds. The $\mu_{\rm output}$ is calculated using the output `GALFIT-M` parameters. Even though the nominal error values are the lower estimates, it is clear that these behave as expected – the errors increase with surface brightness for all parameters (even if not so evident for n, Q and PA). This fact could also be appreciated if the errors are represented as a function of $I_{\rm input}$ (however, we do not show this relation here). We report the nominal values of the errors with the indication that these are lower-bound estimates (at least for bright objects) since the total error budget would require performing simulations as in Häussler et al. (2007), which is beyond the scope of this work.

4.4 Visual classification

A visual classification of the OTELO galaxies is presented in this section. We performed a visual classification of selected sources (Sec. 4.2) down to $\mathrm{OTELO}_{deep} =$ 24.5 mag using MorphGUI interface described in Section 3.2. Even if more sources were classified in this way, the results for a total of 1467 sources are presented in this section in order to be able to compare the visual classification with meaningful morphological parameters obtained for *morphological sample*. We considered following morphological types: point-like/compact (PL), spheroid (Sph), disk (D), tadpole (T), chain (C), clumpy cluster (CC), doubles (DD), and unclassified (Unclass). We permitted to classify sources with mixed classes of spheroid with disk (Sph+D) in order to record disks with visible bulges.

These results have to be taken as preliminary because only one person (J.N.) visually classified these sources. In order to provide robust (i.e., to corroborate) classification, a common practice is to provide at least three independent classifications per object.

Taking into account that no statistics can be provided to estimate the goodness of the classification per individual, we can not show any robust results. We show, however, the dependence of the visual classification with I-band Sérsic index in Figure 4.16. From this Figure we can clearly appreciate that PLs, Sphs and Sph+Ds, have significantly higher median Sérsic index (3.37, 2.49, and 2.8, respectively) than the sources in the remaining classes. This is an expected behaviour since early-type galaxies (PL, Sph, and galaxies with bulges) are described with profiles with higher Sérsic index n. We can also notice, that a majority of Hα sample is classified as disk galaxies.

4.5 Discussion

Strateva et al. (2001) demonstrated that a $(u - r)$=2.22 colour cut separation can be useful for a broad segregation of ET from LT. They used a sample with more than 140 000 galaxies from the SDSS survey down to magnitude $g = 21$ and $z < 0.4$. Even if this particular method does not directly use the parameters derived in this work, it is interesting to test its performance using the OTELO catalogue. This method employs relatively easy-to-obtain parameters, namely observed magnitudes in g, r and u bands, which are available also in the OTELO catalogue. Figure 4.17 shows how this method is able to separate sources in the *morphological sample* up to $z_{\mathrm{phot}} =$ 2. Nearly 81% (97%) of ET (LT) from the *morphological sample* are correctly separated, i.e. with

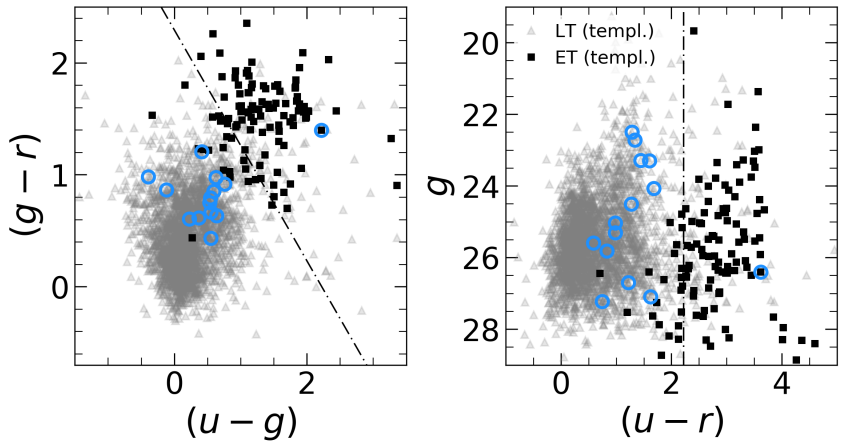

Figure 4.17. ET/LT-colour separation from Strateva et al. (2001) using data from this work. Gray triangles and black squares represents LT and ET galaxies classified via best-fitting galaxy templates. Dot-dashed line represent $(u-r) = 2.22$. Blue circles represent the Hα sample studied in Chapter 6.

$(u - r) \geq 2.22$ (< 2.22). The reliability of ET (LT) selection for this method (defined as in Strateva et al. 2001) is about 54% (99%). As comparing with values from Strateva et al. (2001), their ET (LT) completeness and reliability are 98% (72%) and 83% (96%) for spectroscopic sample and 80% (66%) and 62% (83%) for visually classified galaxies, respectively (see their Table 2 and 3). Although the completeness of our ET selection using this method slightly decreases, our sample extend to much higher redshift and deeper in magnitude than both samples presented in Strateva et al. (2001). In spite of this, an more appropriate $(u - r)$ colour cut separation could be used as a fair proxy to a ET/LT segregation in OTELO data.

The stellar mass–size relations for ET and LT (Figure 4.14) in our sample, regardless of the separation in redshift bins, are in agreement with the general trends at low redshift reported in the recent literature (Shen et al. 2003; Lange et al. 2015). According to these authors, and leaving aside the data scattering, the MSR for ET galaxies is steeper than the corresponding to LT, as confirmed in this work. Furthermore, the stellar-mass distributions shows a sort of bi-modality, with LT galaxies being less massive than ET sources (in our case, with median values of $\log M_*/M_\odot = 8.8$ and 10.12, respectively).

According to the results given in Section 4.3 we can not conclude nothing about the possible evolution of the MSR in both types considering stellar-mass range studied (Fig. 4.14). Recent studies of the MSR in similar redshift range as studied in this work (e.g., van der Wel et al. 2014; Roy et al. 2018; Mowla et al.

2019, and references therein) point out to a median galaxies size evolution with redshift (r_e–z). In particular, Mowla et al. (2019) used I-band *HST*-ACS images to quantify the r_e–z relation for COSMOS-DASH survey, i.e., the same instrument and filter of *HST* as in this work. The use of the same photometric band is especially important because of the claimed dependence of size on the wavelength at which the measurements are done (e.g., Kelvin et al. 2012). Since the MSR presented by Mowla et al. (2019) do not match stellar-mass ranges studied here, we compare the r_e–z for three fixed mass of $\log M_*/M_\odot = 10, 10.5,$ and, 11, furthermore including lower-mass bins of $\log M_*/M_\odot =$ 8, and 9 for the LT galaxies from this work. In Figure 4.18 we show the results of this comparison. In this figure we only have plotted median size values for bins where we have more than 3 objects (note that for the ET most massive stellar-mass bin we plot only intermediate redshift bin). This ensure a more robust comparison with previous works.

Considering, the r_e–z relation for fixed stellar-mass of $\log M_*/M_\odot = 10.5$ (red lines and points in Fig. 4.18) for which OTELO have sufficient statistics in both morphological types, we can notice that our results are consistent with Mowla et al. (2019): ET galaxies present steeper median size evolution, as compared to LT population. In addition, we show the median size evolution for LT galaxies in a mass regime previously unexplored, namely for $\log M_*/M_\odot$ of 8, and 9. These are two mass bins where OTELO has a sufficient number of sources in all redshifts (between $\sim$ 50, and $\sim$ 450). We find a very mild evolution of the median size for these masses, what is compatible with a passive evolution of this type of galaxies (e.g., van der Wel et al. 2014; Mowla et al. 2019). Generally speaking, and taking into account the biases introduced in our selection process (under-representation of high-mass end), our results are in agreement with previous findings on MSR, as well as on the median size evolution r_e–z.

About the preliminary visual classification, we have found a correlation of the median Sérsic index n with the visual classes. This correlation is expected due to the profile of the light distribution for each class described in terms of n.

Along this Chapter we have shown that the Hα sample is composed mostly of blue, disk, low-Sérsic index galaxies. The overall result for this sample is consistent with the fact that these are SFG. In Chapter 6 we present a more detailed discussion of this sample in the context of mass-metallicity relation.

Finally, in Chapter 5 we will study a sample of ET-ELG. We make a use of the morphological analysis presented in this Chapter for the ET segregation. Details on the further selection of ET-ELG sample are given in the following Chapter.

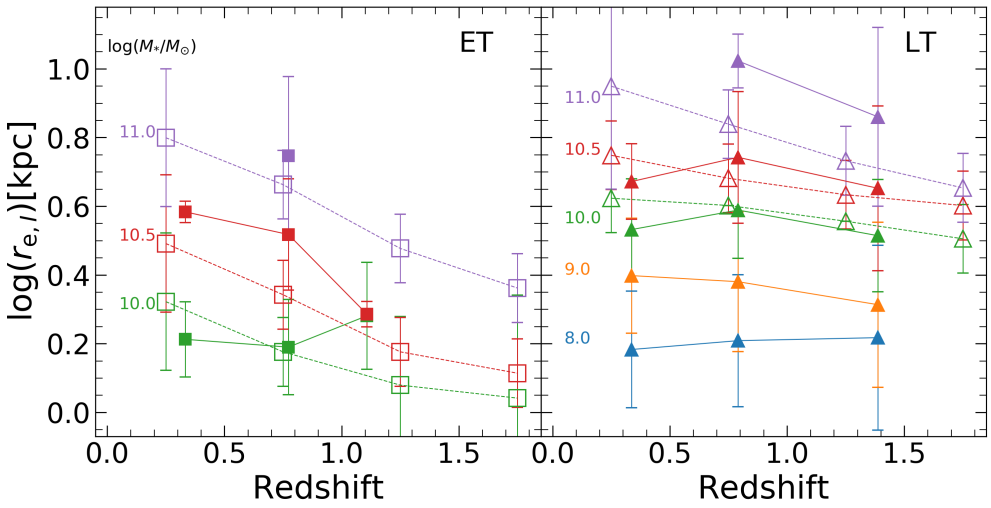

Figure 4.18. Median size evolution with redshift, the r_e–z relation. Median sizes are shown for fixed stellar-mass bins centered at $\log M_*/M_\odot = 8, 9, 10, 10.5,$ and 11, with colours indicated in the right side of the plots (bin width of 0.5 dex.). Note that only three most massive bins are showed for ET for each volume (left panel). Filled symbols represent data from this work, while open markers shows data from Mowla et al. (2019), given in their Table 3 (including errors). Our error bars represent the median absolute deviation of the data in each bin. We only plot the median sizes for bins which have more than 3 sources.

5

Early-type emission line galaxies

The origin of the gas, dust, and source of ionization in early-type emission line galaxies (ET-ELG) are still a matter of controversy. The literature about the observed properties of these sources is based on low-redshift data. Hence, scarce or null information about ET-ELG at intermediate redshifts makes these questions even more puzzling. Taking advantage of the OTELO survey capabilities we recover a population of ET-ELG at intermediate redshift, providing insights on the population densities of these intriguing objects.

5.1 Introduction

Since the first investigations about the chemical and kinematic properties of early-type galaxies (ET, Mayall 1939; Humason et al. 1956; Phillips et al. 1986) the view of these as devoid of gas, dust, and with no star formation has changed gradually. The ETs frequently exhibit emission lines in their optical spectra ($\sim$ 50 - 75%, depending on the selection process, Sarzi et al. 2006; Capetti & Baldi 2011). Multi-wavelength observations, from X-ray, through optical to far-infrared (FIR) and radio, have shown a multi-phase nature of interstellar matter (ISM) with hot, warm, and cold components (Jura et al. 1987; Lees et al. 1991; Trinchieri & di Serego Alighieri 1991; Goudfrooij et al. 1994). A correlation between FIR and radio emission and recent rejuvenation episodes have also been found (Walsh et al. 1989; Annibali et al. 2007).

Some authors have found signs of low-ionization nuclear emission-line regions (LINERs, e.g. Annibali et al. 2010; Capetti & Baldi 2011; Gomes et al. 2016) in

early-type emission line galaxies (ET-ELG) at low redshift. Recent simulations indicate that these regions are not limited to the nuclear region, but that they are spatially extended (e.g, Byler et al. 2019, low-ionization emission-line regions or LIERs).

The evidence for the ubiquitous presence of gas and dust in ETs is now unquestioned. However, different morphologies and kinematic properties of both expose controversies about (i) the origin of the gas and dust, and (ii) the source of ionizing photons. Many studies lead to opposite findings on both issues. For instance, van Gorkom et al. (1989) concluded that the ISM of ETs has external origin (merger process or inflow of the intergalactic matter), while Knapp et al. (1992) suggested that the stellar mass loss plays a key role in supplying material to the ISM. As for the origin of the ionizing photons, several different sources have been proposed: hot low-mass evolved stars, post-AGB, or young stars (Trinchieri & di Serego Alighieri 1991; Athey & Bregman 2009; Pandya et al. 2017; Herpich et al. 2018; Byler et al. 2019), and nuclear activity or shocks (Panuzzo et al. 2011). Their true origin, however, is still a matter of debate (Annibali et al. 2010; Capetti & Baldi 2011). For a general review see Goudfrooij (1999) and Renzini (2006). Finally, according to our knowledge, no census of ET-ELG at intermediate redshifts is available in the literature.

In this work we report an unprecedented discovery of 14 ET-ELG at seven different redshift windows ($0.4 < z < 1.1$). These windows corresponds to seven different emission lines as seen by the OTELO survey (i.e.: Hα, [O I], He I, [N I], [O III], Hβ, and Hγ). Considering strong emission lines, i.e., Hα, [O III], and Hβ, at $z \sim 0.4, 0.8$ and 0.9, respectively, OTELO detects 9, 2.6, and 3.6 times higher number density of ET-ELG than would be expected from local SDSS data. Our findings hold even regarding the uncertainties associated to the cosmic variance. Furthermore, volume limited samples of Hα, [O III], and Hβ were selected from local SDSS data to account for the effects of a possible luminosity evolution, which could affect the count number.

5.2 ET-ELG sample selection

Our sample of ET-ELG is selected from the OTELO catalogue with morphological information described in Chapter 4. Following the same criteria as presented in Section 4.2, we select sources with meaningful morphological parameters up to $z_{\rm best} = 2$, resulting in 2995 sources (*morphological sample*). From those candidates we selected the sources of interest according the following criteria (we indicate in parentheses the symbols used in Fig. 5.1):

1. Galaxies with the best fit galaxy template $\rm SED_{best}$ corresponding to an

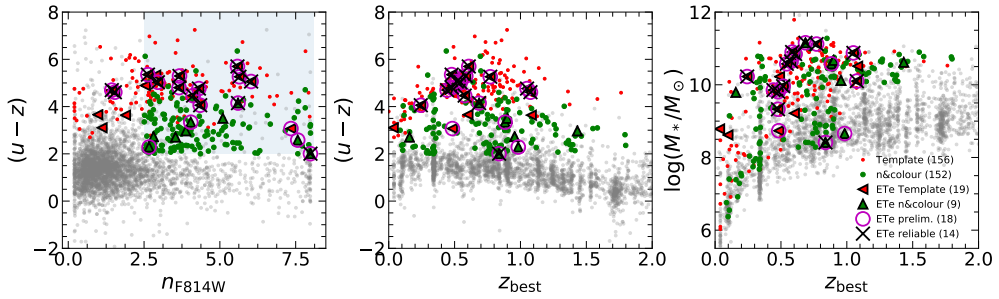

Figure 5.1. *Left panel:* Observed $(u - z)$ colour as a function of Sérsic index n_I. The shaded region indicates $n_I > 2.5$ and $(u - z) > 2$ (see Sec. 5.2). *Middle panel:* Observed $(u - z)$ colour as a function of photometric redshift $z_{\rm best}$. *Right panel*: Stellar mass $\log M_*/M_\odot$ as a function of $z_{\rm best}$. Dots represent the overall OTELO sample; the early-type template-, Sérsic-, and colour-selected samples are represented in gray, red, and green, respectively. Green triangles and left pointing red triangles show ET-ELG samples selected by their Sérsic & colour values, and template, respectively. Empty circles in magenta show the visually selected ET-ELG sample, while black crosses show the robust ET-ELG sources as described Sec. 5.2. The numbers in the legend represents the number of sources in each particular sample.

E/S0 type (red dots),

2. galaxies with Sérsic index $n_I > 2.5$, and $(u - z) > 2$, and not selected in the previous point (green dots),

3. galaxies with at least one detected emission line in PS using a semi-automatic procedure (for details see Bongiovanni et al. 2019; red and green triangles).

In this way, we obtained a list of 28 objects as raw candidates for ET-ELG. From this list we removed 10 sources which clearly show characteristics that point to a different type of object (a possible star, bulge dominated spiral, etc.) after a visual inspection of the *HST*-ACS images. The remaining 18 sources have been inspected individually using our online GUI by five members of our team, assigning a chemical spice to the emission feature observed in the PS and its associated redshift $z_{\rm PS}$ (see Figs. 5.7-5.9 for an example of the relevant information used in the inspection using our GUI). Every member assigns a personal vote of confidence to each source and we select as reliable ET-ELG the sources with three or more votes. It results in a final sample of 14 reliable sources. In Figure 5.2 we present $z_{\rm PS}$ as a function of $z_{\rm best}$ (top panel), and *EW* (bottom panel). As can be seen on the top panel, the assigned $z_{\rm PS}$ to the emission line feature lies within the estimated error of the corresponding photometric redshift in each case (see Sect. 2.1.4).

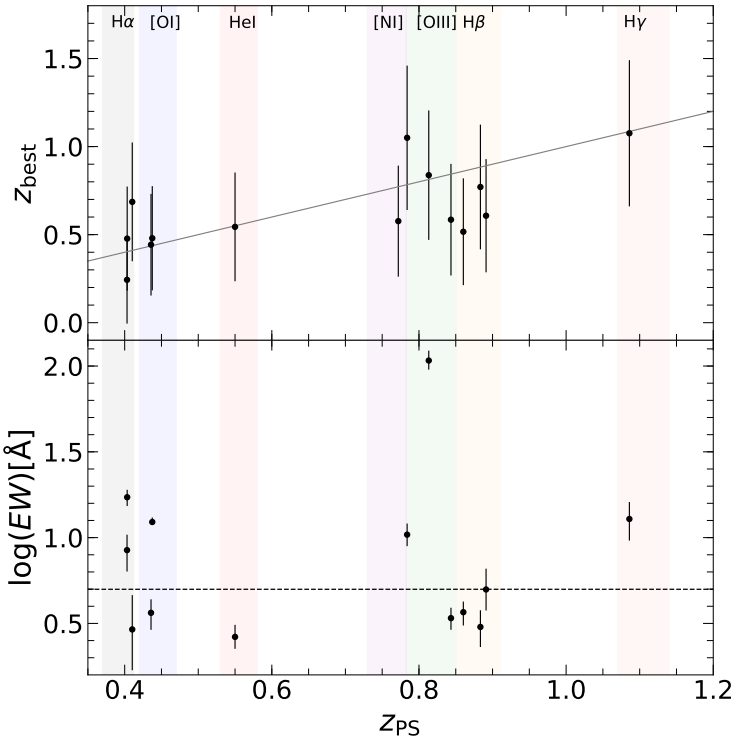

Figure 5.2. Assigned redshift $z_{\rm PS}$ vs. $z_{\rm best}$ and $\log(EW)$ for the ET-ELG preliminary sample. Reliable ET-ELG sources are shown as blue empty circles. Error bars on $z_{\rm best}$ represent the maximum redshift errors estimated in Bongiovanni et al. (2019), while $z_{\rm PS}$ are of the order of $\pm 10^{-3}$. The line in gray on the top panel represents the 1:1 relation. Errors in EW are estimated from simulation's probability density function for the 68% confidence intervals. For details on the errors estimation for $z_{\rm PS}$ and EW, see Nadolny et al. (2020). Specific ELs, as seen by the OTELO survey, are indicated as shaded vertical regions. Horizontal black dashed-line marks the $EW = 5$ Å limit (see Sec. 5.2).

We obtained the line fluxes and EWs for 13 (out of 14) sources in our sample using the method of inverse deconvolution described in Section 3.4. The EW distribution against redshift is shown in the bottom panel of Figure 5.2. We note that one source (`id:1579`) is missing in this panel due to lack of measurements of EW because the inverse deconvolution process did not converge. This source, is a [N I] emitter with confirmed spectroscopic redshift from DEEP2 survey (Newman et al. 2013). A total of seven sources from our ET-ELG sample have EWs lower than 5 Å. According to the design of the OTELO survey, the detection probability of sources with $EW < 5$ Å drops below 50%, as estimated in Ramón-Pérez et al. (2018). In summary, we have a sample of 14 robust ET-ELG. Since we do not apply a completeness correction, the number densities

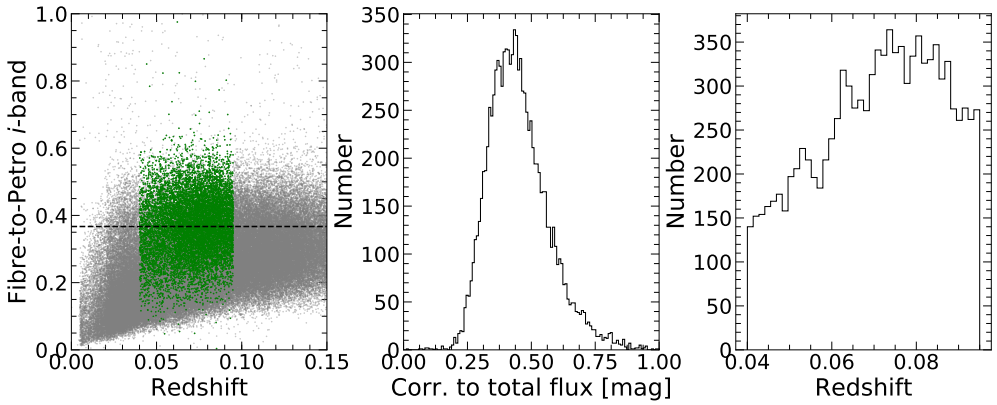

Figure 5.3. *Left panel:* Fibre-to-total (Petrosian flux as a proxy to total) flux ratio in i-band of the overall SDSS sample (gray dots) and selected ET-ELG (green dots). Horizontal dashed line in black represents the median value of the fibre-to-total flux ratio. *Middle panel:* Correction of the fibre-to-total magnitude estimated from the fibre-to-total flux ratio. *Right panel:* redshift distribution of the selected ET-ELG from SDSS sample.

of ET-ELG are lower-limit estimations. The resulting percentages of Hα, [O I], He I, [N I], [O III], Hβ, and Hγ ET-ELG over the overall ET sample are 37.5%, 22%, 14%, 5%, 12.5%, 12% and 8%, respectively.

5.2.1 SDSS ET-ELG sample

In order to compare our results with the Local Universe we use available data from the SDSS DR8, in particular the *MPA-JHU* catalogues, as described in Section 2.2.3. We select sources with reliable spectroscopy and no warnings on the redshift measurements and target type to be galaxy, as described in Brinchmann et al. (2004, `RELIABLE = 1, Z_WARNING = 0, TARGETTYPE & SPECTROTYPE = GALAXY`). From these, following Herpich et al. (2018), we select sources with spectroscopic redshift in the range $0.04 < z_{\rm spec} < 0.095$, and EWs > 0.5 Å for Hα and [O III]λ5007 lines, resulting in a total of 122 419 sources. We match the objects with the morphological catalogue of Domínguez Sánchez et al. (2018).

We further select sources classified morphologically as ETs (`TT_pred` $<$ `0`) and with a probability lower than 20% to have a disk/features (`P_disk` $<$ `0.2`). Selecting all the ETs in the given redshift range (with or without emission) we get 67 879 sources; and including the emission line criteria, this sample is reduced to 10 523 sources. This assure a fairly complete local sample up to the upper redshift limit (90% completeness of the parent morphological sample, see: Meert et al. 2014; Domínguez Sánchez et al. 2018). The fibre-to-total (using

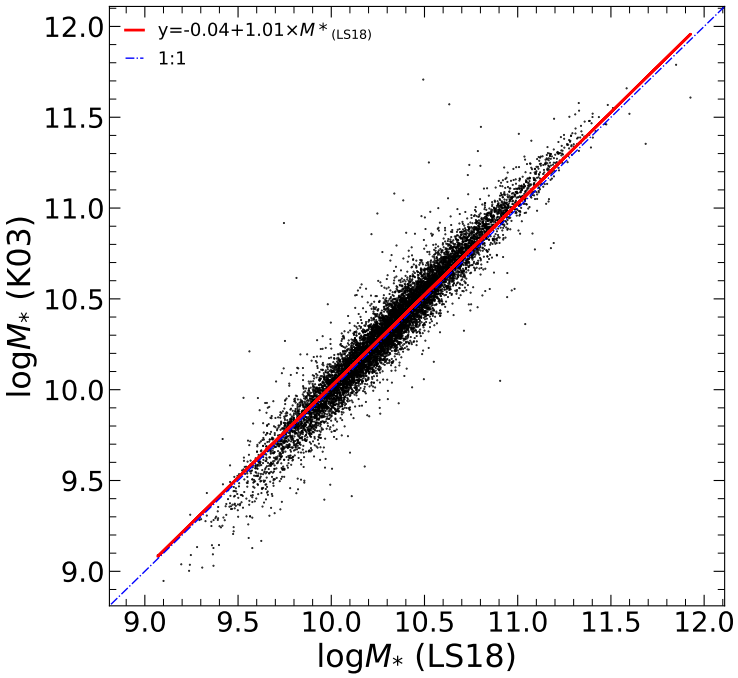

Figure 5.4. Comparison of the methods used in the stellar masses estimation for the selected ET-ELG from SDSS: López-Sanjuan et al. (2018, LS18, used in this work) vs. Kauffmann et al. (2003b, K03). Red line represents best linear fit, while blue dot-dashed line represents a 1:1 relation.

Petrosian photometry as a proxy to total) i-band flux and the estimated aperture correction is showed in the left panel of Figure 5.3. The mean value of fiber-to-total ratio found for the SDSS sample is of 0.36, which is slightly higher than the reported by Brinchmann et al. (2004). However, this is expected for the ET since these sources are more compact, thus filling the 3″ fiber more effectively (more of the total flux goes into the fiber). We use the fiber-to-total ratio to provide the aperture correction in the absolute magnitude calculation in order to estimate stellar masses (see below). We further divide the SDSS sample on three sub-samples using the BPT-NII diagram (Baldwin et al. 1981) classification from Brinchmann et al. (2004), obtaining 48.3% SF (including "low-S/N" SF, see Brinchmann et al. 2004), 27.1% of composite, and 24.3% AGN+LINERs galaxies, while the remaining 0.3% are unclassified. This results in a total of 10 491 ($\sim$ 15% of all ETs) sources selected as our local sample of ET-ELG, hereafter the SDSS sample. The percentages of ET-ELG with detected [O I], He I, Hβ, and Hγ lines in SDSS sample are 99%, 78%, 65%, and 72%,

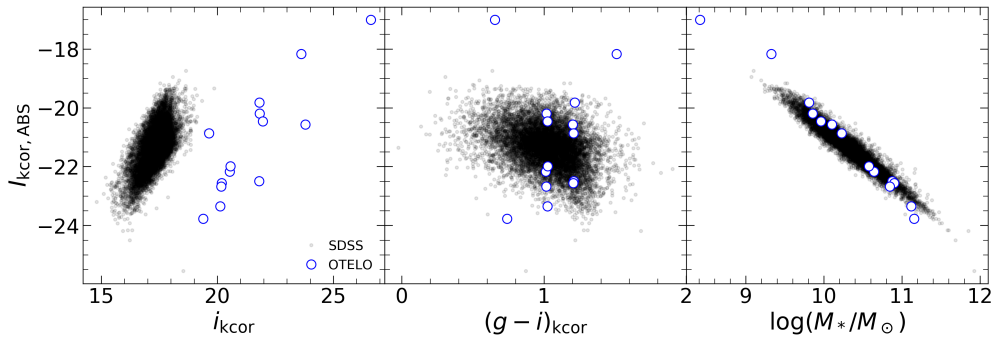

Figure 5.5. Comparison of selected parameters for SDSS and OTELO ET-ELG samples. From left to right: i-band rest-frame magnitude, $(g-i)$ rest-frame colour, and $\log M_*/M_\odot$ as a function of i-band absolute magnitude.

respectively[1].

5.2.2 Stellar masses

We used stellar masses calculated as described in Section 3.3 using rest-frame g and i bands magnitudes adopting the prescription from López-Sanjuan et al. (2018). Stellar masses of the OTELO's selected ET-ELG together with the overall OTELO sources are shown in the right panel in Figure 5.1. For consistency, we estimate M_* for the SDSS sample using the same method after a fiber-to-total flux correction. A comparison between our M_* estimation with those of Kauffmann et al. (2003b) show a good agreement ($\sigma = 0.09$ dex; Figure 5.4). We will use our M_* estimation for the SDSS sample for internal consistency.

5.3 Analysis

For the majority (85%) of the OTELO's ET-ELG, the basic properties used in this work (i.e i-band absolute magnitude, rest-frame colour, and stellar mass) are in the range of the values observed in the SDSS sample. Only two sources from our sample (a Hα and a [O II] emitters) have stellar masses lower than the ET-ELG that come from selected SDSS sample (see Figure 5.5)

In this Section we will analyze (indirectly) the properties of our sample in the context of the BPT diagram. Furthermore, we estimate the cosmic variance (CV) for the OTELO survey per cosmic volume surveyed. The number density

[1]Since the selection is based on the Hα and [O III] emission lines, thus all selected ET-ELG have these lines

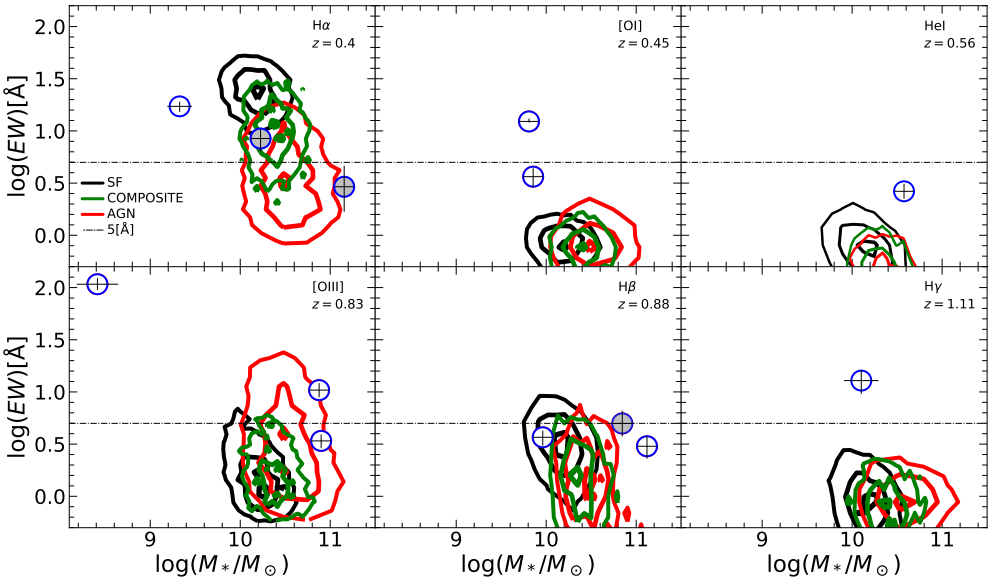

Figure 5.6. *EW* vs. stellar mass. Each panel represents the data for the particular emission line indicated in the top right corner of the panel, and the corresponding median redshift in the case of OTELO data. Colored contours correspond to SF (black), composite (green), and AGN+LINERs (red) regions for each particular emission line obtained from the SDSS sample and according the BPT digram (Brinchmann et al. 2004). Each contour encloses (outside-in) 85%, 50% and 5% of the particular sample. Circles in blue show reliable OTELO ET-ELG for every particular EL. Filled gray symbols indicate truncated PS (i.e. sources with lower-limit *EW* measurements). The number of OTELO and SDSS sources included in each panel are given in Table 5.1, cols. 2 and 10, respectively. Note that the [N I] panel is not shown because there are not data from SDSS and PS inverse deconvolution did not converge in case of our ET-ELG (`id:1579`). The horizontal line at 5 Å in each panel shows the limit where the detection probability of the OTELO survey drops below 50% (see Sect.5.2).

is studied including the CV uncertainties. We also include an examination of the volume-limited samples in order to assure robustness of our findings in case of a possible luminosity evolution.

5.3.1 Star-forming, composite and AGN+LINER galaxies

Figure 5.6 shows the stellar mass M_* and *EW* for OTELO and SDSS ET-ELG samples for different ELs (as listed in Table 5.1), and in the case of our sample, different redshift ranges (both indicated in the top right corner of each panel). We divide the SDSS sample according to the BPT classification (SF, composite, and AGN+LINERs), as explained in Sec. 5.2.1. Because of the limited spectral

range of the OTELO PS, we would only distinguish between SF, composite or AGN+LINERs for the case of three Hα emitters using the N2 index (Stasińska et al. 2006). However, two Hα sources (`id:6176, 6736`) have truncated PS on the red side (i.e. there are no measurements of [N II]λ6583), and only one source (`id:754`), studied in Chapter 6 (and in Nadolny et al. 2020), is classified as SF galaxy through the N2 index. Additionally, no match was found between our sample and the census of AGN in the OTELO survey described in Ramón-Pérez et al. (2019). In order to fully explore all the possibilities, we also employ the diagnostic diagram from Stern et al. (2005), revised by Donley et al. (2012) using MIR photometry. For 78% (14 out of 18) sources in our sample we have measurements in 4 *Spitzer*/IRAC bands (3.6, 4.5, 5.8, and 8.0 μm). We find no AGN in our sample using this method.

Finally, the only indirect indication that a source in our sample is SF, composite, or AGN+LINERs type is the position on the M_* vs. EW plane with respect to the SDSS sample (see contours in Fig. 5.6), assuming null or small evolution. The majority of sources with Hα, [O III] and Hβ lines from our sample fall into the imprint of the SDSS sample. One clear outlier is found in the [O III] sub-sample with low mass and high EW. In the case of [O I], and Hγ, the sources are clearly above SDSS distribution. In the case of [N I], the inverse deconvolution did not succeed to converge. Moreover, no measurements are given in the SDSS catalogue for this particular EL. We made a similar analysis using WHAN (Cid Fernandes et al. 2011) diagram to divide SDSS sample into SF, AGN and LINER sub-samples. We obtained similar results as presented in this section and Figure 5.6.

5.3.2 Cosmic variance

It has been demonstrated that cosmic variance (CV) is an important factor of uncertainty (e.g., Driver & Robotham 2010) in the determination of the number densities of a given galaxy population. It arises from the underlying large-scale density fluctuations of the cosmic web. The CV can vary significantly depending on the survey design. Basic parameters responsible for changes in CV are the survey area, redshift, and stellar mass ranges explored. The variation of CV goes from $\sim$ 10%, for wide area surveys like SDSS, up to 50% and even 70% for pencil beam surveys like Ultra Deep Field (Beckwith et al. 2006), as estimated in Driver & Robotham (2010). Since the OTELO survey covers a relatively small sky area, we estimate the CV for the seven cosmic volumes where our ET-ELG are found.

To test the impact of CV on our number density we use the method described in Moster et al. (2011), and obtain a fractional uncertainty due to CV ($\sigma_{\rm CV}$)

for each volume defined by the emission line under consideration. The highest $\sigma_{\rm CV}$ is measured for the Hα emitters (42%), and drops as the cosmic volume (redshift) increases, as expected. We quote $\sigma_{\rm CV}$ for all volumes (or EL) in Table 5.1, column 5.

5.3.3 Number density ℵ

The number density ℵ in this work is defined as the number of galaxies per comoving Mpc^3 estimated from the observed number of galaxies in a given cosmic volume. Due to the narrow spectral range covered by the OTELO survey (230 Å width, centered at 9175 Å), OTELO sees different emission lines at different redshifts thanks to the PS (see the PS of all the sources in top left panels of the informative cards showed in Figs. 5.7 – 5.9), resulting in different cosmic volumes per emission line. In what follows, we compare OTELO's number density per emission line ($\aleph_{\rm OTELO}$) to the SDSS number density of the sub-sample of SDSS ET-ELG with a particular emission line ($\aleph^{EL}_{\rm SDSS}$, where EL stands for emission line).

The results of the number density analysis are given in Table 5.1. Note that, because the selection of SDSS sample is based on Hα and [O III] lines, the number densities (thus source number) $\aleph^{EL}_{\rm SDSS}$ for both lines are the same. We found that even with the low number of galaxies in our sample, the OTELO survey, with less than 0.02 deg^2, sees more ET-ELG per volume than SDSS, one of the largest surveys in total area, with more than 8 000 deg^2. We see the largest difference ($\aleph_{\rm OTELO}/\aleph^{EL}_{\rm SDSS}$) between OTELO and SDSS number densities for the Hα emitters, for which OTELO sees 9 times more objects. For the cosmic volume associated to this EL we also find the largest uncertainty due to the cosmic variance $\sigma_{\rm CV}$. Even considering this uncertainty for both surveys we still find a substantial difference of number densities of 4.8. The same is true for other strong emission lines, for instance [O III] and Hβ, for which OTELO detects 2.6 and 3.6 times more than SDSS. Again, considering $\sigma_{\rm CV}$, we still detect more sources than SDSS (1.7 and 2.4 times more for [O III] and Hβ emitters, respectively). It is necessary to note that the count number estimations for OTELO ET-ELG are not corrected for completeness, and that OTELO detects less than 50% of sources with $EW < 5$Å (see Sec. 5.2). Thus $\aleph_{\rm OTELO}$ should be considered as a lower limit, i.e. the difference between OTELO and SDSS could be significantly larger.

Volume limited SDSS sample

To further investigate the robustness of our findings, we test possible luminosity evolution effects on the number densities. Because of the low number of sources in our sample in each cosmic volume, we chose to use the data from our previous works on the OTELO emitters. Thus, we studied volume limited samples for Hα, [O III], and Hβ lines. Volume limited luminosities for these lines are computed using fluxes taken from Nadolny et al. (2020), Bongiovanni et al. (2020) and Navarro Martínez et al. (2021, in prep.), respectively. The sources in these works are not necessarily early-type galaxies, thus, we consider this exercises as merely informative.

Due to the luminosity distance relation, in terms of luminosity SDSS observes slightly less luminous objects. Thus, using the volume limited luminosities estimated from OTELO emitters, we define the SDSS volume limited samples for Hα, [O III], and Hβ lines. We find that the number of sources in the Hα volume limited from SDSS does not change, while for [O III] and Hβ it drops by about 9% for both ELs. The resulting ratio of OTELO to SDSS volume limited number densities $\aleph_{\rm OTELO}/\aleph^{EL}_{\rm SDSS}$ (for [O III] and Hβ lines) increases as expected due to the lower number of sources in the SDSS volume limited samples. This increase is proportional to the change in the number of sources in volume limited samples. The biggest difference is found for the Hβ emission line. The ratio $\aleph_{\rm OTELO}/\aleph^{EL}_{\rm SDSS}$ increases from 3.6 to 3.9 for this EL. This further confirms our finding, even under the effects of a possible luminosity evolution. Note, however, that possible errors due to the CV (of 29% in the case of Hβ) would easily dilute these effects.

5.4 Results

We analyzed the sample of 14 ET-ELG from the OTELO survey in seven cosmic volumes defined by the emission line observed from $z\sim0.4$ to ~1.1. The stellar mass M_*, line EW, absolute magnitude, and rest-frame colours of these sources are in general agreement with the same characteristic parameters of a local SDSS sample ($0.04 < z < 0.095$; +10k sources) of ET-ELG. However, the OTELO survey reaches a lower line flux limit, which is about one order of magnitude lower than the same limit of the SDSS sample, for the [O III] emission line.

Hence, OTELO detects at intermediate redshifts a number density of ET-ELG between 2 and 9 times higher than the observed in the local universe. In particular, OTELO detects ~9 times more galaxies with Hα emission (at $z\sim0.4$) per comoving volume, despite the huge difference in the sky areas explored in both surveys. This result holds even if we consider the effect of the

CV, which in case of pencil beam surveys like OTELO, is an important source of uncertainty. For the Hα ET-ELG in OTELO, this uncertainty amounts to $> 40\%$. Furthermore, we found that for the volume limited Hα, [O III], and Hβ SDSS samples the ratio $\aleph_{\rm OTELO}/\aleph^{EL}_{\rm SDSS}$ slightly increases, thus confirming our results even in the presence of a possible luminosity evolution. It is worth noting that the OTELO ET-ELG sample is not corrected for completeness and that more than 50% of the sources with *EW* lower than 5Å are not detected by OTELO. Thus, the number densities estimated from the OTELO survey in this work should be taken as a lower limit. Our results also demonstrate that (i) we should expect finding more ETs in future space- and ground-base deep surveys than those would be expected from the Local Universe estimations, pointing to a significant evolution in the population of ET-ELG, and (ii) the potential of deep blind spectroscopic surveys, like OTELO, in recovering emission lines at intermediate redshift.

5.5 Discussion

In this Chapter we report an unprecedented discovery of 14 ET-ELG at seven different redshift windows ($0.4 < z < 1.1$). These windows corresponds to seven different emission lines as seen by the OTELO survey (i.e.: Hα, [O I], He I, [N I], [O III], Hβ, and Hγ). Considering strong emission lines, i.e., Hα, [O III], and Hβ, at $z \sim 0.4, 0.8$ and 0.9 respectively OTELO detects 9, 2.6, and 3.6 times higher number density of ET-ELG than would be expected from local SDSS data. Our findings hold even considered uncertainties resulting from the cosmic variance. Furthermore, volume limited samples of Hα, [O III], and Hβ were selected in local SDSS data to account for the effects of a possible luminosity evolution, which could affect the count number.

Additional spectroscopic data is needed for a better understanding of the observed emission line properties, at least in the framework of the BPT diagnostic diagram. It also would help to disentangle (or confirm) the issue of the origin of the ionized gas together with its detailed properties, and test different theories about the possible source of ionization of each galaxy in our sample. As showed in Panuzzo et al. (2011), 80% of their samples with MIR *Spitzer* spectra show different signs of activity. They suggest star formation bursts, a low level AGN activity, or shocks as the possible ionization mechanisms, while the remaining 20% are passive galaxies showing no MIR emission or the polycyclic aromatic hydrocarbon emission. The MIR detection in almost 80 % of our sample gives us a preliminary evidence on the nature of these sources: the OTELO ET-ELG sample may be constituted by higher redshift counterparts of the MIR-detected sources observed by these authors. This is the scope of a future work.

Table 5.1. Density number ℵ and counts of ET-ELG in OTELO and SDSS.

EL	$z_{\rm min}$	$z_{\rm max}$	Δz	$\sigma_{\rm CV}$	Volume $[10^4{\rm Mpc}^3]$	N° ET-ELG OTELO	$\aleph_{\rm OTELO}$ $[10^{-3}{\rm Mpc}^{-3}]$	N° ET-ELG SDSS	$\aleph^{EL}_{\rm SDSS}$ $[10^{-3}{\rm Mpc}^{-3}]$	$\aleph_{\rm OTELO}/\aleph^{EL}_{\rm SDSS}$ [a]
col. 1	col. 2	col. 3	col. 4	col. 5	col. 6	col. 7	col. 8	col. 9	col. 10	col. 11
Hα	0.376	0.415	0.039	0.42	0.1666	3	1.8	10 491	0.2005	9.0
[O I]	0.434	0.475	0.041	0.40	0.2139	2	0.9	10 362	0.1980	4.7
He I	0.537	0.581	0.044	0.37	0.3082	1	0.3	8 137	0.1555	2.1
[N I]	0.737	0.787	0.049	0.31	0.5125	1	0.2	...	...	...
[O III]	0.804	0.855	0.052	0.30	0.5838	3	0.5	10 491	0.2005	2.6
Hβ	0.858	0.911	0.053	0.29	0.6422	3	0.5	6 844	0.1308	3.6
Hγ	1.081	1.140	0.059	0.26	0.8808	1	0.1	7 545	0.1441	0.8
SDSS	0.04	0.095	0.055	0.07	5233.5	...	...	10 491	0.2005	...

[a] Ratio of $\aleph_{\rm OTELO}$ to $\aleph^{EL}_{\rm SDSS}$ (ratio of col. 7 over the product of col 6 times col 10 rounded to the first decimal); values are not corrected for $\sigma_{\rm CV}$. In the case of SDSS sample Δz and $\sigma_{\rm CV}$ are fixed to the redshift range used in this work, while value of $\sigma_{\rm CV}$ for SDSS main survey region are from Driver & Robotham (2010), and both are stated for illustrative purposes. Furthermore, note that the values for Hα, and [O III] in col. 9 and 10 are the same because we use these lines in the selection process. Columns 7 and 9 show the total number of sources with a particular EL in OTELO and SDSS, respectively.

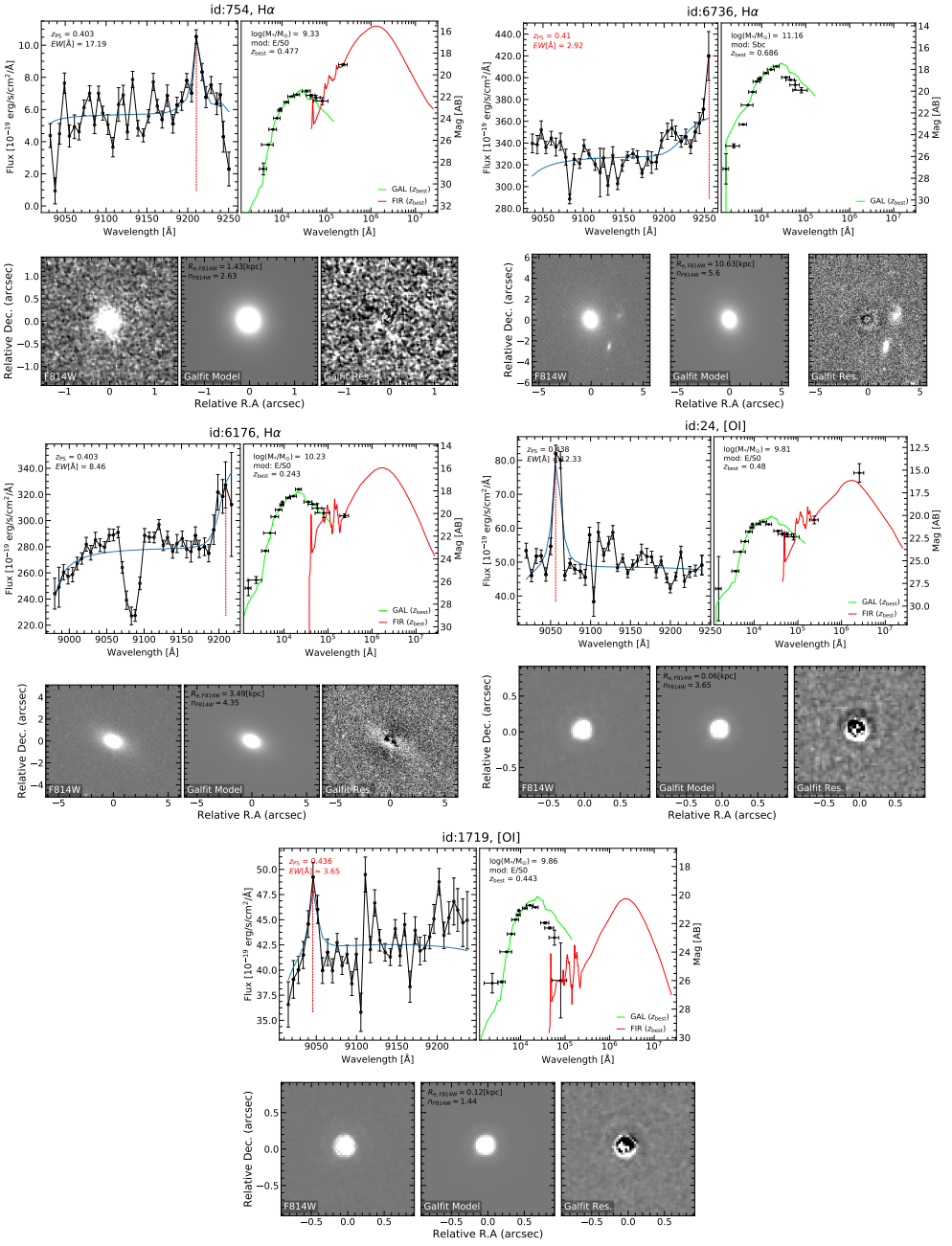

Figure 5.7. Informative cards for all Hα and [O I] sources in the sample. *Left top panel:* black line and dots and blue line represent observed and deconvolved PS; filled black dots show data points included in the emission line fit indicated by vertical red dashed line at $z_{\rm PS}$. Legend in red indicates $EW < 5$ Å. *Right top panel:* Best SED fit from `LePhare`. We include also FIR template if fitted. Photometric points used in the fitting process are shown in black. Vertical error bars represent the photometric errors, while horizontal errors show band widths. The templates are $z_{\rm BEST}$-redshifted. On the bottom part of each card is given the graphic result of the 2D Sérsic model fitting (from left to right: $F814W$ cutout, model and residual image).

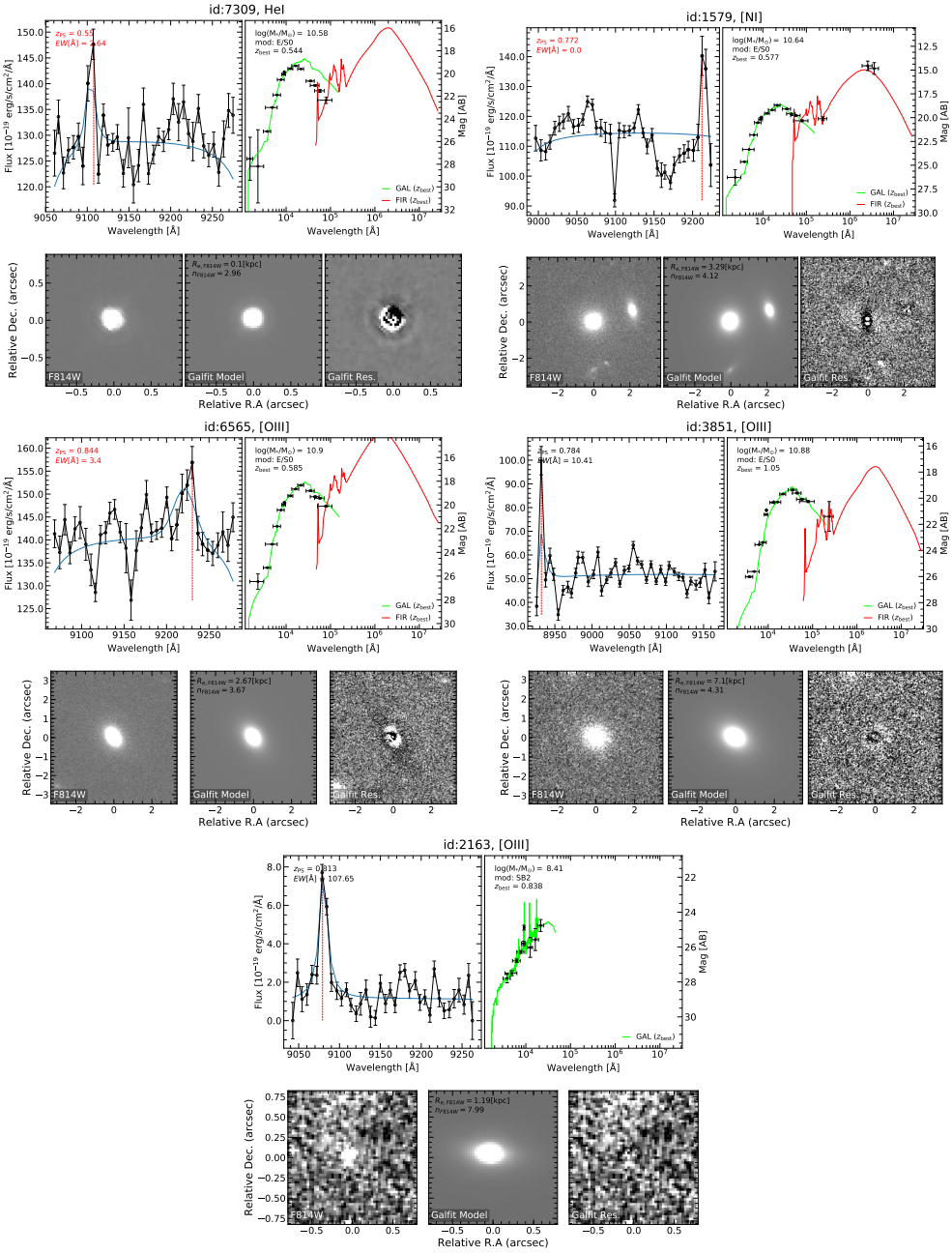

Figure 5.8. As Fig. 5.7 for He I, [N I] and [O III] sources.

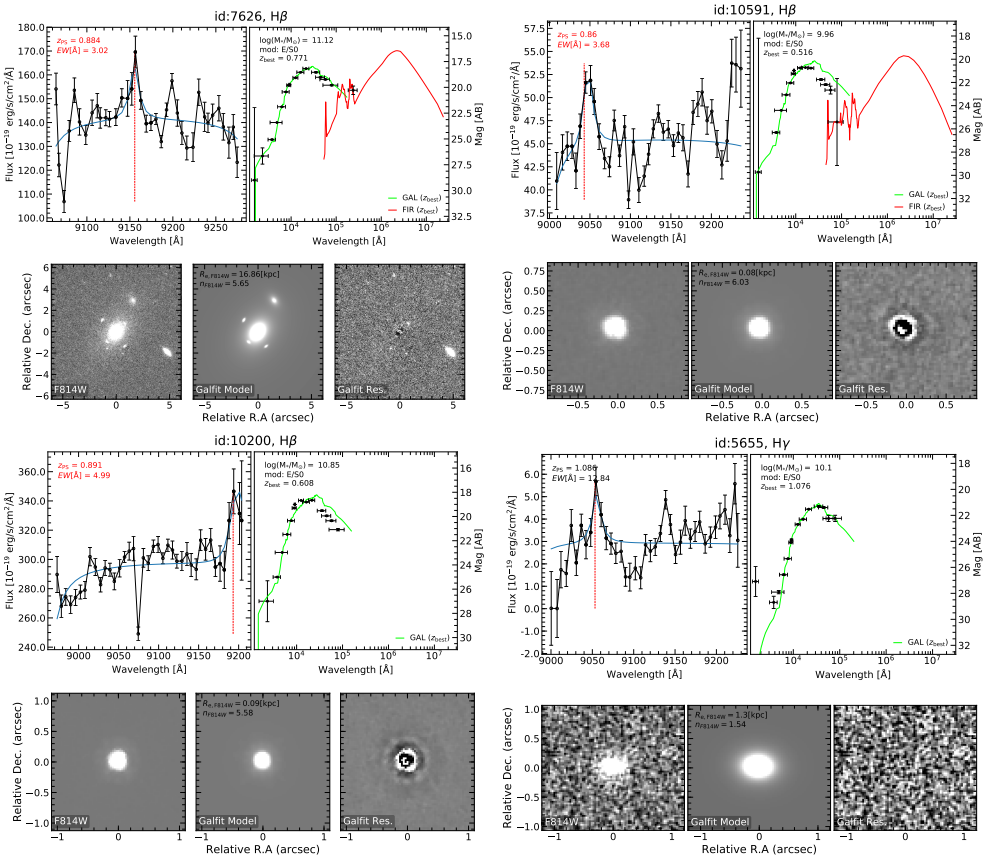

Figure 5.9. As Fig. 5.7 for Hβ and Hγ sources.

6

Mass-metallicity relation

A sample of low-mass Hα emission line sources at $z \sim 0.4$ is studied in the context of the mass-metallicty relation (MZR) and its possible evolution. This study aims to explore the MZR in the very low-mass regime. Our sample reaches stellar masses (M_*) as low as $\sim 10^7 M_\odot$, where 63% of the sample have $M_* < 10^9\, M_\odot$. This Chapter is based on the already published work in (Nadolny et al. 2020).

6.1 Introduction

The stellar mass (M_*) and gas-phase metallicity (Z) are among the most fundamental properties of galaxies and tracers of galaxy formation and evolution. While the stellar mass provides information about the amount of gas that is locked up into stars, the metallicity gives indications on the history of star formation and the exchange of gas between an object and its environment.

The mass-metallicity relation (MZR) has been studied for several decades, beginning with the pioneering work of Lequeux et al. (1979). Since then, several authors have investigated the origin and behaviour of this relationship in low and high redshifts, and in different environments and mass regimes. Tremonti et al. (2004) studied this relation for $> 53\,000$ star-forming galaxies (SFGs) in a demonstration of the statistical power of the SDSS. They found a tight correlation (± 0.1 dex) between stellar mass and metallicity, spanning over three orders of magnitude in stellar mass (down to $10^{8.5} M_\odot$), and a factor of 10 in

metallicity, with a median redshift of 0.1. Possible explanations of the origin of the MZR include gas outflows. In this scenario, low-mass galaxies suffer a stronger effect because they have lower escape velocities and can more easily loose enriched gas through stellar winds than massive galaxies. This scenario was first proposed by Larson (1974, see also Spitoni et al. 2010 and Tremonti et al. 2004). Furthermore, Belfiore et al. (2019) recently found that the inferred outflow loading factor decreases with stellar mass. The second possible explanation might be associated to the downsizing effect: massive galaxies process their gas faster, on shorter timescales and at earlier epochs than low-mass galaxies, where the star formation is slower and extends over longer periods (e.g. Cowie et al. 1996; Thomas et al. 2010). Another possible mechanism to explain the MZR is the dependence of stellar mass or star formation rate (SFR) on the initial mass function (IMF; e.g. Köppen et al. 2007; Gunawardhana et al. 2011). However, it is still a matter of debate which of these mechanisms (or a combination of them) plays the most important role in the formation and evolution of star-forming galaxies.

With the advent of large surveys, there has been an effort to observe fainter and higher redshift objects because they would provide strong constraints on our understanding of how galaxies evolve. For instance, using data from GAMA survye (see Sec. 2.2.4), Lara-López et al. (2013) found an evolution of metallicity of $\sim$ 0.1 dex for massive galaxies at redshift $\sim$ 0.35. At higher redshifts, using VVDS data, Lamareille et al. (2009) studied the MZR up to $z \sim 0.9$. They defined two samples: a wide ($i_{\rm AB} < 22.5$) and a deep sample ($i_{\rm AB} < 24$). They used three different metallicity calibrators depending on the redshift range. All methods are normalized to the Charlot & Longhetti (2001) calibrator, which is in agreement with the Tremonti et al. (2004) metallicities. Assuming that the MZR shape is constant with redshift, they found a stronger metallicity evolution in the wide sample, and concluded that the MZR is flatter at higher redshift. They arrived at the same conclusion for the luminosity-metallicity relation (LZR) in the wide sample.

There is an incentive to also analyse the low-mass end of the MZR because a flattening in this relation has been reported. For instance, Jimmy et al. (2015) found a flattening of the MZR relation using a sample of local (D $<$ 20 Mpc) dwarf galaxies with the VIMOS integral field unit (IFU) spectrograph on the VLT. They also found a clear dependence of the MZR and LZR on SFR and H I-gas mass. They used this finding to explain the observed scatter at the low-mass ($< 10^8 M_\odot$) end of these relations. Using a sample of 25 dwarf galaxies, Lee et al. (2006) also extended the MZR for galaxies down to a $M_* \sim 10^6\ M_\odot$, roughly 2.5 dex lower in stellar masses than Tremonti et al. (2004). Using *Spitzer* mid-IR (MIR) (4.5 μm) photometry, they found a comparable scatter in the MZR over 5.5 dex in stellar mass. They concluded that if galactic winds are responsible

for the MZR, an increasing of the dispersion is expected, contrary to what they found in their analysis.

A clear extreme in the MZR is given by extremely metal-deficient (XMD) galaxies ($\leq 0.1\ Z_{\odot}$). As found by Thuan et al. (2016), XMD galaxies show a clear trend of increasing gas mass fraction with decreasing metallicity, mass, and luminosity. On the same line, Sánchez Almeida et al. (2014, 2015) have argued that the low metallicities of the XMD galaxies are an indicator of pristine gas infall. However, Thuan & Izotov (2005) found that low metallicity alone cannot explain the hard ionising radiation observed in blue compact dwarf (BCD) galaxies, and proposed fast radiative shocks (velocity > 450 km s^{-1}) associated with supernovae explosions of massive Population III stars. Ekta & Chengalur (2010) examined the MZR of XMD galaxies and compared it with the MZR of BCD and dwarf irregular galaxies. They proposed that XMD galaxies are extremely metal depleted due to better mixing of the inter-stellar medium (ISM).

The fact that there are outliers of the MZR makes the situation even more interesting. Peeples et al. (2008) found a sample of 41 local ($z < 0.048$), low-mass, high-oxygen abundance outliers from the Tremonti et al. (2004) SDSS-based relation. They argued that these compact, isolated, and morphological undisturbed sources may be transitional dwarf galaxies. Their red colours (approaching or on the red sequence) and low gas fraction suggest that they are in the final stage of their star formation period. Moreover, using a larger sample of galaxies from the SDSS and DEEP2 surveys with stellar masses down to $10^7 M_{\odot}$, Zahid et al. (2012) found that the properties of low-mass metal-rich galaxies (the outliers from MZR) are, in agreement with previous works, possible transitional objects between gas-rich dwarf irregular and gas-poor dwarf spheroidal and elliptical galaxies.

In consideration of previous studies, we wish to shed light on the low-mass end of the MZR. To this aim, we study a sample of low-mass Hα emission line sources (ELS) at redshift ~ 0.4, firstly described in Ramón-Pérez et al. (2019). In what follows we describe the selection process, metallicity estimation, and finally the analysis of the MZR, (s)SFR, MSR, and morphology.

6.2 Sample selection of Hα + [N II] emitters

We used the OTELO data described in Section 2.1 to select the Hα sample as follows.

(a) We selected sources with $z_{\rm best}$ in the range $0.2 < z_{\rm best} < 0.5$ with the same error requirement described in Section 2.1.4. A total number of sources in this redshift window is 2 289. In this selection we lost some Hα + [N II]

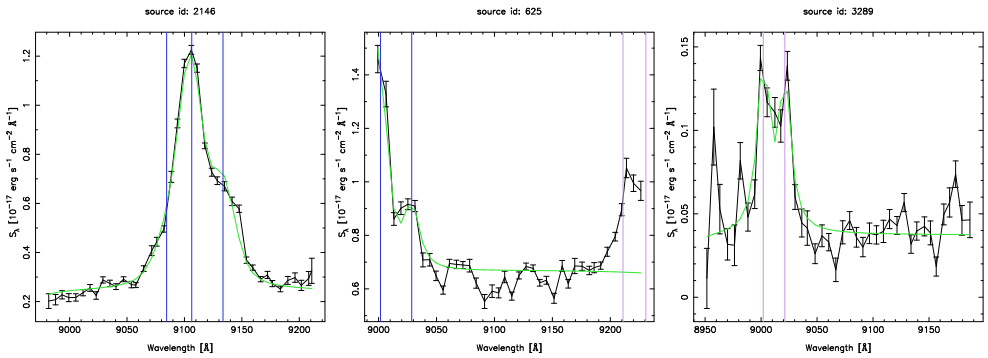

Figure 6.1. Pseudo-spectra of selected sources. From left to right: Source `id: 2146` with a clear Hα + [N II] emission line complex at z=0.387; source `id: 625` with Hα (truncated in the blue side) and [N II] emission lines and [S II]λ6716 (on the red side of the spectrum) at z=0.371; and source `id: 3289,` which exhibits the [S II]$\lambda\lambda$6716,6731 doublet at z=0.340. The green line shows the best-fit synthetic spectrum after the deconvolution process described in Sec. 3.4

candidates whose best $z_{\rm phot}$ would be obtained with `AGN/QSOs` libraries instead of galaxy templates. However, since we want to study SFGs, this does not affect the goals of this work. In addition, we are also aware that our selection includes possible Hα emitters with [S II]λ6716, or [S II]$\lambda\lambda$6716,6731 at $z \sim 0.3$. Examples of these are showed in Figure 6.1. Within this set of 2 289 sources, we found 73 preliminary ELS candidates to Hα + [N II], i.e., these sources display an emission feature in their PS using the same procedure as in the case of ET-ELG (Section 5.2; for details of the procedure see Bongiovanni et al. 2019). The best-fit templates $\rm SED_{best}$ correspond to Scd, Im, or SFGs types, with the exception of two sources where the best solution of $z_{\rm phot}$ was provided by an E/S0 galaxy type.

(b) We visually inspected the 73 candidates using our web-based GUI where all data about a user-selected source can be displayed; in particular, it includes the PS, the thumbnails of the images in available bands, and the `SExtractor` segmentation maps together with high-resolution *HST* images, $z_{\rm phot}$ solution including and excluding $\rm OTELO_{\mathit{deep}}$ photometry obtained from our photo-z analysis and their comparison with the input photometry, the $z_{\rm phot}$ solution from the CFHTLS T0004 Deep3 photo-z catalogue, and the $z_{\rm spec}$ from DEEP2, i.e. all the auxiliary redshift information add to the multi-wavlenght OTELO catalogue (as described in Section 2.1).

The high-resolution *HST*-ACS images allow us to identify possible contamination of the PS from neighbouring sources that are not resolved in the ground-based images. The comparison of the $\rm SED_{best}$ and the source data, together with

the additional redshift estimates (obtained in our analysis, from the CFHTLS $z_{\rm phot}$ catalogue, and from the objects with DEEP2 $z_{\rm spec}$) allows us to evaluate the confidence in our $z_{\rm phot}$ solution. Finally, the PS allow us to distinguish between Hα + [N II] SFG sources, [S II]$\lambda\lambda$6716,6731, or AGN galaxies with Hα + [N II] emission. We took advantage of the fact that the N2 index (ratio of [N II]λ6583 over Hα) must be lower than 0.4 (using the extreme case used by Pettini & Pagel 2004, see below) in SFGs. In addition, the [S II]λ6716 over [S II]λ6731 line ratio must range between 1.49 and 0.44 (see McCall 1984 and Cedrés et al. 2013 in the context of tunable filters). This means that any doublet where the line redwards ([N II]λ6583 or [S II]λ6731) is stronger than about half of the blueward line (Hα or [S II]λ6716) should be a Hα + [N II] AGN or a [S II]$\lambda\lambda$6716,6731 source. This process reduced the sample of 73 candidates to a sample with 18 sources where Hα and [N II]λ6583 can be measured. In addition, we also obtained a $z_{\rm PS}$ value (from the web-based GUI; as in the case of the ET-ELG in Sec. 5.2), which was obtained by the association of the brightest RTF slice and the Hα emission line at a given observed wavelength.

(c) As a final cross-check, we searched for objects with DEEP2 spectroscopic redshift in the range of $0.35 \leq z_{\rm spec} \leq 0.42$, which covers the range where Hα line would be detected in the OTELO spectral window. This redshift range would overlap with [S II]$\lambda\lambda$6716,6731 sources ($0.32 \leq z \leq 0.38$). DEEP2 data provides 18 sources in common with our selection in point (b): 9 of them do not show any emission feature in the OTELO PS, and 7 of them are in common with our selection from point (b). The remaining 2 objects had a best $z_{\rm phot}$ solution for the galaxy library outside of our redshift selection range (although one of them provides a $z_{\rm phot}$ solution in the Hα + [N II] range using the `AGN/QSOs` library with a Sy-2 galaxy template). After a visual inspection of the PS, we verified that one source of this set is indeed a Hα + [N II] emitter (`id: 625`) and the second one displays only the [N II]λ6583 line (and [S II]$\lambda\lambda$6716,6731 lines on the red side, `id: 6059`) in its PS. We therefore included only `id: 625` source in the final sample, which increases to 19 objects. We note that this additional source was not included in the preliminary ELS list since the emission line is truncated in one extreme of the PS (see the middle panel of Figure 6.1), but it was selected as a Hα + [N II] SFG candidate with the colour-magnitude ELS selection technique (Pascual et al. 2007) that is traditionally used in deep narrow-band surveys (see also Section 1.1). In our case, a ($z-$OTELO$_{\rm int}$) colour was obtained for all the OTELO sources detected in z band. The OTELO$_{\rm int}$ is the photometry obtained from the OTELO$_{deep}$ image (see Section 2.1).

The recovery of a preliminary ELS through a colour-magnitude diagram instead of using the flux-excess in PS, as indicated above, is an exception. As can be inferred from the description of this survey, OTELO combines the advantages

Table 6.1. Number of sources in the selected Hα samples.

sample	source number
Total	11237
Preliminary ELS	5322
Preliminary ELS in $z_{\rm phot}$range	2289
Hα ELS candidates	73
used Hα ELS	19

Hα sample	
AGN	3
Hα with metallicity	11
Hα with $f_{[\rm N\ II]\ \lambda6583}$ limit (low-flux sources)	5

of the deep narrow-band surveys, that imperatively use the colour-magnitude selection technique, but whose sensitivity to low values of observed EW is constrained by the passband of the narrow-band filter used, with the strengths of the conventional spectroscopic surveys, but without their selection biases and long observing times required. This has allowed us to reach the line flux and EW sensitivities reported in Section 1.4.

In summary, the final sample of Hα ELSs SFG candidates consists of 19 sources; hereafter we refer to this as the Hα sample. Further refinements (i.e. the flux and metallicity estimations) are described in the following sections. The examples given in Figure 6.1 show a PS for a Hα + [N II] source (`id: 2146`), a source with a truncated Hα and [S II]λ6716 emitter (`id: 625`) and a [S II]$\lambda\lambda$6716,6731 source (`id: 3289`, not in the Hα sample). The top part of Table 6.1 shows a summary of the number of sources at different steps of the selection process.

6.2.1 Local and high-z comparison samples

In order to compare our results of the MZR with other surveys we made use of the SDSS, GAMA and VVDS data described in Section 2.2. The high-z and local samples were selected as follow.

From SDSS and GAMA datasets we considered only the SFGs selected through the BPT diagram (Baldwin et al. 1981), using the criteria of Kauffmann et al. (2003a). In both surveys, the stellar masses were estimated using

SED templates from Bruzual & Charlot (2003) and a Chabrier (2003) IMF. SDSS fit templates to the observed SEDs, while stellar masses in GAMA were estimated using $(g - i)$ colours and a mass–luminosity relation (Taylor et al. 2011).

We selected the following sub-samples from the SDSS (local and high-z) and the GAMA surveys: (i) a local SDSS sample with $0.005 < z < 0.1$ and a S/N ratio > 3 for Hα and S/N > 4 for the [N II] emission line, and (ii) a higher redshift sample (high-z SDSS and GAMA) with $0.3 < z < 0.33$ (upper-z limit due to the Hα line visibility in both surveys). The emission line S/N imposed for both high-z samples was the same as in (i).

Furthermore, to ensure completeness for the higher redshift samples, we imposed a cut in stellar mass of $10^{10} M_{\odot}$. This cut is given by the limit in completeness of SDSS (see Weigel et al. 2016), and it approximately corresponds to an I-band absolute magnitude limit of $M_i \sim -21$ [AB]. These selection processes guarantee that we are using robust and complete samples from both surveys.

Considering VVDS (Deep and Ultra Deep samples) we adopted the following criteria: a redshift quality flag $1 <$ `ZFLAG` < 11 (this removes possible AGN from the sample, as described in Garilli et al. 2008), and a redshift range of 0.3(Deep)/0.2 (Ultra-Deep) $< z < 0.42$. We decided to use $z = 0.2$ as the lower redshift limit for Ultra-Deep in order to increase the final number of sources.

6.3 Metallicity estimation of Hα sample

To obtain gas-phase metallicities and AGNs contamination, we used the N2 index defined as

$$\mathrm{N2} = \log \frac{f([\mathrm{N\ II}]\ \lambda 6583)}{f(\mathrm{H}\alpha)}, \tag{6.1}$$

which requires a flux estimate. To this end, we used the inverse deconvolution of the PS, fully described in Section 3.4, here however we provide a summary of the method. In short, we assumed rest-frame model spectra defined by a constant continuum level, and Gaussian profiles of the [N II]λ6548, Hα, and [N II]λ6583 lines defined by their amplitude and a common line width for the three lines. The model to be compared with observational data is thus defined by the parameters $f_{\mathrm{mod}}(z, f_c, \sigma_{\mathrm{line}}, f_{[\mathrm{N\ II}]\ \lambda 6548}, f_{\mathrm{H}\alpha}, f_{[\mathrm{N\ II}]\ \lambda 6583})$. We performed 10^6 Monte Carlo simulations for each object and varied the different parameters. The different parameters varied in following ranges. The redshift was varied in

the range $z_{\rm PS} \pm 0.001$. The line width $\sigma_{\rm line}$ varied from 20 to 500 km/s rest-frame values, which translates into a range of 0.43 to 11 Å in spectral units at the Hα wavelength. The continuum f_c level varied in the range $f_{med,c} \pm \sigma_{\rm med,c}$ with $f_{\rm med,c}$ the median of the PS and $\sigma_{\rm med,c}$ the root mean square around $f_{\rm med,c}$. The rest-frame $f_{\rm H\alpha}$ amplitude varied between $f_{\rm med,c}$ and the maximum value observed in the PS, $f_{\rm PS}^{\rm max}$ taking into account the observational error $\sigma(f_{\rm PS}^{\rm max})$, and taking into account the assumed Gaussian profile. This is given by Eq. 3.8. The rest-frame $f_{\rm [N\ II]\ \lambda6583}$ varied between $0.006 \cdot f_{\rm H\alpha}$ and the maximum possible value given by Eq. 3.8. Finally, the rest-frame $f_{\rm [N\ II]\ \lambda6548}$ was fixed to $1/3 \cdot f_{\rm [N\ II]\ \lambda6583}$ (Osterbrock & Ferland 2006).

Each model was convolved with the OTELO filter response to produce a synthetic PS that was compared with the observed PS, and the corresponding χ^2 was obtained. The Monte Carlo simulations were designed to sample the multiparametric probability density function (PDF) from which modal values (i.e. best-fit solutions), and different confidence intervals around the modal value are obtained for each parameter (see details in Section 3.4). In what follows, the error bars are defined by the confidence intervals, which includes 25% and 68% (which would be the equivalent of $\pm 1\sigma$ for the Gaussian case) of the total area of the PDF around the modal value as an estimate of the errors. The redshift value obtained for each source after deconvolution (hereafter $z_{\rm OTELO}$) are given in Table 6.3. Formally, the common maximum uncertainty of these values is about $0.001(1+z_{\rm OTELO})$, as established in Bongiovanni et al. (2020).

We note that the possible flux-related parameters we obtained are strongly correlated, that is, each model has its own N2 index (i.e. metallicity), line equivalent widths, and so on, because the variation in one of the parameters of the model non-trivially affects the possible best solutions of the other parameters. In this way, we also obtained the corresponding PDFs of all the associated parameters (equivalent widths, N2 indices, and oxygen abundances). For all these inferred quantities we performed a posteriori operations over the entire Monte Carlo set associated with each particular object. The corresponding PDFs (and associated errors) of the particular quantities can be obtained as shown in Section 3.4. In the case of $f_{\rm H\alpha}$, we corrected the model values for possible stellar absorption of underlying older components following Hopkins et al. (2003, 2013) using a $EW_{\rm c}$ correction value of 2.5 Å, given by

$$F_{\rm H\alpha}^{\rm cor} = \frac{EW_{\rm H\alpha} + EW_{\rm c}}{EW_{\rm H\alpha}} \times F_{\rm H\alpha}^{\rm mod}, \tag{6.2}$$

where $F_{\rm H\alpha}^{\rm mod}$ and $F_{\rm H\alpha}^{\rm cor}$ are the model fluxes before and after the stellar absorption correction, respectively, and $EW_{\rm H\alpha}$ refers to the equivalent width of the model before correction.

Finally, we computed the gas-phase oxygen abundance from the N2, with the absorption corrected $F^{\rm cor}_{\rm H\alpha}$ value by means of equation 1 of Pettini & Pagel (2004) for all simulations:

$$12 + \log\,({\rm O/H}) = 8.90 + 0.57 \times {\rm N2}. \tag{6.3}$$

Nominal values and errors for metallicities were calculated by analysing the metallicity PDF obtained from the Monte Carlo simulations, but we did not take the intrinsic dispersion in the calibration into account, which would be ±0.41 (±0.18) dex at 95% (68%) confidence interval (Pettini & Pagel 2004). Table 6.3 shows the resulting $f_{\rm H\alpha}$, $EW_{\rm H\alpha}$ (both including the correction for stellar absorption), $f_{\rm [N\ II]\ \lambda6583}$, and $12 + \log({\rm O/H})$ (without calibration uncertainty) values with their 68% confidence intervals in columns 6, 8, 7, and 5, respectively.

We note that by construction, the inverse deconvolution process always provides a solution for the intensity of the $f_{\rm [N\ II]\ \lambda6583}$ value (defined as $0.006 \cdot f_{\rm H\alpha}$), which would correspond to a $12 + \log({\rm O/H}) = 7.63$ (before the stellar absorption correction). These values would be below the OTELO line flux limit of $\sim 5{\times}10^{-19}$erg/s/cm^2 as occurs for five objects. These cases translate into a large uncertainty in the resulting N2 and metallicity values. We refer to these objects as low-flux sources and can only provide a $f_{\rm [N\ II]\ \lambda6583}$ (hence metallicity) lower limit.

In addition, the Pettini & Pagel (2004) method is valid in the range of $-2.5 < {\rm N2} < -0.3$, which corresponds to the 7.47 to 8.73 of $12 + \log({\rm O/H})$ range. This range correspond to N2 (or metallicity) values found in our sample (see Figure 6.2). Values of $12 + \log({\rm O/H})$ equal to 8.67 would correspond to N2= −0.4, which defines an empirical division between SFGs and AGNs as found in Stasińska et al. (2006). Thus, in order to remove possible AGNs from our sample, we used the same method as in Ramón-Pérez et al. (2019, as for narrow-line AGN in the framework of the OTELO survey), that is, the Cid Fernandes et al. (2010) diagnostic diagram ($EW_{\rm H\alpha}$ vs. N2) shown in Figure 6.2. In this Figure, additionally to the Stasińska et al. (2006) limit (red dashed line), the green and blue dashed lines are the limits of the empirical metallicity estimations from Yin et al. (2007) and Pettini & Pagel (2004) of −0.5 and −0.3, respectively. In this way, we found three sources as possible AGN and excluded them from the further analysis. The lower part of Table 6.1 shows the summary of sources of different classes after the inverse deconvolution and AGN discrimination process.

Finally, we corrected the Hα fluxes for dust attenuation using the reddening values obtained from `LePhare` SED fitting (quoted in the second column of Table 6.3), and the empirical relation by Calzetti et al. (2000) estimated for galaxies at z=0.5 by Ly et al. (2012). We note that this is a lower value of

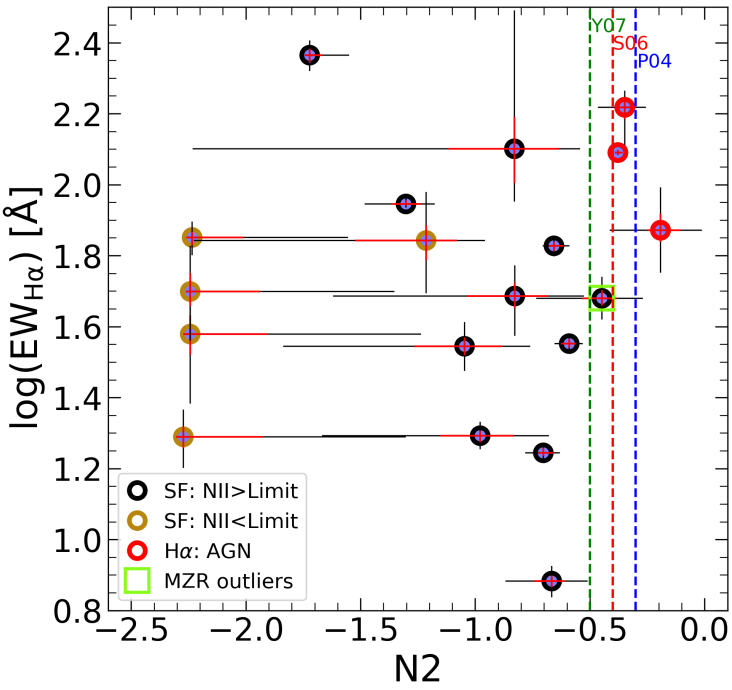

Figure 6.2. N2 index vs. $EW_{\mathrm{H}\alpha}$. Blue pints show all the Hα candidates. Black and golden circles represent sources with an [N II] line flux above and below OTELO flux limit, respectively (see Section 6.3 and Bongiovanni et al. 2020). Red circles show AGN candidates selected using the Stasińska et al. (2006) empirical limit of N2= −0.4. Vertical green and blue dashed lines show the Yin et al. (2007) and Pettini & Pagel (2004) limits of their calibration using the N2 index, respectively. The red line shows the AGN selection limit from Stasińska et al. (2006). The error bars in each object correspond to the 25% and 68% confidence interval around the most probable value.

$L(H\alpha)$ because the extinction is obtained from the fit of galaxy templates whose intrinsic extinction is unknown. The derived values of $E(B-V)$ are in the range of 0.0 and 0.3 mag, which is consistent with the extinction expected for low-mass galaxies, as shown in previous studies (e.g. Domínguez Sánchez et al. 2014). We also note that `LePhare` does not provide an evaluation of the uncertainty in $E(B-V)$, therefore the uncertainty in this term was not taken into account to evaluate the uncertainty in $L(H\alpha)$ (hence in the SFR, see following Sec. 6.3.1). The Hα line fluxes were used to derive SFRs following the standard calibration of Kennicutt (1998), but including the correction for a Chabrier (2003) IMF (see Kennicutt & Evans 2012, their Table 1) , which is the one used in this work:

$$\mathrm{SFR}(\mathrm{M}_{\odot} yr^{-1}) = 5.37 \times 10^{-42} \mathrm{L}(\mathrm{H}\alpha)[\mathrm{ergs}^{-1}]. \tag{6.4}$$

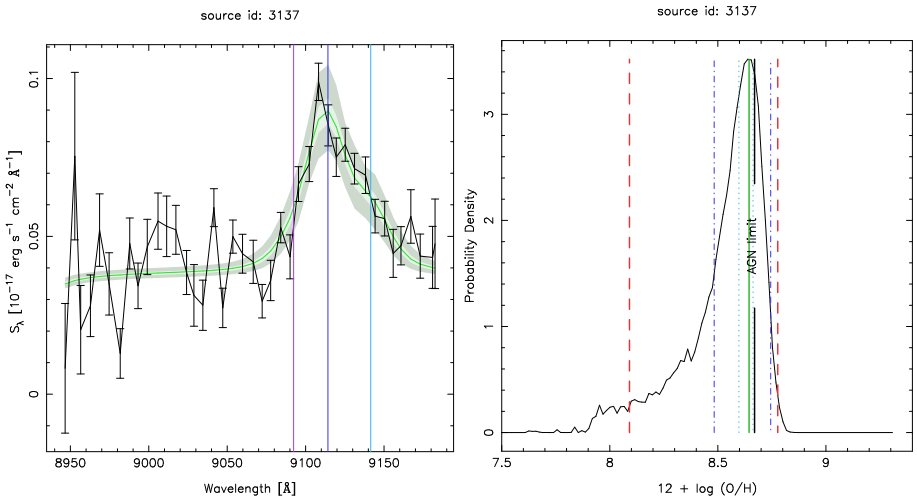

Figure 6.3. Pseudo-spectrum and metallicity PDF of source `id:3137`

The specific SFR (sSFR) was subsequently estimated as SFR/M_*. The resulting SFR and its associated uncertainty are listed in column 9 in Table 6.3.

6.3.1 Uncertainty in SFR

The uncertainty in the SFR quoted in Table 6.3 requires some cautions. First of all, the SFR requires the use of an extinction value. We used the value that was obtained with the best-fit solution with the `LePhare` software and used empirical galaxy templates. This choice implies that the extinction value is a lower limit because the intrinsic extinction of the templates are unknown. In addition, `LePhare` does not provide an evaluation of the uncertainty in $E(B-V)$, therefore this uncertainty was not included in the SFR. Finally, we recall that our $f_{\mathrm{H}\alpha}$ uncertainty does not correspond to a variance (where standard propagation theory would apply), but to a confidence interval. Taking these considerations into account, we computed the uncertainty in the SFR by applying the same formulae as we used to obtain the nominal SFR (the extinction correction used by Ly et al. 2012 and the SFR estimate using the Kennicutt & Evans 2012 relation) to the $f_{\mathrm{H}\alpha}$ values that define the 68% confidence interval. We stress that the uncertainty values would be underestimated because they do not include all the possible sources of uncertainty (interstellar extinction in particular). In Figure 6.3 we show examples of probability density functions and the confidence intervals of the best model of PS, as well as for the metallicity estimated via N2 index using relation showed in equation 6.3.

6.4 Analysis and discussion

6.4.1 Mass-metallicity relation

In this section we compare our results with the high-z SDSS, GAMA, and VVDS-Deep and Ultra-Deep samples. Finally, a comparison is made with the local SDSS sample in order to shed light on the possible evolution of the MZR at the low-mass end. The selection process of these comparison sets is given in Section 6.2.1.

In Figure 6.4 we show the local SDSS sample of galaxies up to $z\sim$ 0.1 together with higher redshift samples up to $z\sim$ 0.33 from GAMA and SDSS with their respective second-order polynomial fits [$12+\log(\mathrm{O/H}) = a+bx+cx^2$ where $x = \log M_*/M_\odot$]. Both high redshift samples were selected to be complete in mass and luminosity at a given redshift. It is worth noting that the OTELO sample is three orders of magnitude deeper in stellar mass than the two surveys at similar redshift. This is due to the depth of the OTELO survey (line flux down to 4.6×10^{-19}erg/s/cm^2, see Chapter 1, and Bongiovanni et al. 2020) and its potential as a blind spectroscopic survey to pre-select ELSs according to their PS and not only as a result of the colour excess in the colour-magnitude diagram.

In Figure 6.4 we also show the selected sample from the VVDS-Ultra-Deep survey: after our selection process, we are left with 10 sources from a total of 1125 in the redshift range $0.2 < z < 0.42$ with $z_{\mathrm{mean}} = 0.26$, which is much wider than our SFG sample redshift range ($0.36 < z < 0.42$). The highest redshift in the selected VVDS-Ultra-Deep sample is $z \sim 0.33$. The VVDS-Ultra-Deep survey data were processed in a consistent way with our data: (i) Hα fluxes were corrected for stellar absorption (eq. 6.2) and for intrinsic extinction (in this case, using the Balmer decrement), (ii) we estimated the N2 index, SFR (assuming a Chabrier IMF) and sSFR (using VVDS stellar masses), and (iii) we removed sources with N2> -0.4 as possible AGNs. We note that this sample spans the same range of metallicities, but covers a smaller range in stellar masses. We argue that this shows the capacity of the OTELO survey to recover the low-mass end of the observed galaxy population, even with its limited area of $\sim$ 56 arcmin^2 and despite the limited spectral range (230Å wide, centred at 9175Å).

In order to shed light on the possible evolution of the MZR, we compared our result with the local SDSS sample. The fit from Tremonti et al. (2004) is valid in the range of $8.5 < \log M_*/M_\odot < 11.5$, while our sample reaches masses as low as $\log M_*/M_\odot\sim$ 6.8 (where 63% of the sample with $\log M_*/M_\odot < 9$), therefore we did not use it. In Figure 6.4 we show our second-order polynomial

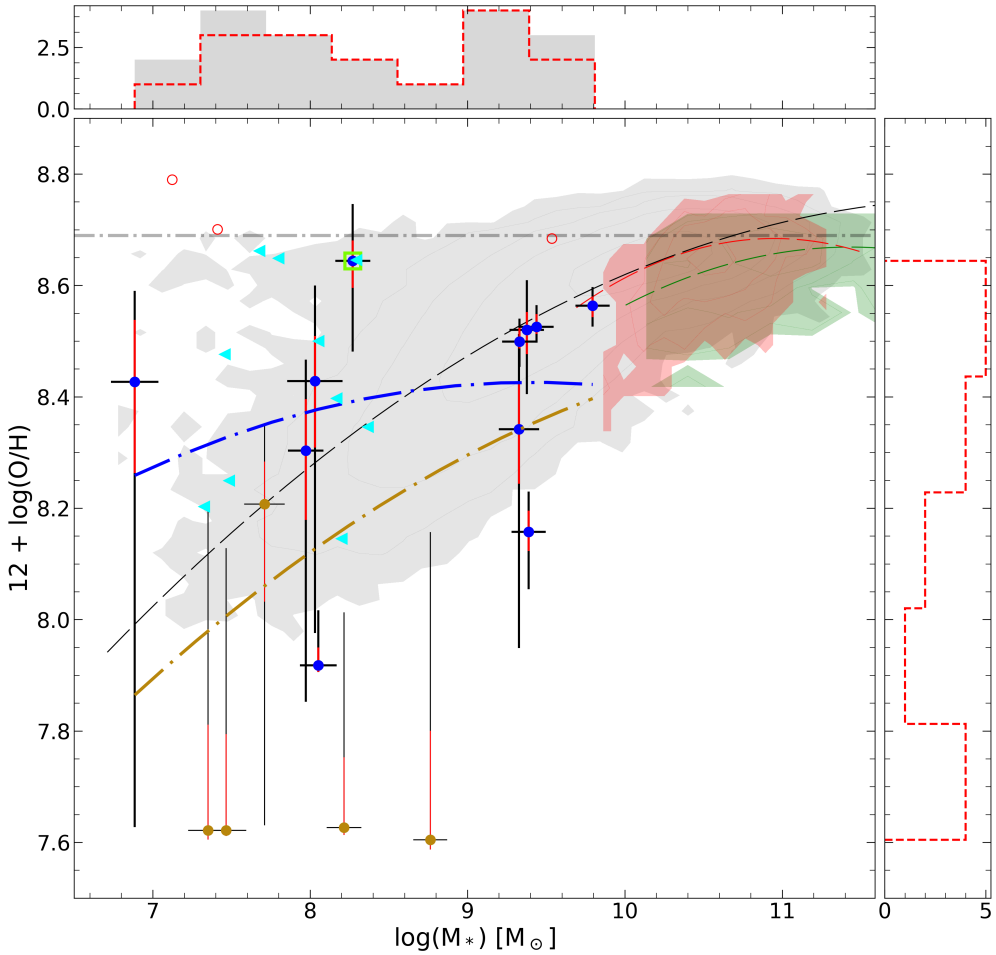

Figure 6.4. Mass-metallicity relation for OTELO Hα ELS. Blue and golden markers represent sources with an [N II]λ6583 line flux above and below OTELO flux limit, respectively. The light green empty square shows the MZR outlier as defined by Peeples et al. (2008). Cyan triangles show the VVDS-Ultra-Deep selected sample with $z_{\rm mean}$ = 0.26. Grey filled contours show local SDSS SFGs. Green filled contours show the high-z SDSS sample. Red filled contours show the SFG sample from the GAMA survey. All fits shown in this figure represent second-order polynomial fits. The blue dot-dashed line is the OTELO MZR fit to the sources with an [N II] line flux above the OTELO line flux limit, and the golden dot-dashed line shows the OTELO MZR including low-flux sources; the black thin dashed line shows the fit to the local SDSS sample; and green and red dashed lines show the SDSS and GAMA samples at z$\sim$0.3, respectively. The error bars correspond to the 25% (red) and 68% (black) confidence interval around the most probable value. The calibration uncertainty in metallicity is not included.

Table 6.2. Polynomial coefficients of the MZR fits shown in Figure 6.4 in the form $12 + \log(\mathrm{O/H}) = a + bx + cx^2$, where $x = \log M_*/M_\odot$.

sample	a	b	c
OTELO SF z=0.38	6.103	0.494	-0.026
OTELO SF low-lim	4.836	0.620	-0.026
SDSS $z < 0.1$	4.798	0.644	-0.026
SDSS z=0.31	1.987	1.169	-0.051
GAMA z=0.32$^{(1)}$	-0.752	1.723	-0.079

$^{(1)}$ Coefficients from second-order polynomial fit of the GAMA data below z=0.2.

fit to the local SDSS sample. From our SFG sample we identified those sources with [N II]λ6583 flux below the OTELO line flux limit (low-flux sources). Since for these low-flux sources our metallicity estimate has a large uncertainty, we provide two MZR fits: the first is obtained using sources with an [N II]λ6583 flux that is higher than the OTELO line flux limit (points and dot-dashed line in blue), and the second includes low-flux sources (points and dot-dashed line in gold). In both fits we limited the c parameter to be not greater than the c parameter from fit of the local SDSS sample. Additionally, we show in this figure the MZR second-order polynomial fits of the local ($z< 0.1$) and high-z (~ 0.31) SDSS and GAMA ($z\sim 0.32$) samples.

Our sample lies within the distribution of local SDSS MZR. Although our fit of the sources whose [N II]λ6583 line flux exceeds the OTELO line flux limit is flatter at the low-mass end, we cannot conclude that there is an evolution of the MZR because of the uncertainty in the metallicity of the low-flux sources. In the cases of the the fit that include low-flux sources (golden symbols), our fit approximates to the local SDSS MZR, especially at the low-mass end. All the fitted polynomial coefficients are listed in Table 6.2.

In Figure 6.4, the upper histogram represents the mass distribution where the red dashed line shows the pure SFG sample, and the grey filled histogram also includes possible AGNs (which are not included in the MZR). The "gap" in the M_* distribution between $\sim 10^{8.5}$ and $10^9\,M_\odot$ is a statistical effect due to the low number of sources in the sample. The right-hand histogram shows the metallicity distribution. The peak around ~ 7.6 is associated with low-flux sources with an [N II]λ6583 line flux that is lower than the OTELO flux limit. This corresponds to the hard limit of our method when it recovers line fluxes from PS, and also for the use of N2 as a metallicity estimator.

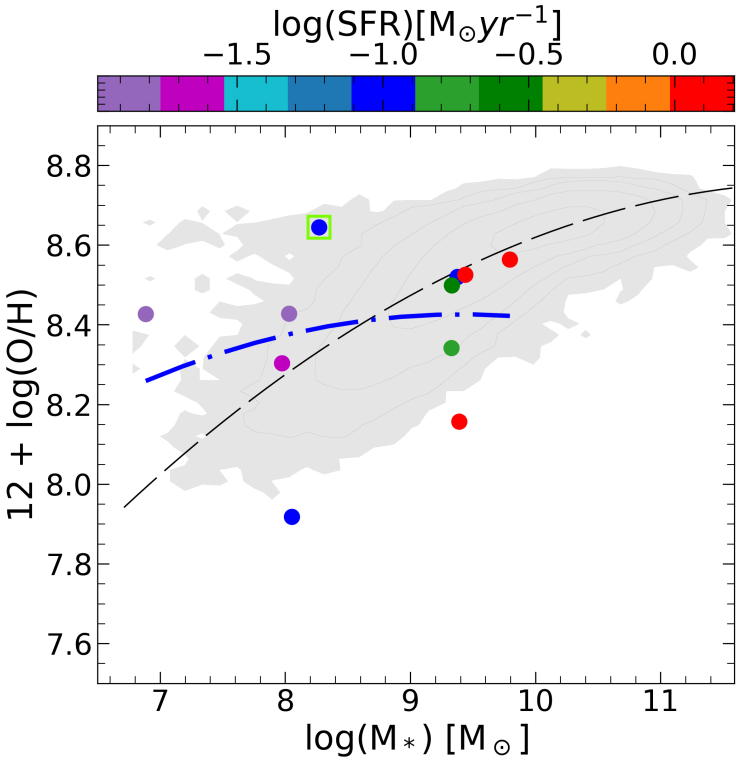

Figure 6.5. Mass-metallicity relation and SFR for OTELO Hα ELS. Points represent sources with [N II] flux above OTELO flux limit. Blue dot-dashed line represent second-order polynomial fit. Gray filled contours show the local SDSS sample. Black dashed line represent second-order fit to SDSS sample. Colours of the points represent SFR as indicated in colour-bar on the top of the figure.

6.4.2 Mass, metallicity, and SFR

As proposed by Lara-López et al. (2010a), the stellar mass, metallicity, and SFR are correlated and may be reduced to a fundamental plane (FP), a relationship among these three relevant characteristics of star-forming galaxies. In Figure 6.5 we represent a 2D version of the FP, i.e., we show mass-metallicity relation including however, information about SFR. This Figure is similar to Fig. 6.4, but showing only sources with [N II] flux above OTELO flux limit, together with best fit to this sub-sample. We can notice that the most massive sources in this sub-sample have also the highest SFR. Our sample, however, is too small to make any further statements.

In Figure 6.6 we show further scaling relationships between SFR, sSFR, M_*

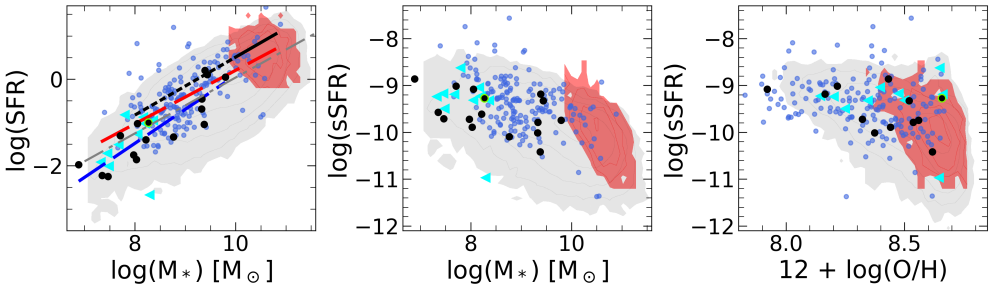

Figure 6.6. Star formation rate and sSFR as a funcion of stellar mass and metallicity. In all panels, black markers show the OTELO SFG sample, green empty circles show transitional dwarf galaxies, cyan triangles show the VVDS-Ultra-Deep data, blue dots show the VVDS-Deep data, and contours in red and grey show the GAMA and local SDSS samples, respectively. In the left panel we show the linear fits to our SFG sample (blue dashed line), VVDS Deep+Ultra-Deep (both selected sub-samples from VVDS, red dashed-line), and the fit from (Noeske et al. 2007, black solid line), which is given in the mass range of 10^{10} to $10^{11} M_{\odot}$, and the black dashed line is an extrapolation of their fit down to $10^{8} M_{\odot}$. The grey dashed line shows the linear fit of the local SDSS sample. For clarity we do not plot the estimated dispersions for any fit.

, and metallicity. On this Figure we represent the selected sub-samples from local SDSS, GAMA, VVDS (Deep and Ultra-Deep), and our Hα SFG sample. The left panel of this figure shows the dependence of the SFR on the stellar mass. Noeske et al. (2007) explored this relation over a wide range of redshifts between $0.2 < z < 1.1$, with the mass complete down to $\sim 10^{10}$. They found a main sequence of this relation for SFGs over cosmic time with a slope of 0.67. Our sample reaches three orders of magnitude lower in stellar mass than the work of Noeske et al. (2007). We find a linear relation with a slightly higher slope of 0.78 ± 0.11, but shifted down by ~ 0.25 dex. This shift is associated with the different mass ranges in the two datasets.

Using data from merged VVDS Deep and Ultra-Deep survey samples, we obtain a linear fit with a slope of 0.61 ± 0.03, shown in the same figure. We note that this fit approximates ours at the high-mass end. Our fit is in agreement with previous studies within the estimated dispersion. We find no evolution of this relation from the local Universe to $z = 0.4$. Our Hα sample is consistent with the local SDSS sample, as can be seen not only in the spatial distribution, but also in the linear fits of the two samples. Our sample has moderate SFRs, ranging from $-2.2 \lesssim \log(\mathrm{SFR}) \lesssim 0.2\ M_{\odot}\mathrm{yr}^{-1}$. VVDS covers this relation with a similar dispersion from the high-mass (Deep) down to the low-mass (Ultra-Deep) regime; the VVDS-Ultra-Deep sample reaches the mean mass of the OTELO Hα sample ($M_{*} \sim 10^{8.3}\ M_{\odot}$).

The middle and right panels of this figure show the relationship of sSFR with M_* and metallicity, respectively. There is no clear evidence of evolution as compared with the local SDSS sample. In both cases the sSFR is anti-correlated with M_* and metallicity (middle and right panel, respectively). Moreover, these relations hold up to $z = 0.4$ down to the low-mass regime for the OTELO and VVDS samples.

6.4.3 Mass-size relation

In Figure 6.7 we show the M_*–size relation (MSR) for the Hα sample we studied. We estimated the physical half-flux radius r_e using the effective radius from the Sérsic model (described in Chapter 4) and $z_{\rm OTELO}$ (r_e values are given in the last column of Table 6.3). From a linear fit we obtain an intercept of -1.41 ± 0.73, and a slope of 0.19 ± 0.09. In this fit we used 13 sources from the SFG sample that had available M_* and r_e measurements. Here we compare our MSR with Ichikawa et al. (2012), who studied galaxies from the MOIRCS Deep Survey (Kajisawa et al. 2009) in the GOODS-North region at $0.3 < z < 3$, and in a mass range of $M_* \sim 10^8$-$10^{11} M_\odot$. They found a universal slope of the MSR (independent of redshift and galaxy activity, SFGs or quiescent, for a given mass) of $R \propto {M_*}^\alpha$, with $\alpha \sim 0.1 - 0.2$. Figure 6.7 shows a fit from Ichikawa et al. (2012) for colour-selected SFGs at $0.25 < z < 0.5$ with a slope of 0.115, using their Eq. 3 with the parameters given in their Table 1.

In Figure 6.7 we also show a linear fit from van der Wel et al. (2014) for colour-selected SFGs from the 3D-*HST*/CANDELS at $z \sim 0.25$ (equation and values as given in their Table 1). We found that our results agree with those from Ichikawa et al. (2012). We argue that this is due to the mass range studied in both works.

6.4.4 Morphology

In Chapter 4 we have studied morphological parameters of the selected sample of OTELO's galaxies. A total of 14 Hα galaxies were included in the *morphological sample* and were subsequently analysed (i.e., with meaningful results, see Sec. 4.2).

In Figures 4.11 – 4.17 we show Hα sample as blue circles (filled or empty). We found that great majority of the analysed sources show properties (i.e., $(u-r)$, Sérsic index n, stellar masses $\log M_*/M_\odot$, physical sizes), compatible with late-type galaxies. This is also confirmed by the visual classification described in Section 4.4, and showed in Figure 4.16: 9 sources are classified as disk galaxies, one as tadpole, two as spheroidal, while further two were unclassified. The

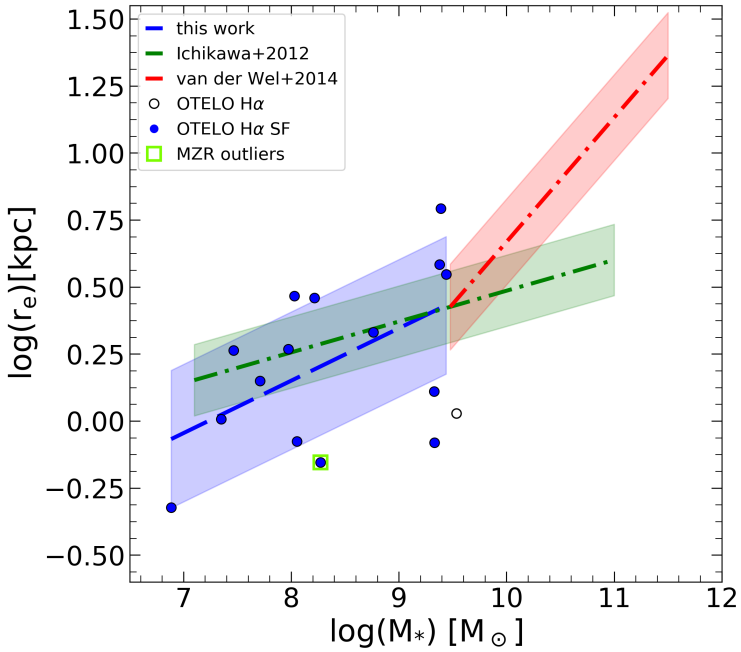

Figure 6.7. Physical half-light radius r_e as a function of the stellar mass M_*. Black empty circles show the Hα sample, and blue markers show SF galaxies (in both cases we show sources for which it was possible to measure both variables). The green square shows the outlier of the MZR. The blue dashed line represents the linear fit in a form y= a + bx to the Hα sample with a=-1.41±0.73 and b=0.19±0.09. The green dot-dashed line shows the linear fit from Ichikawa et al. (2012), with a logarithmic slope of 0.115. The red dot-dashed line shows the linear fit found by van der Wel et al. (2014), with a slope of 0.25. The green and red shaded regions represent the dispersion of the linear fit as estimated by Ichikawa et al. (2012) and van der Wel et al. (2014), respectively, while the blue shaded region shows the dispersion of our measurement estimated as the median absolute deviation of 0.2. Note that the sizes and stellar masses of the Hα sample are slightly different that these showed in Figure 4.14 due to small changes in the estimation process. We keep this figure as it is published in Nadolny et al. (2020). The overall results remain unchanged.

median values of the I-band Sérsic index of the Hα sample per morphological class are very close to the median value of the *morphological sample*, as indicated by star-marker in the same figure.

As showed in Figure 4.15, the nominal errors of morphological parameters derived in `GALFIT-M` fall within the error distribution of the overall *morphological sample*. These are lower-limit errors as explained in Section 4.3.2.

6.4.5 Possible transitional dwarf galaxy

We identified one source as a possible transitional dwarf galaxy, which is the outlier of the MZR (see Figure 6.4 and 6.7, green square, source `id: 3137`; see also Fig. 6.3 where PS, and metallicity PDF are showed). The selection is based on the cuts in stellar mass $\log M_*/M_\odot < 9$ and metallicity $12+\log(\mathrm{O/H}) > 8.6$, following Peeples et al. (2008). According to these authors, it is most likely that sources with these characteristics are metal-rich dwarf galaxies. The percentage of metal-rich dwarf galaxies in our SFG sample is $\sim$6% (one source in our SFG sample) compared with less than 1% in the local SDSS sample selected with the same criteria. Morphologically, this source is visually classified as a disc with a Sérsic index $n = 1.25$, it is compact (0.7 kpc), and has a close companion (at least in projection). Peeples et al. (2008) studied a sample of 41 local ($z < 0.05$) metal-rich dwarf galaxies selected from the SDSS survey from Tremonti et al. (2004). They predicted that in order to have such high metallicity, these sources also need to have a lower gas fraction than objects with similar SFR and luminosities. They discussed other possible explanations for this behaviour: environment (interactions), effective yields, and finally the possibility that these sources are transitional dwarf galaxies at the end of their period of star formation. The outlier in our sample has a low stellar-mass $\log M_*/M_\odot = 8.2$, high metallicity $12+\log(\mathrm{O/H}) = 8.6$, low SFR of $\log \mathrm{SFR} \sim -1\ M_\odot \mathrm{yr}^{-1}$, and a high sSFR of $\log \mathrm{sSFR} \sim -9.2$. More information, in particular spectroscopic observations, is needed to disentangle its morphology and to shed light on its real nature.

6.5 Discussion

We studied the MZR and scaling relations between stellar mass, SFR, and sSFR, and the morphology of the low-mass Hα sample drawn from the OTELO survey at $z \sim 0.4$. We reach three orders of magnitude deeper in stellar mass ($\sim 10^{6.8} < M_*/M_\odot < 10^{10}$, with 57% of the sample with $M_* < 10^9 M_\odot$) than the SDSS and GAMA samples at similar redshift. The PS (data-product of OTELO survey) gives us the possibility to efficiently select and study the metallicity of these low-mass ELSs. About 95% of our ELS sample was selected from spectral features present in PS. If the colour-excess technique used in classical narrow-band surveys had been used instead, only half of this sample (i.e. necessarily the sources with larger observed EWs) would be recovered. For more details, see Bongiovanni et al. (2019) and Bongiovanni et al. (2020).

Because of the OTELO instrumental limits [as seen in the N2 index and/or $12 + \log(\mathrm{O/H})$], and the associated errors in the recovery of the line fluxes

together with the low number of objects in the sample, we cannot conclude about a possible MZR evolution that would be due to cosmic variance. Furthermore, our results are consistent with those obtained using the local SDSS sample (see Figure 6.4).

We also explored the SFR as a function of M_*, which has previously been studied by Noeske et al. (2007), who found the so-called main sequence. We showed that this relation holds for the sample we studied, but with a systematic shift by $\sim$ 0.25 dex in SFR, which is associated with the different stellar mass ranges used in Noeske et al. (2007) and in this work. Our data agree with the VVDS-Deep and Ultra-Deep data used in this work. Furthermore, the global distribution of the OTELO SFG sample lies within the local SDSS distribution.

From the automatic and visual morphological classification (see Section 4.3), we find that the majority of sources in the sample are discs (52%), followed by spheroids (10%) with median Sérsic indices of 1.31 and 2.2, respectively. One source is classified as tadpole ($\sim$5%). No classification is given for 31% of our sample because they are not detected in the high-resolution *HST*-ACS F814W image, have no data, or because the sources are just too faint to provide any reliable classification (did not classified to the *morphological sample*).

We obtained the M_*–size relation for our Hα sample. Our results agrees with those of Ichikawa et al. (2012), but have a slightly higher slope (0.14 and 0.115, respectively). The difference in the results in this work and in van der Wel et al. (2014) is probably due to the different range of stellar-masses that is covered in both studies (we reach almost three orders of magnitude deeper in M_* than van der Wel et al.).

We identified one candidate ($\sim$ 6% of our SFG sample) as a transitional dwarf galaxy with low mass $\log M_*/M_\odot = 8.6\,M_\odot$ and high metallicity $12 + \log(\mathrm{O/H}) = 8.64$. Considering the same criteria, we find less than 1% of these sources in the local-SDSS sample. Morphologically, this source is classified as a compact ($\sim$ 0.7 kpc) disc galaxy ($n = 1.25$) with blue ($g - i$) colour. The study of MZR, SFR, sSFR, and its colour and morphology suggest that this source is indeed a transitional dwarf galaxy at the end of its star formation period, as discussed in previous works (e.g. Peeples et al. 2008). More information is needed to conclude on this issue, however.

Table 6.3. Catalogue of the OTELO Hα SFG sample. AGN candidates are separated in the lower part of the table. Metallicity and SFR values for these sources need to be taken with caution.

idobj	EBV [mag]	$z_{OTELO}^{(a)}$	Mass [$\log(M_*/M_\odot)$]	12 + $\log(O/H)^{(b,c)}$	$f_{H\alpha}{}^{(b,d,e)}$	$f_{N\ II\ \lambda6583}{}^{(b,e)}$	EW(Hα)$^{(b,d)}$ [Å]	$SFR_{H\alpha}{}^{(f)}$ [$M_\odot yr^{-1}$]	n	r_e [kpc]
Sources with [N II]λ6583 above OTELO line flux limit.										
$625^{(1)}$	0.1	0.371	9.80 ± 0.10	$8.56^{+0.03}_{-0.04}$	$23.5^{+1.3}_{-1.1}$	$5.21^{+0.41}_{-0.53}$	$35.6^{+2.1}_{-1.6}$	$1.12^{+0.06}_{-0.05}$	—	—
754	0.3	0.404	9.33 ± 0.12	$8.34^{+0.17}_{-0.39}$	$1.14^{+0.10}_{-0.09}$	$0.119^{+0.092}_{-0.080}$	19.6 ± 1.7	0.21 ± 0.02	2.61 ± 0.09	1.29
1130	0.1	0.380	9.38 ± 0.10	$8.52^{+0.09}_{-0.11}$	$1.80^{+0.18}_{-0.16}$	$0.39^{+0.14}_{-0.13}$	7.65 ± 0.76	0.09 ± 0.01	1.92 ± 0.02	3.841
1873	0.1	0.379	9.39 ± 0.10	$8.16^{+0.07}_{-0.10}$	$32.07^{+0.51}_{-0.54}$	$1.60^{+0.48}_{-0.38}$	$88.2^{+1.8}_{-1.6}$	1.60 ± 0.02	2.15 ± 0.02	6.199
2747	0.1	0.380	9.33 ± 0.10	$8.50^{+0.04}_{-0.04}$	$6.95^{+0.30}_{-0.33}$	$1.38^{+0.25}_{-0.21}$	$17.57^{+0.78}_{-0.93}$	0.35 ± 0.02	1.78	0.832
3089	0.0	0.365	6.89 ± 0.14	$8.43^{+0.16}_{-0.80}$	$0.41^{+0.53}_{-0.09}$	$0.060^{+0.046}_{-0.060}$	126^{+168}_{-33}	$0.011^{+0.014}_{-0.002}$	1.95 ± 1.00	0.475
3106	0.0	0.368	8.03 ± 0.17	$8.43^{+0.17}_{-0.45}$	0.52 ± 0.10	$0.077^{+0.053}_{-0.060}$	$48.5^{+9.9}_{-11}$	0.014 ± 0.003	7.75 ± 0.10	2.931
$3137^{(2)}$	0.1	0.389	8.27 ± 0.10	$8.64^{+0.10}_{-0.16}$	$1.88^{+0.26}_{-0.18}$	$0.67^{+0.17}_{-0.22}$	$47.8^{+7.4}_{-5.4}$	0.10 ± 0.01	1.25 ± 0.01	0.702
7990	0.0	0.379	7.97 ± 0.11	$8.30^{+0.16}_{-0.45}$	0.63 ± 0.08	$0.056^{+0.054}_{-0.046}$	$35.1^{+4.9}_{-5.4}$	0.018 ± 0.002	1.47 ± 0.07	1.854
8074	0.1	0.372	9.44 ± 0.10	$8.53^{+0.04}_{-0.03}$	$27.0^{+1.1}_{-1.6}$	5.58 ± 0.41	$67.2^{+2.7}_{-4.4}$	$1.29^{+0.05}_{-0.08}$	0.65 ± 0.01	3.528
10512	0.0	0.380	8.05 ± 0.11	$7.92^{+0.10}_{-0.01}$	$3.29^{+0.12}_{-0.13}$	$0.06^{+0.06}_{-0.00}$	231^{+19}_{-18}	$0.094^{+0.003}_{-0.004}$	0.73 ± 0.07	0.84
Sources whose [N II]λ6583 is lower than the OTELO line flux limit.										
3854	0.3	0.372	7.71 ± 0.13	$8.21^{+0.14}_{-0.58}$	$0.332^{+0.085}_{-0.082}$	$0.020^{+0.063}_{-0.020}$	69^{+24}_{-20}	0.05 ± 0.01	1.24 ± 0.26	1.41
3855	0.0	0.373	7.35 ± 0.12	$7.62^{+0.57}_{-0.02}$	0.22 ± 0.07	$0.001^{+0.041}_{-0.001}$	37^{+16}_{-13}	0.006 ± 0.002	1.37 ± 0.25	1.017
7088	0.1	0.385	8.76 ± 0.11	$7.61^{+0.55}_{-0.02}$	$0.89^{+0.13}_{-0.16}$	$0.01^{+0.11}_{-0.01}$	$19.5^{+3.6}_{-3.8}$	$0.046^{+0.007}_{-0.008}$	2.47 ± 0.06	2.142
8713	0.0	0.379	7.47 ± 0.13	$7.62^{+0.51}_{-0.01}$	0.2 ± 0.05	$0.001^{+0.022}_{-0.001}$	50^{+16}_{-13}	0.006 ± 0.001	0.95 ± 0.15	1.835
9932	0.0	0.380	8.22 ± 0.11	$7.63^{+0.39}_{-0.01}$	$1.40^{+0.11}_{-0.12}$	$0.008^{+0.073}_{-0.008}$	$71.0^{+6.8}_{-7.7}$	0.04 ± 0.003	0.86 ± 0.05	2.878
AGN candidates.										

Continued on next page

Table 6.3 – *Continued from previous page*

idobj	EBV [mag]	$z_{\rm OTELO}^{(a)}$	Mass [$\log(M_*/M_\odot)$]	12 + $\log({\rm O/H})^{(b,c)}$	$f_{\rm H\alpha}{}^{(b,d,e)}$	$f_{\rm N\ II\ \lambda6583}{}^{(b,e)}$	EW(Hα)$^{(b,d)}$ [Å]	$\rm SFR_{H\alpha}{}^{(f)}$ [$M_\odot {\rm yr}^{-1}$]	n	r_e [kpc]
2146	0.3	0.387	9.54 ± 0.10	8.68 ± 0.01	30.88 ± 0.20	$12.92^{+0.20}_{-0.00}$	$123.22^{+0.36}_{-0.53}$	5.06 ± 0.03	2.18 ± 0.03	1.069
3373	0.0	0.373	7.12 ± 0.13	$8.79^{+0.10}_{-0.12}$	$0.25^{+0.05}_{-0.04}$	0.157 ± 0.05	74^{+22}_{-17}	0.007 ± 0.001	—	—
4893	0.1	0.385	7.41 ± 0.21	$8.70^{+0.05}_{-0.07}$	0.61 ± 0.06	0.20 ± 0.05	165^{+16}_{-32}	0.032 ± 0.003	—	—

(1) Object selected via DEEP2 redshift, see Section 6.2 for details.
(2) Possible transitional dwarf galaxy.
(a) Uncertainty on $z_{\rm OTELO}$ is $\pm 0.001\,(1 + z_{\rm OTELO})$.
(b) Uncertainty defined as the 68% confidence interval around the mode.
(c) Uncertainty in metallicity does not include calibration uncertainty.
(d) Corrected for stellar absorption.
(3) In the units of [10^{-17} erg s^{-1} cm^{-2}]
(f) Lower limit; see Section 6.3.1 for the uncertainty evaluation.

7

Conclusions

The OTELO catalogue and its data-products has been exploited in this thesis. On this basis we provide insights on the morphology of the overall OTELO sources, the number counts of early-type emission line galaxies, as well as the mass-metallicity relation.

In the morphological study we have employed the high-resolution images from *HST*-ACS. These images have given us the opportunity to provide morphological parameters for ∼8 000 sources. These were carefully matched to the OTELO sources catalogue resulting in a final sample of ∼3 000 galaxies with *meaningful* results, which were subsequently analyzed. We found that the model based parameters (i.e. Sérsic index, physical sizes, magnitudes and colours) are in the ranges of expected values for ET and LT galaxy population. The visual classification has also confirmed these findings. Furthermore, we found no evidence for evolution of the mass-size relation up to $z = 2$. Moreover, investigating the median size evolution we found good agreement with previous works.

From the *morphological sample* we have selected a sample of early-type galaxies with emission (ET-ELG). This selection was based on the morphological parameters derived in this thesis, observed $(u - z)$ colour, and on the emission feature visible in their PS. We have found 14 robust ET-ELG at seven different redshifts as defined by the emission line detected in PS. Then we estimated the number densities for each of the cosmic volume under consideration. We have compared the OTELO's number densities with the local SDSS-based sample of ET-ELG.

In the last part of this thesis, we have focused on the star-forming galaxies. We have investigated the mass-metallicity relation of the Hα emitters at $z \sim 0.4$. A total of 19 Hα sources were selected through a careful procedure involving semi-automatic and visual inspection of PS, as well as the inverse deconvolution process to derive emission line proprieties. Employing the N2 index (i.e., ratio of [N II] and Hα) we have separated AGNs from SFGs, and for the latter ones we have estimated metallicities and (specific) star formation rates.

In what follows we present the main conclusions of this thesis.

- The morphological catalogue of ∼8 000 sources found in the OTELO field was presented. To this end we register homogeneously all of 11 *HST* images available with accuracy better than one *HST* pixel. Using the multi-wavelength version of `GALFIT` we provide the morphological parameters for a substantially high number of sources as compared with previous works, especially at the low signal-to-noise regime ($I > 26$ mag). For a sub-sample of carefully selected objects, we provide a detailed analysis of the methods to separate ET and LT galaxy populations up to $z = 2$. In the following we list particular findings.
  - We have confirmed the claims that the multi-wavelength version of `GALFIT` is more robust in the low S/N regime, as stated in Häussler et al. (2013). To this end we have compared our results with the ACS-GC catalogue from Griffith et al. (2012) where exactly the same data in the same field have been used. However, the ACS-GC catalogue is based on the single-band version of `GALFIT`. About 800 galaxies have been additionally recovered in this work. Furthermore, for the galaxies detected in both works, we recover meaningful results for a larger number of galaxies, especially in the faintest magnitude bins.
  - We showed several methods to separate ET from LT galaxies based on the derived parameters. These methods are based on the $(u-r)$ colour, Sérsic index, concentration index, and the ratio of Sérsic index in I-band to the same index measured in V-band. Moreover, we found a good agreement with the classification based on the fitted templates to spectral energy distribution.
  - We found no evidence for evolution of the mass-size relation up to $z = 2$. Using three redshift bins for both, ET and LT galaxy population, we found no significant differences between our intermediate galaxy population with the low-z galaxies studied in Lange et al. (2015). However, we note that due to the small sky area covered by the OTELO survey, we loose up to 60% of the high-mass end ($> 10^{11} M_{\odot}$) galaxies. This

is more evident in the further study of the median size evolution for a given stellar-mass, where several mass bins are not sufficiently populated. For stellar-masses bins where we have a robust statistics we find good agreement with previous studies. Furthermore, for the first time, we presented r_e–z relation for LT galaxies in two low stellar-mass bins ($\log M_*/M_\odot = 8$, and 9).

- We have tested the classical ET/LT colour separation from Strateva et al. (2001). Using the same cut of $(u - r) = 2.22$ we found that this method, even if derived for the local sample, can be used for galaxies at intermediate redshifts.

- The study of ET-ELG was based on the morphological catalogue as well as on the PS. We have tested the number densities of the intermediate redshift ET-ELG found in the OTELO survey, and compared these to the number densities estimated using local SDSS-based ET-ELG sample. In what follows we list the particular results.

  - We found 14 ET-ELG allocated at seven different redshifts, between 0.4 and 1.1, defined by emission line detected in OTELO PS. These sources have been confirmed by a careful inspection of all the available data.
  - Considering strong emission lines, i.e., Hα, [O III], Hβ, the OTELO survey detects 9, 2.6 and 3.6 times more ET-ELG than would be expected from the local SDSS sample.
  - We have investigated the impact of the uncertainties due to the cosmic variance σ_{CV}. We have estimated these errors for all the cosmic volumes studied. The highest $\sigma_{CV} \sim 40\%$ is found for the first cosmic volume where Hα line is observed. Taking into account σ_{CV} found for OTELO (for each cosmic volume) and for SDSS, OTELO still detects more ET-ELG. In the worst case (Hα emitters with the highest σ_{CV}), OTELO detects 4.8 times more ET-ELG than would be estimated from SDSS. The same is true for [O III], and Hβ when including the CV effects: OTELO detects 1.7 and 2.4 times more ET-ELG. This result may suggest that ET-ELG were more abundant in the past, and/or were more intense that local analogues.

- Finally, we have studied the stellar-mass–metallicity relation (MZR) of Hα sample at $z = 0.4$. Metallicity was estimated employing N2 index using line fluxes from the OTELO pseudo-spectra. The N2 index was also used to separate possible AGNs from our sample. In the following, we outline our results.

  - From the OTELO catalogue we selected a total of 19 galaxies with noticeable Hα + [N II] signatures in their PS. The selection process involved

semi-automatic method to search for emission in PS, photometric redshift cuts, and visual inspection.

- In order to estimate emission line proprieties we have used the inverse deconvolution process. We recovered line fluxes, equivalent widths EWs, and redshifts, including the associated uncertainties. Using line fluxes (i.e. the N2 index) and EWs we found 3 sources as possible AGN candidates, which were not taken into account in the MZR analysis.
- We studied MZR at the very low-mass end, with stellar masses between 10^7 and 10^{10}, this is three orders of magnitude lower than the lower mass reached in other surveys at the same redshift. We found no evidence for the evolution of this relation as compared to the local SDSS sample.
- We have found a general agreement of the (specific) star formation rate comparing with local, and high redshift counterparts from SDSS, VVDS, and GAMA surveys.
- We found that majority of the Hα sources with morphological parameters are visually classified as disks, with low Sérsic index, with only two sources classified as spheroidal. This is expected since star-forming activities are mostly found in late-type galaxies.
- We have also identified a possible transitional dwarf galaxy, i.e., the outlier of the MZR with low stellar-mass and high metallicity. All the evidences (i.e., Sérsic index and morphology, colours, stellar mass, metallicity and its (s)SFR) indicate that this particular source is at the end of its star formation period. More information is needed, however, to confirm these claims.

Summarizing, we have scientifically exploited several facets of the OTELO survey and its data-products. We provided, complementary to the OTELO multi-wavelength database, a catalogue with the morphological parameters for more than 8 000 sources. For a sub-sample of sources we have tested several method to separate ET from LT galaxies, finding a general good agreement with classification via templates. We have found no evidence for MSR evolution, and we have confirmed the median size evolution r_e–z for LT and ET up to $z = 2$. From the morphological catalogue we have selected robust sample of ET-ELG at seven different cosmic volumes, showing that OTELO detects more of these sources as compared with local SDSS ET-ELG sample. Finally we have studied the MZR for a carefully selected sample of Hα emitters at $z = 0.4$. No signs of evolution are evident as compared to the local SDSS Hα star forming galaxies.

All these findings show the potential of the OTELO survey to search for emission-line sources at the very low mass end.

Bibliography

Abell, G. O. 1958, ApJS, 3, 211

Abraham, R. G., Valdes, F., Yee, H. K. C., & van den Bergh, S. 1994, ApJ, 432, 75

Abraham, R. G., van den Bergh, S., & Nair, P. 2003, ApJ, 588, 218

Ahumada, R., Allende Prieto, C., Almeida, A., et al. 2020, ApJS, 249, 3

Alloin, D., Collin-Souffrin, S., Joly, M., & Vigroux, L. 1979, A&A, 78, 200

Andrae, R., Jahnke, K., & Melchior, P. 2011b, MNRAS, 411, 385

Andrae, R., Melchior, P., & Jahnke, K. 2011a, MNRAS, 417, 2465

Annibali, F., Bressan, A., Rampazzo, R., Zeilinger, W. W., & Danese, L. 2007, A&A, 463, 455

Annibali, F., Bressan, A., Rampazzo, R., et al. 2010, A&A, 519, A40

Arnouts, S., Cristiani, S., Moscardini, L., et al. 1999, MNRAS, 310, 540

Athey, A. E. & Bregman, J. N. 2009, ApJ, 696, 681

Baldry, I. K., Glazebrook, K., Brinkmann, J., et al. 2004, ApJ, 600, 681

Baldwin, J. A., Phillips, M. M., & Terlevich, R. 1981, PASP, 93, 5

Barden, M., Häußler, B., Peng, C. Y., McIntosh, D. H., & Guo, Y. 2012, MNRAS, 422, 449

Barden, M., Rix, H.-W., Somerville, R. S., et al. 2005, ApJ, 635, 959

Barro, G., Pérez-González, P. G., Gallego, J., et al. 2011, ApJS, 193, 13

Beckwith, S. V. W., Stiavelli, M., Koekemoer, A. M., et al. 2006, AJ, 132, 1729

Belfiore, F., Vincenzo, F., Maiolino, R., & Matteucci, F. 2019, MNRAS, 487, 456

Benítez, N., Dupke, R., Moles, M., et al. 2014, arXiv e-prints, arXiv:1403.5237

Bertin, E. & Arnouts, S. 1996, A&AS, 117, 393

Bertin, E., Mellier, Y., Radovich, M., et al. 2002, in Astronomical Society of the Pacific Conference Series, Vol. 281, Astronomical Data Analysis Software and Systems XI, ed. D. A. Bohlender, D. Durand, & T. H. Handley, 228

Bohlin, R. C., Colina, L., & Finley, D. S. 1995, AJ, 110, 1316

Bongiovanni, A., Bruzual, G., Magris, G., et al. 2005, MNRAS, 359, 930

Bongiovanni, Á., Ramón-Pérez, M., Pérez García, A. M., et al. 2019, A&A, 631, A9

Bongiovanni, Á., Ramón-Pérez, M., Pérez García, A. M., et al. 2020, A&A, 635, A35

Brammer, G. B., van Dokkum, P. G., Franx, M., et al. 2012, ApJS, 200, 13

Brinchmann, J., Charlot, S., White, S. D. M., et al. 2004, MNRAS, 351, 1151

Bruzual, G. & Charlot, S. 2003, MNRAS, 344, 1000

Byler, N., Dalcanton, J. J., Conroy, C., et al. 2019, AJ, 158, 2

Calzetti, D., Armus, L., Bohlin, R. C., et al. 2000, ApJ, 533, 682

Capetti, A. & Baldi, R. D. 2011, A&A, 529, A126

Cedrés, B., Beckman, J. E., Bongiovanni, Á., et al. 2013, ApJL, 765, L24

Cepa, J. 2008, The Emission-Line Universe

Cepa, J., Aguiar-Gonzalez, M., Bland -Hawthorn, J., et al. 2003, in Society of Photo-Optical Instrumentation Engineers (SPIE) Conference Series, Vol. 4841, Proc. SPIE, ed. M. Iye & A. F. M. Moorwood (SPIE), 1739–1749

Chabrier, G. 2003, ApJL, 586, L133

Charlot, S. & Longhetti, M. 2001, MNRAS, 323, 887

Cid Fernandes, R., Stasińska, G., Mateus, A., & Vale Asari, N. 2011, MNRAS, 413, 1687

Cid Fernandes, R., Stasińska, G., Schlickmann, M. S., et al. 2010, MNRAS, 403, 1036

Ciotti, L. 1991, A&A, 249, 99

Coleman, G. D., Wu, C.-C., & Weedman, D. W. 1980, ApJS, 43, 393

Conselice, C. J., Bershady, M. A., & Jangren, A. 2000, ApJ, 529, 886

Coupon, J., Ilbert, O., Kilbinger, M., et al. 2009, A&A, 500, 981

Cowie, L. L., Songaila, A., Hu, E. M., & Cohen, J. G. 1996, AJ, 112, 839

Davis, M., Guhathakurta, P., Konidaris, N. P., et al. 2007, ApJL, 660, L1

de Diego, J. A., Nadolny, J., Bongiovanni, Á., et al. 2020, A&A, 638, A134

de Souza, R. E., Gadotti, D. A., & dos Anjos, S. 2004, ApJS, 153, 411

de Vaucouleurs, G. 1959, Handbuch der Physik, 53, 275

Domínguez Sánchez, H., Bongiovanni, A., Lara-López, M. A., et al. 2014, MNRAS, 441, 2

Domínguez Sánchez, H., Huertas-Company, M., Bernardi, M., Tuccillo, D., & Fischer, J. L. 2018, MNRAS, 476, 3661

Donley, J. L., Koekemoer, A. M., Brusa, M., et al. 2012, ApJ, 748, 142

Dressler, A., Faber, S. M., Burstein, D., et al. 1987, ApJL, 313, L37

Dreyer, J. L. E. 1888, MemRAS, 49, 1

Driver, S. P., Hill, D. T., Kelvin, L. S., et al. 2011, MNRAS, 413, 971

Driver, S. P. & Robotham, A. S. G. 2010, MNRAS, 407, 2131

Ekta, B. & Chengalur, J. N. 2010, MNRAS, 406, 1238

Elmegreen, D. M., Elmegreen, B. G., Ravindranath, S., & Coe, D. A. 2007, ApJ, 658, 763

Fabry, C. & Pérot, A. 1901, ApJ, 13, 265

Freeman, K. C. 1970, ApJ, 160, 811

Gallego, J., Zamorano, J., Rego, M., & Vitores, A. 1993, in Astronomische Gesellschaft Abstract Series, Vol. 8, Astronomische Gesellschaft Abstract Series, 39

Garilli, B., Le Fèvre, O., Guzzo, L., et al. 2008, A&A, 486, 683

Gomes, J. M., Papaderos, P., Kehrig, C., et al. 2016, A&A, 588, A68

González, J. J., Cepa, J., González-Serrano, J. I., & Sánchez-Portal, M. 2014, MNRAS, 443, 3289

González-Otero, M., Padilla Torres, C. P., Cepa, J., & Lockman-SpReSO Team. 2020, in Contributions to the XIV.0 Scientific Meeting (virtual) of the Spanish Astronomical Society, 43

Goudfrooij, P. 1999, in Astronomical Society of the Pacific Conference Series, Vol. 163, Star Formation in Early Type Galaxies, ed. P. Carral & J. Cepa, 55

Goudfrooij, P., Hansen, L., Jorgensen, H. E., et al. 1994, A&AS, 104, 179

Graham, A. W., Driver, S. P., Petrosian, V., et al. 2005, AJ, 130, 1535

Griffith, R. L., Cooper, M. C., Newman, J. A., et al. 2012, ApJS, 200, 9

Grogin, N. A., Kocevski, D. D., Faber, S. M., et al. 2011, ApJS, 197, 35

Gunawardhana, M. L. P., Hopkins, A. M., Sharp, R. G., et al. 2011, MNRAS, 415, 1647

Häussler, B., Bamford, S. P., Vika, M., et al. 2013, MNRAS, 430, 330

Häussler, B., McIntosh, D. H., Barden, M., et al. 2007, ApJS, 172, 615

Hayashi, M., Tanaka, M., Shimakawa, R., et al. 2018, PASJ, 70, S17

Herpich, F., Stasińska, G., Mateus, A., Vale Asari, N., & Cid Fernandes, R. 2018, MNRAS, 481, 1774

Herschel, J. F. W. 1864, Philosophical Transactions of the Royal Society of London Series I, 154, 1

Hippelein, H., Maier, C., Meisenheimer, K., et al. 2003, A&A, 402, 65

Hopkins, A. M., Driver, S. P., Brough, S., et al. 2013, MNRAS, 430, 2047

Hopkins, A. M., Miller, C. J., Nichol, R. C., et al. 2003, ApJ, 599, 971

Hubble, E. P. 1925, ApJ, 62, 409

Hubble, E. P. 1926, ApJ, 64, 321

Hubble, E. P. 1936, Realm of the Nebulae (Yale University Press)

Huertas-Company, M., Gravet, R., Cabrera-Vives, G., et al. 2015, ApJS, 221, 8

Huertas-Company, M., Rodriguez-Gomez, V., Nelson, D., et al. 2019, MNRAS, 489, 1859

Huertas-Company, M., Rouan, D., Tasca, L., Soucail, G., & Le Fèvre, O. 2008, A&A, 478, 971

Humason, M. L. 1936, ApJ, 83, 10

Humason, M. L., Mayall, N. U., & Sandage, A. R. 1956, AJ, 61, 97

Ichikawa, T., Kajisawa, M., & Akhlaghi, M. 2012, MNRAS, 422, 1014

Ilbert, O., Arnouts, S., McCracken, H. J., et al. 2006, A&A, 457, 841

Jiménez-Teja, Y. & Benítez, N. 2012, ApJ, 745, 150

Jimmy, Tran, K.-V., Saintonge, A., et al. 2015, ApJ, 812, 98

Jones, D. H. & Bland-Hawthorn, J. 2001, ApJ, 550, 593

Jones, H., Renzini, A., Rosati, P., & Seifert, W. 2001, The Messenger, 103, 10

Joye, W. A. & Mandel, E. 2003, in Astronomical Society of the Pacific Conference Series, Vol. 295, Astronomical Data Analysis Software and Systems XII, ed. H. E. Payne, R. I. Jedrzejewski, & R. N. Hook, 489

Jura, M., Kim, D. W., Knapp, G. R., & Guhathakurta, P. 1987, ApJL, 312, L11

Kajisawa, M., Ichikawa, T., Tanaka, I., et al. 2009, ApJ, 702, 1393

Kartaltepe, J. S., Mozena, M., Kocevski, D., et al. 2015, ApJS, 221, 11

Kashikawa, N., Shimasaku, K., Yasuda, N., et al. 2004, PASJ, 56, 1011

Kauffmann, G., Heckman, T. M., Tremonti, C., et al. 2003a, MNRAS, 346, 1055

Kauffmann, G., Heckman, T. M., White, S. D. M., et al. 2003b, MNRAS, 341, 54

Kelly, B. C. & McKay, T. A. 2005, The Astronomical Journal, 129, 1287

Kelvin, L. S., Driver, S. P., Robotham, A. S. G., et al. 2012, MNRAS, 421, 1007

Kennicutt, R. C. & Evans, N. J. 2012, ARA&A, 50, 531

Kennicutt, Jr., R. C. 1998, ARA&A, 36, 189

Kinney, A. L., Calzetti, D., Bohlin, R. C., et al. 1996, ApJ, 467, 38

Knapp, G. R., Gunn, J. E., & Wynn-Williams, C. G. 1992, ApJ, 399, 76

Kocevski. 2015, initial release of the CANDELS morphology GUI

Koekemoer, A. M., Fruchter, A. S., Hook, R. N., & Hack, W. 2003, in HST Calibration Workshop : Hubble after the Installation of the ACS and the NICMOS Cooling System, ed. S. Arribas, A. Koekemoer, & B. Whitmore, 337

Köppen, J., Weidner, C., & Kroupa, P. 2007, MNRAS, 375, 673

Kormendy, J. 1977, ApJ, 218, 333

Kormendy, J. & Bender, R. 1996, ApJL, 464, L119

Krywult, J., Tasca, L. A. M., Pollo, A., et al. 2017, A&A, 598, A120

Kuchner, U., Ziegler, B., Verdugo, M., Bamford, S., & Häußler, B. 2017, A&A, 604, A54

Laird, E. S., Nandra, K., Georgakakis, A., et al. 2009, ApJS, 180, 102

Lamareille, F., Brinchmann, J., Contini, T., et al. 2009, A&A, 495, 53

Lange, R., Driver, S. P., Robotham, A. S. G., et al. 2015, MNRAS, 447, 2603

Lara-López, M. A., Cepa, J., Bongiovanni, A., et al. 2010a, A&A, 521, L53

Lara-López, M. A., Cepa, J., Castañeda, H., et al. 2010b, PASP, 122, 1495

Lara-López, M. A., Hopkins, A. M., López-Sánchez, A. R., et al. 2013, MNRAS, 433, L35

Larson, R. B. 1974, MNRAS, 169, 229

Le Fèvre, O., Cassata, P., Cucciati, O., et al. 2013, A&A, 559, A14

Le Fèvre, O., Vettolani, G., Garilli, B., et al. 2005, A&A, 439, 845

Lee, H., Skillman, E. D., Cannon, J. M., et al. 2006, ApJ, 647, 970

Lees, J. F., Knapp, G. R., Rupen, M. P., & Phillips, T. G. 1991, ApJ, 379, 177

Lequeux, J., Peimbert, M., Rayo, J. F., Serrano, A., & Torres-Peimbert, S. 1979, A&A, 80, 155

Lintott, C. J., Schawinski, K., Slosar, A., et al. 2008, MNRAS, 389, 1179

López-Sanjuan, C., Díaz-García, L. A., Cenarro, A. J., et al. 2018, arXiv e-prints, arXiv:1805.03609

López-Sanjuan, C., Le Fèvre, O., Ilbert, O., et al. 2012, A&A, 548, A7

Lutz, D., Poglitsch, A., Altieri, B., et al. 2011, A&A, 532, A90

Ly, C., Malkan, M. A., Kashikawa, N., et al. 2012, ApJL, 747, L16

Mahoro, A., Pović, M., Nkundabakura, P., Nyiransengiyumva, B., & Väisänen, P. 2019, MNRAS, 485, 452

Martin, D. C., Fanson, J., Schiminovich, D., et al. 2005, ApJL, 619, L1

Mayall, N. U. 1939, Lick Observatory Bulletin, 497, 33

McCall, M. L. 1984, Monthly Notices of the Royal Astronomical Society, 208, 253

Meert, A., Vikram, V., & Bernardi, M. 2014, Monthly Notices of the Royal Astronomical Society, 446, 3943

Moles, M., Benítez, N., Aguerri, J. A. L., et al. 2008, AJ, 136, 1325

Moster, B. P., Somerville, R. S., Newman, J. A., & Rix, H.-W. 2011, ApJ, 731, 113

Mowla, L. A., van Dokkum, P., Brammer, G. B., et al. 2019, ApJ, 880, 57

Nadolny, J., Bongiovanni, Á., Cepa, J., et al. 2021, A&A, Forthcoming

Nadolny, J., Lara-López, M. A., Cerviño, M., et al. 2020, A&A, 636, A84

Nair, P. B. & Abraham, R. G. 2010, ApJS, 186, 427

Navarro Martínez, R. et al. 2021, A&A, in perp.

Newman, J. A., Cooper, M. C., Davis, M., et al. 2013, ApJS, 208, 5

Ngan, W., van Waerbeke, L., Mahdavi, A., Heymans, C., & Hoekstra, H. 2009, MNRAS, 396, 1211

Nilson, P. 1973, Uppsala general catalogue of galaxies

Noeske, K. G., Weiner, B. J., Faber, S. M., et al. 2007, ApJL, 660, L43

Osterbrock, D. E. & Ferland, G. J. 2006, Astrophysics of gaseous nebulae and active galactic nuclei (University Science Books)

Ouchi, M., Shimasaku, K., Furusawa, H., et al. 2010, ApJ, 723, 869

Pandya, V., Greene, J. E., Ma, C.-P., et al. 2017, ApJ, 837, 40

Panuzzo, P., Rampazzo, R., Bressan, A., et al. 2011, A&A, 528, A10

Pascual, S., Gallego, J., & Zamorano, J. 2007, PASP, 119, 30

Peeples, M. S., Pogge, R. W., & Stanek, K. Z. 2008, ApJ, 685, 904

Peng, C. Y., Ho, L. C., Impey, C. D., & Rix, H.-W. 2002, AJ, 124, 266

Peng, C. Y., Ho, L. C., Impey, C. D., & Rix, H.-W. 2010, AJ, 139, 2097

Pérez-González, P. G., Cava, A., Barro, G., et al. 2013, ApJ, 762, 46

Pérot, A. & Fabry, C. 1899, ApJ, 9, 87

Pettini, M. & Pagel, B. E. J. 2004, MNRAS, 348, L59

Phillips, M. M., Jenkins, C. R., Dopita, M. A., Sadler, E. M., & Binette, L. 1986, AJ, 91, 1062

Pickles, A. J. 1998, PASP, 110, 863

Polletta, M., Tajer, M., Maraschi, L., et al. 2007, ApJ, 663, 81

Pović, M., Huertas-Company, M., Aguerri, J. A. L., et al. 2013, MNRAS, 435, 3444

Pović, M., Márquez, I., Masegosa, J., et al. 2015, MNRAS, 453, 1644

Pović, M., Sánchez-Portal, M., Pérez García, A. M., et al. 2009, ApJ, 706, 810

Ramón-Pérez, M., Bongiovanni, Á., Pérez García, A. M., et al. 2019, A&A, 631, A11

Ramón-Pérez, M. et al. 2018, A&A, in press

Renzini, A. 2006, ARA&A, 44, 141

Rix, H.-W., Barden, M., Beckwith, S. V. W., et al. 2004, ApJS, 152, 163

Roseboom, I. G., Oliver, S. J., Kunz, M., et al. 2010, MNRAS, 409, 48

Roy, N., Napolitano, N. R., La Barbera, F., et al. 2018, MNRAS, 480, 1057

Salim, S., Rich, R. M., Charlot, S., et al. 2007, ApJS, 173, 267

Sánchez Almeida, J., Elmegreen, B. G., Muñoz-Tuñón, C., et al. 2015, ApJL, 810, L15

Sánchez Almeida, J., Morales-Luis, A. B., Muñoz-Tuñón, C., et al. 2014, ApJ, 783, 45

Sarzi, M., Falcón-Barroso, J., Davies, R. L., et al. 2006, MNRAS, 366, 1151

Schawinski, K., Urry, C. M., Simmons, B. D., et al. 2014, MNRAS, 440, 889

Schlafly, E. F. & Finkbeiner, D. P. 2011, ApJ, 737, 103

Sérsic, J. L. 1968, Atlas de Galaxias Australes (Cordoba, Argentina: Observatorio Astronomico, 1968)

Shen, S., Mo, H. J., White, S. D. M., et al. 2003, MNRAS, 343, 978

Simard, L. 1998, Astronomical Society of the Pacific Conference Series, Vol. 145, GIM2D: an IRAF package for the Quantitative Morphology Analysis of Distant Galaxies (ASPCS), 108

Simard, L., Mendel, J. T., Patton, D. R., Ellison, S. L., & McConnachie, A. W. 2011, ApJS, 196, 11

Simard, L., Willmer, C. N. A., Vogt, N. P., et al. 2002, ApJS, 142, 1

Skrutskie, M. F., Cutri, R. M., Stiening, R., et al. 2006, AJ, 131, 1163

Spitoni, E., Calura, F., Matteucci, F., & Recchi, S. 2010, A&A, 514, A73

Stasińska, G., Cid Fernandes, R., Mateus, A., Sodré, L., & Asari, N. V. 2006, MNRAS, 371, 972

Stern, D., Eisenhardt, P., Gorjian, V., et al. 2005, ApJ, 631, 163

Strateva, I., Ivezić, Ž., Knapp, G. R., et al. 2001, AJ, 122, 1861

Straughn, A. N., Pirzkal, N., Meurer, G. R., et al. 2009, AJ, 138, 1022

Taylor, E. N., Hopkins, A. M., Baldry, I. K., et al. 2011, MNRAS, 418, 1587

Thomas, D., Maraston, C., Schawinski, K., Sarzi, M., & Silk, J. 2010, MNRAS, 404, 1775

Thuan, T. X., Goehring, K. M., Hibbard, J. E., Izotov, Y. I., & Hunt, L. K. 2016, MNRAS, 463, 4268

Thuan, T. X. & Izotov, Y. I. 2005, ApJS, 161, 240

Tody, D. 1993, in Astronomical Society of the Pacific Conference Series, Vol. 52, Astronomical Data Analysis Software and Systems II, ed. R. J. Hanisch, R. J. V. Brissenden, & J. Barnes, 173

Tremonti, C. A., Heckman, T. M., Kauffmann, G., et al. 2004, ApJ, 613, 898

Trinchieri, G. & di Serego Alighieri, S. 1991, AJ, 101, 1647

Tully, R. B. & Fisher, J. R. 1977, A&A, 500, 105

van der Wel, A., Franx, M., van Dokkum, P. G., et al. 2014, ApJ, 788, 28

van Gorkom, J. H., Knapp, G. R., Ekers, R. D., et al. 1989, AJ, 97, 708

Veilleux, S. & Osterbrock, D. E. 1987, ApJS, 63, 295

Vika, M., Vulcani, B., Bamford, S. P., Häußler, B., & Rojas, A. L. 2015, A&A, 577, A97

Villaverde, M., Cerviño, M., & Luridiana, V. 2010, A&A, 517, A93

Vorontsov-Velyaminov, B. & Krasnogorskaya, A. A. 1974, Morphological catalogue of galaxies

Vulcani, B., Bamford, S. P., Häußler, B., et al. 2014, MNRAS, 441, 1340

Walsh, D. E. P., Knapp, G. R., Wrobel, J. M., & Kim, D. W. 1989, ApJ, 337, 209

Wegner, G., Salzer, J. J., Jangren, A., Gronwall, C., & Melbourne, J. 2003, AJ, 125, 2373

Weigel, A. K., Schawinski, K., & Bruderer, C. 2016, MNRAS, 459, 2150

Willett, K. W., Lintott, C. J., Bamford, S. P., et al. 2013, MNRAS, 435, 2835

Wright, E. L. 2006, PASP, 118, 1711

Yin, S. Y., Liang, Y. C., Hammer, F., et al. 2007, A&A, 462, 535

York, D. G., Adelman, J., Anderson, John E., J., et al. 2000, AJ, 120, 1579

Zahid, H. J., Bresolin, F., Kewley, L. J., Coil, A. L., & Davé, R. 2012, ApJ, 750, 120